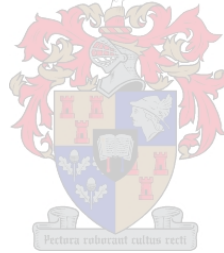


Concentrating solar power in South Africa - a comparison between parabolic trough and power tower technologies with molten salt as heat transfer fluid

by
Ian Vincent Poole

Thesis presented in partial fulfilment of the requirements for the degree of Master of Engineering (Mechanical) in the Faculty of Engineering at Stellenbosch University



Supervisor: Prof Frank Dinter

The financial assistance of the National Research Foundation (NRF) towards this research is hereby acknowledged. Opinions expressed and conclusions arrived at are those of the author and are not necessarily to be attributed to the NRF.

March 2017

Declaration

By submitting this dissertation electronically, I declare that the entirety of the work contained therein is my own, original work, that I am the sole author thereof (save to the extent explicitly otherwise stated), that reproduction and publication thereof by Stellenbosch University will not infringe any third party rights and that I have not previously in its entirety or in part submitted it for obtaining any qualification.

March 2017

Abstract

The most common type of concentrating solar power (CSP) plant in operation today is the parabolic trough plant. In recent years molten salt power tower plants have demonstrated the benefit of using molten salt as heat transfer fluid and a storage medium. New research has shown that molten salt can be used in parabolic trough technology in a similar manner. This thesis documents an investigation into both technologies in order to compare them on a qualitative and quantitative basis.

South Africa has become a hotspot for the development of CSP thanks to the abundant solar resource and the implementation of the Renewable Energy Independent Power Producer Procurement Program (REIPPPP) in the country. South Africa therefore provides a realistic backdrop for the comparison of the two CSP technologies.

Parabolic trough and a power tower simulation models are constructed for the comparison of the two technologies. Meteorological data for six selected sites in South Africa are used to simulate the performance of both of the technologies, while operating under a flat feed in tariff and a two-tiered feed in tariff.

Results of plant simulations show that molten salt can be used effectively as heat transfer fluid in parabolic trough technology. Parabolic troughs are shown to have higher annual optical efficiency compared to power towers. The main drawback of the parabolic trough technology is the thermal losses experienced in the field during overnight recirculation of the hot molten salt.

Parabolic trough solar fields show a large seasonal variation in efficiency while power tower plants are shown to benefit from relatively consistent solar field efficiency throughout the year. The seasonal variation in solar field efficiency results in substantially higher thermal energy being available in the summer than in the winter, thereby resulting in storages being filled and the subsequent dumping of solar energy in parabolic trough plants.

A simple cost model is built to compare the financial performance of the two technologies and allow for the optimization of the plants according to levelized cost of electricity (LCOE). At a site near Springbok in the Northern Cape Province optimization of both plant types resulted in an estimated LCOE of 0.127 USD/kWh_e and 0.129 USD/kWh_e for parabolic trough and power tower plants respectively.

This study demonstrates that both parabolic trough and power tower plants require careful consideration when selecting the most appropriate CSP technology for a given location. Depending on the available solar resource and the tariff structure under implementation, this thesis finds that both parabolic trough and power tower plants can offer competitive CSP solutions with their own set of strengths and weaknesses.

Uittreksel

Die mees algemene vorm van 'n gekonsentreerde sonkrag (GSK) aanleg in hedendaagse bedryf is die paraboliese trog aanleg. In die afgelope jare het gesmelte sout krag toring tegnologie voordeel getoon in die gebruik van gesmelte sout as hitte-oordrag vloeistof en as 'n stoor medium. Onlangse navorsing het getoon dat die gesmelte sout in paraboliese trog tegnologie op 'n soortgelyke wyse gebruik kan word. Hierdie tesis dokumenteer 'n ondersoek van altwee tegnologieë ten einde hulle te vergelyk op 'n kwalitatiewe en kwantitatiewe basis.

Suid-Afrika het gewild geword vir GSK ontwikkeling te danke aan die oorvloed van son hulpbron en die implementering van die Hernubare Energie Onafhanklike Krag Aankoop Program in die land. Suid-Afrika bied dus 'n realistiese agtergrond vir die vergelyking tussen die twee GSK tegnologieë.

Paraboliese trog en 'n krag toring modelle is gebou vir die vergelyking van die twee tegnologieë. Meteorologiese data vir ses gekiesde liggings in Suid-Afrika word gebruik om die optrede van beide tegnologieë te simuleer, terwyl dit bedryf word onder 'n vaste koers invoer tarief en 'n twee-vlak invoer tarief.

Resultate van aanleg simulاسies toon dat gesmelte sout effektief as hitte-oordrag vloeistof in paraboliese trog tegnologie gebruik kan word. Paraboliese trôe vertoon 'n hoër jaarlikse optiese doeltreffendheid in vergelyking met krag torings. Die mees kenmerkende nadeel van die paraboliese trog tegnologie is die termiese verliese in die veld tydens oornag hersirkulasie van die warm gesmelte sout.

Paraboliese trog sonvelde wys 'n groot seisoenale verskil in doeltreffendheid terwyl die krag toring aanlegte wys 'n konstante sonveld doeltreffendheid deur die jaar. Die seisoenale verskil in die sonveld doeltreffendheid beteken dat meer termiese energie beskikbaar in die somer in vergelyking met die winter maande, daarvoor word die stoortenke vol en die daaropvolgende storting van sonenergie in paraboliese trog aanlegte.

'n Eenvoudige kostemodel is gebou om die finansiële prestasie van die twee tegnologieë te vergelyk en voorsiening te maak vir die optimalisering van die aanlegte volgens gelyke koste van elektrisiteit (GKVE). Op 'n ligging naby Springbok in die Noord-Kaap het optimalisering van beide aanlegsoorte gelei tot 'n geskatte GKVE van 0.127 USD/kWh_e en 0.129 USD/kWh_e vir paraboliese trog en krag toring aanlegte onderskeidelik

Hierdie studie toon dat beide tegnologieë deeglike oorweging vereis vir die keuse van die mees geskikte GSK tegnologie vir 'n gegewe ligging. Afhangende van die beskikbare sonkrag hulpbron en die tariefstruktuur onder implementering, bevind hierdie tesis dat beide paraboliese trog en krag toring aanlegte mededingende GSK oplossings met hul eie stel sterk- en swakpunte kan bied.

Acknowledgements

I would like to express my gratitude to my supervisor, Prof Frank Dinter, for his support throughout this project. Thank you for giving me the opportunity to travel and to learn. Your passion for concentrating solar power is contagious and I will always be grateful for your guidance.

To the team at the Solar Thermal Energy Research Group (STERG) – Thank you for your guidance and friendship over the last two years. I am so fortunate to have been surrounded by people with a shared enthusiasm for renewable and sustainable energy.

I would also like to acknowledge the Department of Mechanical and Mechatronic Engineering at Stellenbosch University for hosting my research and allowing me to pursue my passion for engineering.

Thank you to the South African Weather Service, the Southern African Radiation Network and European Community Solar Data for their contribution in the form of meteorological data.

Lastly, thank you to the NRF for funding this project and the travel associated with this research.

To my loving family: Vaughn, Kate and Loren, and to Claire, for her constant kindness and support.

Table of contents

| | |
|--|------|
| Abstract..... | i |
| Uittreksel..... | ii |
| Acknowledgements..... | iii |
| Dedication..... | iv |
| Table of contents..... | v |
| List of figures..... | viii |
| List of tables..... | xi |
| Nomenclature..... | xiii |
| 1. Introduction..... | 1 |
| 1.1. Background..... | 1 |
| 1.2. Motivation..... | 3 |
| 1.3. Research objectives..... | 3 |
| 1.4. Methodology..... | 4 |
| 1.5. Research limitations..... | 5 |
| 2. Literature review..... | 6 |
| 2.1. Parabolic trough plants..... | 6 |
| 2.2. Power tower plants..... | 12 |
| 2.3. Molten salt as heat transfer fluid..... | 15 |
| 2.4. Concentrating solar power in South Africa..... | 17 |
| 2.5. High temporal resolution irradiance data..... | 19 |
| 2.6. Simulation of concentrating solar power plants..... | 20 |
| 2.7. Conclusion..... | 21 |
| 3. Parabolic trough plant description..... | 22 |
| 3.1. Overview..... | 22 |
| 3.2. Solar collector..... | 23 |
| 3.3. Receiver tube..... | 24 |
| 3.4. Solar field layout..... | 25 |
| 3.5. Thermal energy storage..... | 26 |
| 3.6. Power cycle..... | 26 |
| 3.7. Conclusion..... | 27 |
| 4. Power tower plant description..... | 28 |
| 4.1. Overview..... | 28 |
| 4.2. Heliostat..... | 29 |

| | | |
|-------------|--|----|
| 4.3. | Receiver | 29 |
| 4.4. | Conclusion | 30 |
| 5. | Plant modelling | 31 |
| 5.1. | Solar time and solar geometry | 31 |
| 5.2. | Parabolic trough solar field | 33 |
| 5.3. | Power tower solar field..... | 42 |
| 5.4. | Thermal energy storage system model | 46 |
| 5.5. | Power cycle model | 48 |
| 5.6. | Plant control and operating strategy | 49 |
| 5.7. | Parasitic consumption..... | 50 |
| 5.8. | System Advisor Model comparison | 51 |
| 5.9. | Financial model..... | 56 |
| 5.10. | Conclusion | 59 |
| 6. | Site selection and meteorological data..... | 60 |
| 6.1. | Selecting sites in South Africa | 60 |
| 6.2. | Compilation of site meteorological data | 62 |
| 6.3. | Conclusion | 63 |
| 7. | Simulation results | 64 |
| 7.1. | Operation of parabolic trough and power tower plants | 64 |
| 7.2. | Optimization of plant design..... | 72 |
| 7.3. | Optimized plant simulation results..... | 73 |
| 7.4. | Discussion..... | 76 |
| 7.5. | Conclusion | 77 |
| 8. | Conclusion..... | 78 |
| 8.1. | Summary of findings | 78 |
| 8.2. | Conclusion | 79 |
| 8.3. | Contributions | 79 |
| 8.4. | Recommendations for further work..... | 79 |
| Appendix A: | Synthetically developed direct normal irradiance data | 81 |
| A.1. | The effect of direct normal irradiance data on plant modelling | 81 |
| A.2. | Method for generating synthetic irradiation data | 84 |
| A.3. | Evaluation of synthetic direct normal irradiation data | 85 |
| A.4. | Conclusion | 89 |
| Appendix B: | Plant control and operation strategy..... | 90 |
| B.1. | Parabolic trough solar field control..... | 90 |
| B.2. | Power tower receiver and solar field control..... | 93 |

| | |
|---|-----|
| B.3. Power cycle control | 95 |
| B.4. Conclusion | 98 |
| Appendix C: Pressure drop calculations | 99 |
| C.1. Parabolic trough solar field | 99 |
| C.2. Power tower receiver | 102 |
| Appendix D: Levelized cost of electricity sensitivity | 103 |
| Appendix E: Thermophysical properties of molten salt | 105 |
| Appendix F: Site monthly direct normal irradiance | 106 |
| References | 107 |

List of figures

| | |
|---|----|
| Figure 1: Parabolic trough focusing incident radiation onto the receiver tube | 1 |
| Figure 2: Tower, receiver and heliostat field at Gemasolar | 2 |
| Figure 3: A comparison of parabolic trough and power tower technology in operation, under construction and reportedly in development (data: National Renewable Energy Laboratory, 2016)..... | 2 |
| Figure 4: Solar collector assembly (SCA)..... | 8 |
| Figure 5: Rendering of a receiver tube | 9 |
| Figure 6: Heliostats in the field (left) and the cavity receiver in operation (right) at PS20, Spain..... | 13 |
| Figure 7: Typical demand on the South African electrical grid in summer and winter including the tariff periods for Renewable Energy Independent Power Producer Procurement Program Round 3 and 3.5 | 17 |
| Figure 8: International Renewable Agency renewable energy map for South Africa (Wu <i>et al.</i> , 2015a) | 18 |
| Figure 9: Molten salt parabolic trough plant design..... | 23 |
| Figure 10: Molten salt power tower plant design..... | 28 |
| Figure 11: Generic parabolic trough and power tower model schematic diagram | 31 |
| Figure 12: Summary of solar time and geometry model inputs and outputs..... | 33 |
| Figure 13: Solar collector assembly diagram showing the incident angle | 34 |
| Figure 14: Solar collector model inputs and outputs | 35 |
| Figure 15: Receiver tube energy diagram | 35 |
| Figure 16: Heat loss curves for the Archimede Solar Energy HCEMS-11 receiver tube | 37 |
| Figure 17: Receiver tube model inputs and outputs..... | 37 |
| Figure 18: Solar field energy balance control volume..... | 38 |
| Figure 19: Solar field energy balance diagram showing the connection of the solar collector, receiver tube and thermal energy storage models..... | 40 |
| Figure 20: Heliostat field efficiency vs. zenith angle (Gauché <i>et al.</i> , 2012; Kelly, 2010; Kolb <i>et al.</i> , 2011) | 43 |
| Figure 21: Heliostat field model inputs and outputs | 43 |
| Figure 22: Receiver efficiency curve according to wind speed at the receiver height and incident thermal power..... | 44 |
| Figure 23: Summary of inputs and outputs for the receiver model | 45 |

| | |
|--|----|
| Figure 24: Linking the heliostat field and receiver models to the thermal energy storage models..... | 46 |
| Figure 25: Cold tank model inputs and outputs..... | 48 |
| Figure 26: Hot tank model inputs and outputs | 48 |
| Figure 27: Power cycle thermal to electrical efficiency..... | 49 |
| Figure 28: Power cycle ambient temperature modifier | 49 |
| Figure 29: Power cycle molten salt temperature modifier | 49 |
| Figure 30: HTF return temperature from the steam generator system | 49 |
| Figure 31: Power cycle model inputs and outputs | 49 |
| Figure 32: Pressure drop over a parabolic trough solar field with a solar multiple of 2 (left) and a power tower receiver with tower piping with a solar multiple of 2.4 (right) | 51 |
| Figure 33: Plant operation comparison using SAM physical parabolic trough model vs. the designed molten salt parabolic trough model..... | 53 |
| Figure 34: Monthly net electrical yield comparison between SAM and the parabolic trough model..... | 54 |
| Figure 35: Plant operation comparison between the molten salt power tower model and SAM..... | 55 |
| Figure 36: Monthly net electrical yield comparison between the molten salt power tower model and SAM..... | 56 |
| Figure 37: International Renewable Energy Agency zones for concentrating solar power development (Wu <i>et al.</i> , 2015a)..... | 60 |
| Figure 38: Proposed sites for a 100 MW _e CSP plant showing the annual average direct normal irradiation (GeoModel Solar, 2014; Google Inc., 2015)..... | 61 |
| Figure 39: Performance of parabolic trough (blue) and power tower (red) plants over three winter days at the Vryburg site from June 10 th | 67 |
| Figure 40: Performance of parabolic trough (blue) and power tower (red) plants over three summer days at the Vryburg site from December 25 th | 68 |
| Figure 41: Power tower (left) and parabolic trough (right) loss diagrams for a flat tariff structure..... | 69 |
| Figure 42: Power tower (left) and parabolic trough (right) loss diagrams for a two-tiered tariff structure | 71 |
| Figure 43: Optimization of a power tower plant at the Springbok site according to levelized cost of electricity | 72 |
| Figure 44: Optimization of a power tower plant at the springbok site operating under the two-tiered tariff system according to levelized profit of electricity | 73 |
| Figure 45: Electrical yield, capital cost and LCOE comparison of parabolic trough and power tower plants at the six locations operating under a flat tariff structure..... | 75 |

| | |
|--|-----|
| Figure 46: Electrical yield, capital cost and LCOE comparison of parabolic trough and power tower plants at the six locations operating under a two-tier tariff structure. | 75 |
| Figure 47: Daily time trace of the accumulated electrical energy as simulated on the bases of measured and synthesized minutely DNI data sets and on a set with hourly time resolution (Beyer <i>et al.</i> , 2010) | 81 |
| Figure 48: Evaluating the effect of hour vs. minute averaged data | 82 |
| Figure 49: Comparing the effect of minute resolution (red) vs. hour resolution (blue) DNI on parabolic trough solar field return temperature and cold tank storage temperature | 83 |
| Figure 50: The process of generating a dimensionless DNI signature (Fernández-Peruchena <i>et al.</i> , 2015) | 85 |
| Figure 51: Comparison of measured and synthetically generated direct normal irradiance data from Bloemfontein | 86 |
| Figure 52: Control logic for parabolic trough solar field | 91 |
| Figure 53: Temperature control of the parabolic trough solar field over two consecutive days in Springbok | 92 |
| Figure 54: Power tower receiver control logic | 93 |
| Figure 55: Temperature control of the power tower solar field over two consecutive days in Springbok | 95 |
| Figure 56: Power cycle control logic | 96 |
| Figure 57: Power cycle operation with a flat tariff over two consecutive days in Springbok | 97 |
| Figure 58: Power cycle control with a two-tiered tariff over two consecutive days in Upington | 98 |
| Figure 59: 'H-shaped' molten salt parabolic trough solar field layout. The solar field is made up of hot (red) and cold (blue) runner and header pipes which distribute molten salt to individual loops in the field | 100 |
| Figure 60: Illustration of header pipe in parabolic trough solar field with decreasing diameter | 101 |
| Figure 61: LCOE sensitivity analysis for a power tower plant | 103 |
| Figure 62: LCOE sensitivity analysis for a parabolic trough plant | 104 |
| Figure 63: Properties of solar salt | 105 |
| Figure 64: Monthly DNI distribution for selected sites in South Africa | 106 |

List of tables

| | |
|--|----|
| Table 1: Typical capital cost categories for a concentrating solar power plant (adapted from Turchi, 2010)..... | 11 |
| Table 2: Capital expenses for thermal oil parabolic trough plant using Ultimate Trough solar collector assemblies (Kurup & Turchi, 2015) | 11 |
| Table 3: Capital expenses for a molten salt parabolic trough plant (Ruegamer <i>et al.</i> 2013)..... | 12 |
| Table 4: Heliostat size selection for power tower plants (SolarReserve LLC., 2016; National Renewable Energy Laboratory, 2016b)..... | 14 |
| Table 5: Capital expenses for a power tower plant (Kolb <i>et al.</i> , 2011) | 15 |
| Table 6: Capital expenses for a molten salt power tower plant (Turchi <i>et al.</i> , 2013) | 15 |
| Table 7: Comparison of thermal oil and solar salt thermophysical properties | 16 |
| Table 8: Two-tiered feed-in tariff structure for Round 3 and Round 3.5 of the Renewable Energy Independent Power Producer Procurement Program (Relancio <i>et al.</i> , 2015; Department of Energy, 2013)..... | 17 |
| Table 9: Parabolic trough solar field description..... | 23 |
| Table 10: Ultimate Trough solar collector assembly specifications..... | 24 |
| Table 11: Receiver tube specifications | 25 |
| Table 12: Thermal energy storage specifications | 26 |
| Table 13: Power cycle design parameters | 27 |
| Table 14: Heliostat design parameters..... | 29 |
| Table 15: Power tower heliostat field description | 29 |
| Table 16: Receiver design parameters (De Meyer <i>et al.</i> , 2015) | 30 |
| Table 17: Coefficients for the equation of time | 32 |
| Table 18: Solar collector performance characteristics with a 70 mm receiver tube (Riffelmann <i>et al.</i> , 2013b) | 34 |
| Table 19: Receiver tube geometrical and optical performance characteristics | 36 |
| Table 20: Receiver tube performance characteristics (Matino & Maccari, 2015)..... | 37 |
| Table 21: Plant description for power tower model validation..... | 52 |
| Table 22: Plant description for power tower model validation..... | 54 |
| Table 23: Capital expenses for a molten salt parabolic trough plant..... | 57 |
| Table 24: Capital expenses for a molten salt power tower plant..... | 58 |
| Table 25: Operating expenses for a molten salt parabolic trough and power tower plants | 58 |

| | |
|---|-----|
| Table 26: Two-tiered feed-in tariff structure..... | 59 |
| Table 27: IRENA site information..... | 61 |
| Table 28: Meteorological data sources for the six selected sites..... | 63 |
| Table 29: Meteorological information for the six selected sites | 63 |
| Table 30: Power tower plant design for flat tariff structure | 65 |
| Table 31: Parabolic trough plant design for flat tariff structure..... | 65 |
| Table 32: Yield analysis for a power tower and parabolic trough plant design for a flat tariff structure..... | 69 |
| Table 33: Power tower plant design for two-tiered tariff structure | 70 |
| Table 34: Parabolic trough plant design for two-tiered tariff structure | 70 |
| Table 35: Yield analysis for a power tower plant design for a two-tiered tariff structure..... | 71 |
| Table 36: Optimized power tower plant designs for a flat tariff structure | 74 |
| Table 37: Optimized parabolic trough plant designs for a flat tariff structure..... | 74 |
| Table 38: Optimized power tower plant designs for a two-tiered tariff structure | 74 |
| Table 39: Optimized parabolic trough plant designs for a two-tiered tariff structure | 74 |
| Table 40: SAURAN station locations..... | 86 |
| Table 41: Annual indicators of dispersion | 89 |
| Table 42: Overall performance indicators | 89 |
| Table 43: Cost components used for sensitivity analysis of a power tower plant in Springbok..... | 103 |
| Table 44: Cost components used for sensitivity analysis of a parabolic trough plant in Springbok..... | 104 |

Nomenclature

| Symbol | Description | Unit |
|------------|----------------------------|---------------------------|
| C | Constant | - |
| $CAPEX$ | Capital expense | USD |
| cf | Cleanliness factor | - |
| c_p | Heat capacity | $\text{kJ}/(\text{kg K})$ |
| CRF | Capital return factor | - |
| D | Daylight savings modifier | - |
| DNI | Direct normal irradiance | W/m^2 |
| E | Total energy | GWh |
| EOT | Equation of Time | h |
| g | Gravitational acceleration | m/s^2 |
| H | Height | m |
| IAM | Incidence angle modifier | - |
| LC | Longitude correction | h |
| LCT | local clock time | h |
| m | Mass | kg |
| \dot{m} | Mass flow rate | kg/s |
| $OPEX$ | Operating expense | USD |
| P | Power | W |
| Q | Thermal energy | J |
| \dot{Q} | Thermal power | W |
| \dot{q} | Heat flux | W/m |
| SM | Solar multiple | - |
| T | Temperature | $^{\circ}\text{C}$ or K |
| \bar{T} | Average temperature | $^{\circ}\text{C}$ or K |
| t | Time | h or s |
| tar | Tariff | USD/kWh_e |
| V | Velocity | m/s |
| ΔT | Change in temperature | $^{\circ}\text{C}$ or K |
| Δt | Change in time / time step | s |
| α | Absorptivity | - |
| γ | Azimuth angle | $^{\circ}$ |
| γ | Geometry defects | - |
| γ | Tracking error | - |
| δ | Declination angle | $^{\circ}$ |
| η | Efficiency | - or % |
| θ | Solar angle | $^{\circ}$ |
| κ | Efficiency modifier | - |
| ρ | Fluid density | kg/m^3 |
| ρ | Mirror reflectance | - |

| | | |
|----------|----------------|---|
| τ | Transmissivity | |
| ω | Hour angle | ◦ |
| ϕ | Latitude | ◦ |

Subscripts

| | |
|--------------|--------------------------|
| a | Annual |
| <i>abs</i> | Absorber |
| <i>amb</i> | Ambient |
| <i>att</i> | Attenuation |
| <i>aux</i> | Auxiliary |
| c | Cold |
| col | Collector |
| dp | Design point |
| <i>dump</i> | Dumping from defocusing |
| e | Electrical |
| h | Hot |
| <i>HTF</i> | Heat transfer fluid |
| i | Incidence angle |
| incident | Incident to surface |
| opt | Optical |
| <i>p</i> | Pump |
| rec | Receiver / receiver tube |
| s | Solar |
| SCA | Solar collector assembly |
| <i>SF</i> | Solar field |
| <i>spill</i> | Spillage |
| th | Thermal |
| tmz | Time zone meridian |
| trough | Parabolic trough |
| z | Zenith angle |
| 0 | Initial condition |
| 0° | Zero incidence angle |
| c | Cold |

Abbreviations

| | |
|---------------|-------------------------------|
| ACC | Air-cooled condenser |
| ASE | Archimede Solar Energy |
| CAPEX | Capital expense |
| CSP | Concentrating solar power |
| DHI | Diffuse horizontal irradiance |
| DNI | Direct normal irradiance |
| GHI | Global horizontal irradiance |
| <i>guiSmo</i> | Guideline to Solar Modeling |

| | |
|---------|--|
| HCEMS | Heat collecting element – molten salt |
| HP | High pressure |
| HTF | Heat transfer fluid |
| IP | Intermediate pressure |
| IRENA | International Renewable Energy Agency |
| LCOE | Levelized cost of electricity |
| LP | Low pressure |
| NREL | National Renewable Energy Laboratory |
| OPEX | Operational expense |
| PC | Power cycle |
| REIPPPP | Renewable Energy Independent Power Producer Procurement Program |
| SAM | System Advisor Model |
| SAURAN | Southern African Universities Radiometric Network |
| SBP | Schlaich, Bergermann & Partner |
| SCA | Solar collector assembly |
| SEGS | Solar Electric Generating System |
| STEC | Solar thermal electricity component |
| TES | Thermal energy storage |
| USA | United States of America |
| UFS | University of the Freestate |
| SAWS | South African Weather Service |

1. Introduction

1.1. Background

South Africa currently has three concentrating solar power (CSP) plants in operation. Two of the plants are parabolic trough plants and the third is a power tower plant. The development of CSP in South Africa is part of the Renewable Energy Independent Power Producer Procurement Program (REIPPPP). The REIPPPP has resulted in 200 MWe of CSP capacity, with an additional 450 MWe to be added in coming years.

The majority of the renewable energy projects in development under the REIPPPP are conventional photovoltaic solar power plants and wind power plants. The main drawback when working with these two conventional renewable technologies is that they only produce electricity intermittently. The wind does not blow constantly and the sun only shines during clear days.

A viable solution to the problem of intermittent renewable energy is CSP. The concept of CSP is to concentrate solar radiation onto a receiver in order to heat up a fluid to a high temperature. This heat can then be stored and used to generate electricity even when there is no solar radiation available – it is therefore a dispatchable form of renewable energy. It is for this reason that CSP is being implemented under the REIPPPP in South Africa.

The use of thermal storage allows a CSP plant to generate power in a flexible manner. A plant with large thermal storage can generate electricity on a 24-hour per day basis (base load plant). Alternatively, a smaller storage can be selected and the plant can be used to provide power at peak times during the day when the demand on the electrical grid is at its highest (peaking / load following plants).

The most common CSP technology is the parabolic trough plant, which typically concentrates solar radiation to heat up a heat transfer fluid (HTF) known as thermal oil (Figure 1). The thermal oil is heated up to 393 °C, after which it is pumped through a heat exchanger to generate steam, which in turn drives a turbine generator system to create electrical energy. Most parabolic trough plants use a molten nitrate salt (solar salt) as a medium of thermal storage. In this case, the thermal oil is used to heat up the molten salt via a second heat exchanger.

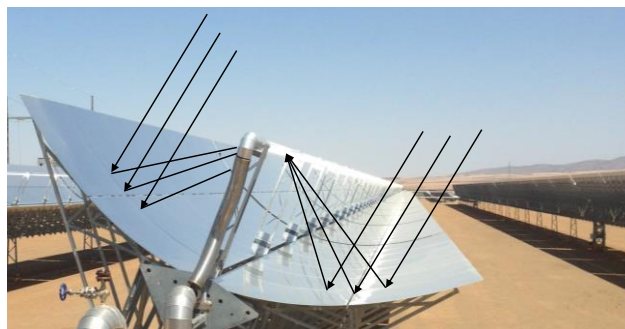


Figure 1: Parabolic trough focusing incident radiation onto the receiver tube

Molten salt power tower technology is the newest CSP technology to reach the market. Power towers use a field of flat mirrors called heliostats to focus the sun's radiation onto a central receiver (Figure 2). Power tower technology is currently the largest competitor to parabolic trough technology. Figure 3 illustrates the shift towards power tower technology by comparing the installed generating capacity to the generating capacity under construction and in development.



Figure 2: Tower, receiver and heliostat field at Gemasolar

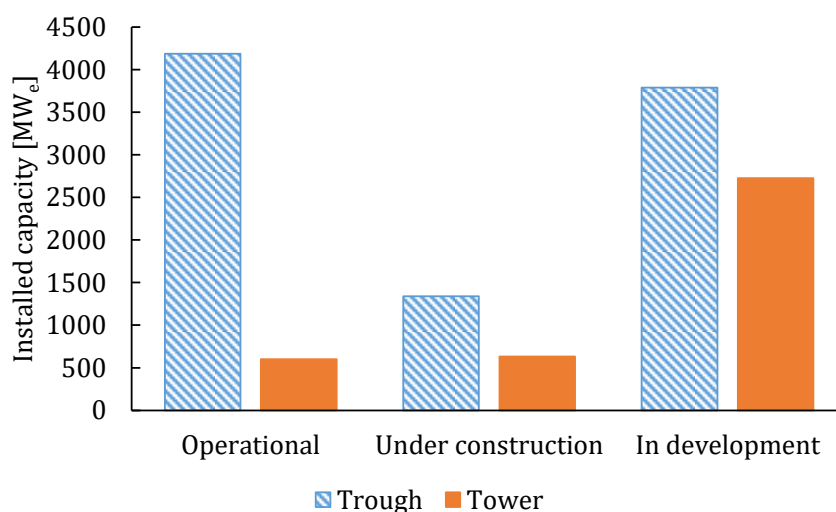


Figure 3: A comparison of parabolic trough and power tower technology in operation, under construction and reportedly in development (data: National Renewable Energy Laboratory, 2016)

Molten salt is particularly well suited to the storage of thermal energy due to its thermophysical properties. Molten salt is liquid between the range of 220 °C and 600 °C, it can be stored in atmospheric pressure tanks and it can be pumped using conventional methods.

In modern molten salt power tower plants, molten salt is pumped up the tower, through the receiver where it is heated, and back down the tower after which it is stored directly in large tanks. The molten salt is therefore used as HTF and a storage medium.

The high temperatures attainable using molten salt result in a high efficiency steam cycle and electrical generation process. Furthermore, the direct storage of high temperature molten salt lowers storage costs. Both of these factors result in a lower

cost of generating electricity compared to conventional parabolic trough technology using oil as HTF.

Recent investigations have shown that the integration of direct molten salt storage into the well-established parabolic trough technology has the potential to drastically reduce the cost of electricity. This would entail the use of solar salt as a heat transfer fluid in the field and as a direct storage medium.

Using high temperature molten salt in a parabolic trough plant creates complications, considering the long and complex network of piping in the solar field. The most prominent concern with using molten salt as a HTF is the event of freezing in the pipes. The molten salt freezing temperature of ~ 220 °C is problematic because all piping and fittings in the solar field need to be kept at a high temperature during operation, which also results in high heat losses. Ongoing research into using solar salt as heat transfer fluid is providing potential solutions to the problems of freezing and heat loss – making molten salt parabolic trough technology competitive with molten salt power tower technology.

1.2. Motivation

Molten salt power tower plants have shown the benefit of using molten salt as HTF and a storage medium. Molten salt parabolic trough plants have the potential to compete with power tower plants, however, there are no large-scale plants in operation. Therefore, it is first required to determine whether a large-scale parabolic trough is feasible, thereafter a detailed investigation is required into both technologies in order to compare them on a qualitative and quantitative basis.

Considering the substantial solar resource available, and the current development of CSP in the country, South Africa will most likely be one of the locations for the next generation of CSP development. Evaluation of the cost and performance of both systems implemented in South African conditions allows for a realistic comparison of the two technologies in question. The comparison will also provide insight into the effect of site selection, meteorological data and tariff structure on the design and operation of power tower and parabolic trough CSP plants.

1.3. Research objectives

The primary objective of this thesis is to compare parabolic trough and power tower technologies using solar salt as a heat transfer fluid. Before the two technologies can be compared, the feasibility of using molten salt in a parabolic trough plant needs to be demonstrated. The research objectives are therefore:

- Demonstrate the feasibility of a molten salt parabolic trough plant using molten salt as HTF.
- Compare the parabolic trough plant to the power tower plant according to differences in system efficiency, annual electrical yield and levelized cost of electricity.
- The development of a computation tool to contribute to the comparative analysis of parabolic trough and power tower technologies using molten salt as heat transfer fluid.

The secondary objectives relate to the South African context of the study:

- Identify the most promising location in South Africa for future development of CSP with a prediction of the electrical yield and cost of generating electricity of at the site.
- Determine the implications of the different REIPPPP tariff structures on molten salt parabolic trough and power tower technologies.

1.4. Methodology

The first step of the comparison of the two technologies is a review of the design and major components of parabolic trough and power tower plants. The use of molten salt as heat transfer fluid and storage medium is then reviewed. In order to understand the implementation of CSP in South Africa, the development of the REIPPPP is discussed and potential sites for CSP sites are investigated.

A system-level description for a molten salt parabolic trough plant is then provided. The plant design uses the current state-of-the-art components. The main areas of the plant design are the solar field, the thermal energy storage and the power cycle. Each main component within these areas of the plant is specified and described.

A system-level description is then provided for a molten salt power tower plant. Both plants are designed to utilize identical thermal energy storage and power cycle components. Therefore the focus of the power tower plant description is on the heliostat field and the central receiver.

A model for each of the plants is then constructed. The models use a combination of energy balance analysis and component performance parameters, which are obtained from literature and manufacturer specifications. The modelling of individual components of both models is described in detail. The performance of these models is compared to that of the System Advisor Model, which has been verified with real plant operational data.

A financial model is developed to compare the financial performance of the plants under two different feed-in tariff structures, which have been implemented in previous rounds of the REIPPPP.

A site selection tool and renewable energy map developed by the International Renewable Energy Agency (IRENA) was used in order to select the most promising sites for CSP development in South Africa. Meteorological data is required in order for the models to perform an annual simulation at selected sites. Direct normal irradiation (DNI) data, wind data and ambient temperature data are obtained from a variety of sources including ground based weather stations, satellite derived information and solar resource data from the Southern African Universities Radiometric Network (SAURAN). Meteorological data is generated, evaluated and compiled to be used by the models at the selected sites.

The parabolic trough and power tower models are used to simulate the performance of both technologies at each of the selected sites, under the two different feed-in tariff structures. The results of these simulations demonstrate the effect of varying

meteorological conditions, locations and tariff structures on both parabolic trough and power tower technologies.

Finally, conclusions are drawn regarding the comparison of the two technologies and the suitability of the various sites in South Africa.

1.5. Research limitations

The work presented in this thesis is focused on the feasibility of a molten salt parabolic trough plant and the comparison of its performance to a molten salt power tower plant. The design and simulation work carried out is done on a system level basis and is not intended to be detailed design in terms of component performance or financial analysis.

2. Literature review

In this section the developments of the two leading CSP technologies, parabolic trough and power towers, are reviewed in detail. The literature behind the use of molten salt as HTF and a storage medium in these two technologies is then investigated.

The current implementation of CSP in South Africa is then described with a focus on the Renewable Energy Independent Power Procurement Program (REIPPPP). This is followed by an investigation into the importance of high temporal resolution solar data and its availability in South Africa. The section is concluded with a summary of CSP modelling tools currently available.

2.1. Parabolic trough plants

This section describes the development of the technology and the main components that are used to collect solar energy. The current costs of parabolic trough plants are then reviewed.

2.1.1. Development

The first commercial scale CSP plant was constructed in 1984. This was the first of the Solar Electric Generating System (SEGS) – SEGS I, which began operation in 1985 (Pavlović *et al.*, 2012). This was then extended to include another 8 SEGS plants (SEGS II to SEGS IX) up until 1991. Situated in California, these plants are still in operation today. All nine of the SEGS plants used thermal oil as a heat transfer fluid, and gas burners were primarily used as an energy backup. SEGS I used direct thermal oil storage, however, the concept was abandoned for the rest of the plants due to the high costs (Cabeza *et al.*, 2012). The technical development and operational experience gained from the SEGS plants was a main contributor to the success of parabolic trough technology in the years to follow. In 2007, the next large scale parabolic trough plant was constructed in Nevada.

Andasol I was the first commercial CSP plant to be built in Europe, in 2008. Andasol I set the precedent for the next generation of parabolic trough plants. Followed by the construction of Andasol II and III, the Spanish plants included a 7.5 hour molten salt thermal storage and a 50 MW_e generating capacity (Dinter & Möller, 2015).

Between 2008 and 2013, political support through attractive feed-in tariffs and renewable energy quotas made the development of many more plants in Spain possible. There are currently 47 commercial scale parabolic trough plants in operation in Spain. Most of the plants have the same basic design: A 50 MW_e capacity with 7.5 hours of indirect molten salt storage and a thermal oil heat transfer fluid. The capacity of parabolic trough technology in Spain is 2.3 GW_e of the global capacity of 4.2 GW_e.

The scale of parabolic trough plants was increased in the United States through the Solana (Abengoa Solar, 2013c) and Genesis (Nextera Energy Resources, 2014) projects in 2013 and 2014. Solana is the largest trough plant in the world according to annual electrical yield and aperture area. With an expected yield of 944 GWh_e per year and a solar field with an area of 2.2 million m², Solana demonstrates the scalability of parabolic trough technology.

In recent years parabolic trough technology has been implemented on the African continent. Kaxu and Bokpoort in South Africa and Noor I in Morocco are all in operation, using thermal oil as a heat transfer fluid. For further information on plants in South Africa, refer to Section 2.4.

Kearney *et al.* (2003) investigated the engineering aspects of using molten salt as a heat transfer fluid and a direct storage medium in a parabolic trough plant. The use of molten salt as heat transfer fluid allows for higher temperatures to be attained compared to the conventional oil plants, which in turn increases the efficiency of the steam cycle. Furthermore, the molten salt can be stored directly, which eliminates the need for an oil-to-salt heat exchanger. It was concluded that the use of solar salt at a maximum operating temperature of 450 °C could reduce the LCOE of the parabolic trough technology by 14.2 %. It was also suggested that costs could be further reduced if higher temperatures were attained.

Kearney *et al.* (2004) proposed that the implementation of a molten salt system would be greatly assisted by the lessons learnt in power tower project known as 'Solar Two'. Experience gained with regards to the piping, valves and pumps would allow parabolic trough technology to adapt to the use of solar salt as HTF. They went on to provide potential solutions for engineering problems that are encountered when using molten salt as HTF.

The Italian electrical utility, ENEL, constructed a 5 MW_e demonstration plant in Sicily in 2010 (Falchetta *et al.*, 2010). The plant uses parabolic troughs with solar salt as a heat transfer fluid. The salt is stored in storage tanks directly rather than having to use a heat exchanger. This molten salt is then used to generate steam, which is fed into the nearby combine cycle 130 MW_e steam turbine. Unfortunately there have been very few publications with regard to the operation and performance of this plant.

In 2013 Abengoa Solar attempted to develop molten salt HTF components for parabolic trough solar power plants (Abengoa Solar, 2013a). It was found that using two storage tanks for thermal energy storage (TES) is currently more suitable than using a thermocline tank, as the thermocline technology is not yet competitive with the conventional two-tank storage. Freeze protection and freeze recovery systems were tested and proven. A major concern was the parasitic consumption of freeze protection systems if the performance of the plant was not optimized.

Abengoa Solar tested more than 13 different variations of ball joints, flexible hoses and rotary joints but could not find a solution that could perform under the high temperatures and pressures associated with the molten salt in the solar field. This was the reason that Abengoa's research in the direction of molten salt parabolic trough technology was halted.

Many of the potential operating issues such as freeze protection and receiver tube preheating have been solved (Maccari *et al.*, 2015) at Archimede Solar Energy (ASE) in Italy. The demonstration plant has two years of operating experience using molten salt as HTF with parabolic trough technology (Donnola *et al.*, 2015). The plant has allowed for successful development of high temperature receiver tubes and the associated valves, pumps and flexible hoses that are required for a parabolic trough plant using molten salt as HTF (Matino & Maccari, 2015).

2.1.2. Components

The solar field primarily consists of an array of solar collector assemblies and a network of heat transfer fluid piping. A solar collector is made up of mirrors mounted to parabolic shaped facets, which are in turn mounted to a large galvanized steel structure. The receiver tubes that contain HTF are mounted using supports in line with the focal point of the parabolic mirrors. The assembly of the solar collector, the receiver tubes and the relevant piping is called the solar collector assembly (SCA) (Figure 4).

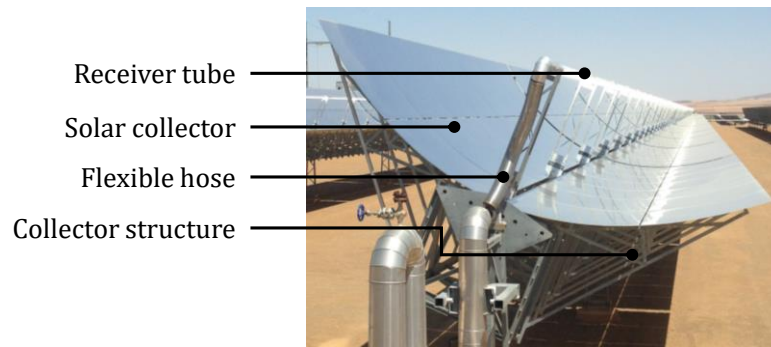


Figure 4: Solar collector assembly (SCA)

Receiver tubes (Figure 5) are constructed out of a stainless steel absorber tube with a cermet coating. Cermet is a spectrally selective composite coating, which allows for high values of absorbance and lower values of emittance while operating at high temperatures. This allows the receiver tubes to absorb the concentrated radiation from the solar collectors and prevents large levels of radiation losses to the environment (Archimede Solar Energy, 2016).

The absorber tube is enclosed in an evacuated glass tube. The vacuum between the absorber tube and the glass envelope prevents conduction and convection heat losses. The outer surface of the glass tube receives a non-reflective coating, which increases the transmittance of radiation through the glass onto the absorber tube. Furthermore, the glass is treated with a hydrophobic coating, which increases its resistance to atmospheric conditions, which might negatively affect the cleanliness of the glass.

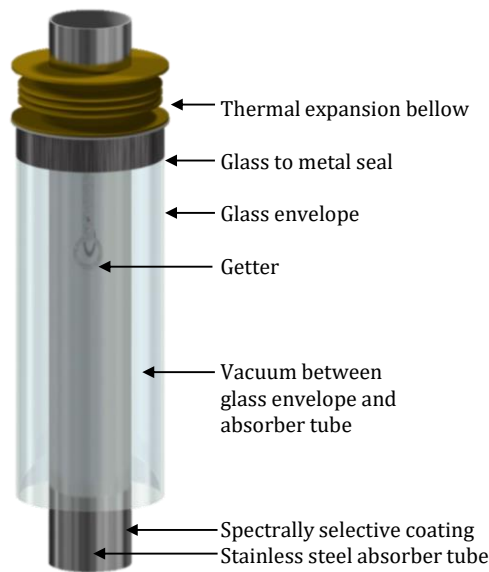


Figure 5: Rendering of a receiver tube

The first commercial trough-shaped solar collectors were designed by the American-Israeli company Luz Industries. Three iterations of the solar collector design (LS-1, LS-2, LS-3) were installed at the SEGS plants. The designs varied from a torque tube structure to space-frame structure. The lessons learnt from the development of the Luz collectors ultimately lead to the design of the Euro Trough. The Euro Trough used a so called 'torque box space frame design' and it was installed in most of the Spanish parabolic trough plants. The improved optical efficiency and larger aperture resulted in a 10 % improvement in thermal efficiency when compared to the Luz troughs.

A consortium of German institutions including Flagsol GmbH and Schlaich, Bergemann & Partner (SBP) then developed the Heliotrough (Janotte *et al.*, 2013). The Heliotrough has shown further optical improvements and implements a wider 6.78 m aperture in its design.

The next iteration of the Heliotrough was the Ultimate Trough, which is currently the best performing solar collector in terms of optical performance and cost (Schweitzer *et al.*, 2011). The large aperture of 7.52 m and allows for a high concentration ratio and a high thermal efficiency.

The Ultimate trough has shown optimum performance using molten salt as heat transfer fluid and a receiver tube diameter of 70 mm (Richert & Nava, 2012). The implementation of Ultimate Troughs as opposed to Euro Troughs when using thermal oil reduces the LCOE by ~9 %. When the use of solar salt as HTF is combined with the implementation of Ultimate Trough in a 100 MW_e (gross) plant, LCOE reductions of 20 % are possible compared to a conventional plant such as Andasol III (Ruegamer *et al.*, 2013).

2.1.3. Cost

This section contains details of various investigations into the cost of parabolic trough technology and the influence that molten salt would have on the cost of a parabolic trough plant.

Turchi (2010) performed an in-depth cost analysis of a conventional thermal oil parabolic trough plant. The report is supported by a plant design and cost estimation by WorleyParsons. Turchi (2010) groups the main capital expenses into the categories listed in Table 1. The capital costs are broken up into direct and indirect capital costs. Indirect capital costs are estimated to range between 25.8 % and 31.2 % of the total direct capital cost value.

Kurup & Turchi (2015) provide an up to date cost estimate of parabolic trough technology (Table 2). The implementation of Ultimate Trough solar collectors has resulted in a substantial reduction in cost in the solar field cost category as well as a slight decrease in cost of the HTF system. This is due to the large aperture solar collectors allowing for more efficient solar field operation. The influence of using a dry cooled power cycle as opposed to the wet cooled alternative is highlighted. A dry cooled cycle results in a ~38 % increase in the power cycle cost category.

Ruegamer *et al.* (2013) investigated the implementation of molten salt as HTF in combination with Ultimate Trough technology. The costs categories used in the model are detailed in Table 3. Ruegamer *et al.*, assume optimistically low costs for the TES, HTF system and power cycle due to the higher operating temperatures using molten salt. The collector field is assumed to be slightly more expensive due to the implementation of high temperature receiver tubes.

Turchi (2010) also provides a simplified method of evaluating the operating costs of a CSP plant. The costs are broken up into fixed and variable operating costs. Fixed operating costs are determined by the capacity of the plant (Paying on-site staff, annual maintenance etc.). Variable operating costs are determined by the level of annual generation (water usage, variable maintenance, chemicals lubricants). Turchi calculates fixed operating costs to equate to 70 USD per kW_e of the turbine size and variable costs as 3 USD per MWh_e of electrical energy produced.

Table 1: Typical capital cost categories for a concentrating solar power plant (adapted from Turchi, 2010)

| Cost category | Description |
|------------------------------------|--|
| Direct capital costs | |
| Site improvements | Roads parking and fencing Earthworks Drainage and evaporation ponds |
| Collector field | solar collector assemblies receiver tubes foundations and support structures Instrumentation, electronics and controls Installation labour |
| Heat transfer fluid system | Freeze protection HTF pumps Expansion systems header and runner piping Fluid costs |
| Thermal energy storage system | Storage vessels Insulation Molten salt pumps Fluid costs |
| Power cycle | Steam generator system Steam turbine system Electrical generator Air cooled condenser system Steam cycle pumps, drives and control |
| Indirect capital costs | |
| EPC | Engineering expenses Procurement costs Construction costs |
| Project management and owners cost | Project management costs Legal fees Permitting Environmental surveys Taxes Interest during construction |

Table 2: Capital expenses for thermal oil parabolic trough plant using Ultimate Trough solar collector assemblies (Kurup *et al.*, 2015)

| Capital expense component | Cost | Unit |
|----------------------------------|-------------|-----------------------|
| Site improvements | 30.0 | USD/m ² |
| Collector field | 170.0 | USD/m ² |
| Heat transfer fluid system | 70.0 | USD/m ² |
| Thermal energy storage | 75.0 | USD/kWh _{th} |
| Power cycle | 1270.0 | USD/kW _e |
| Contingency | 10.0 | % of CAPEX |
| EPC and Project management | 18.5 | % of CAPEX |

Table 3: Capital expenses for a molten salt parabolic trough plant (Ruegamer *et al.* 2013)

| Capital expense component | Cost | Unit |
|----------------------------|-------|----------------------|
| Site improvements | 20.0 | USD/m ² |
| Solar field | 210.0 | USD/m ² |
| Thermal energy storage | 170.0 | USD/kW _{th} |
| Heat transfer fluid system | | |
| Steam turbine system | 973.0 | USD/kW _e |
| Steam generating system | | |

2.2. Power tower plants

Power tower technology uses a field of two-axis tracking mirrors called heliostats to concentrate solar radiation onto a central receiver (Stine & Geyer, 2001). The central receiver is constructed on a large tower – hence the name ‘power tower’. HTF flows through the receiver and absorbs the concentrated thermal energy. This energy is then stored, and then used to generate electricity using a conventional steam cycle.

2.2.1. Development

The first large scale power tower plant was operated in California, USA between 1982 and 1988. Called Solar One, the 10 MW_e plant used a direct steam generation receiver and thermal oil mixed with rock and sand as a thermocline storage system (Flueckiger *et al.*, 2011).

In 1995 the Solar One plant was retrofitted with an increased number of heliostats and a HTF system that allowed for operation using molten salt. The plant was renamed as Solar Two. The 20 MW_e plant used solar salt as HTF and a direct storage medium (Moore *et al.*, 2010). The thermal energy storage was designed to deliver thermal energy at design point of the steam generator for three hours with rated hot and cold salt temperatures of 565 °C and 290 °C (Cabeza *et al.*, 2012).

Valuable experience was gained from the operation of Solar Two between 1995 and 1999. Lessons learnt from the molten salt receiver were well documented (Litwin & Park, 2002) and the construction and operation of the plant as a whole resulted in an official design basis document for molten salt power tower plants (Zavoico, 2001).

The next iteration of Solar One and Solar two was Gemasolar (also known as *Solar Tres*). Gemasolar is a 20 MW_e molten salt power tower plant currently under operation in Spain near Seville (García and Calvo, 2012; Burgaleta *et al.*, 2013). It has 15 hours of storage, which results in 24 hour electricity production using only solar energy.

The most recent molten salt power tower plant to come into operation is the Crescent Dunes 110 MW_e plant in the USA. This plant represents the state of the art molten salt solar power technology. It is equipped with a 1.2 million m² solar field and 10 hours of direct molten salt storage (Solar Reserve, 2016). A 110 MW_e molten

salt power tower is currently under construction in Chile with 17.5 hours of direct thermal storage (Abengoa Solar, 2016).

Power tower technology is also well suited to direct steam generation. The first commercial power tower was constructed in 1999 by Abengoa Solar Energy. PS10 (*Planta Solar 10*) is a 10 MW_e direct steam power tower (Osuna *et al.*, 2006). PS20 is the next iteration of direct steam generation technology, and it is situated next to PS10 in Abengoas Solucar Solar Complex. As the name suggests, PS20 is a 20 MW_e plant, it is equipped with a cavity type receiver and 1 hour of thermal storage using steam accumulators (Abengoa Solar, 2015a).

Ivanpah solar electric generating system in the Mojave Desert is the largest concentrating solar power complex in the world according to peak generating capacity (377 MW_e). The system is made up of three individual towers and uses direct steam generation technology with no thermal energy storage system (NREL, 2014).

Khi Solar One began operation in South Africa in 2015. This 50 MW_e plant uses direct steam generation together with steam accumulators for a small amount of thermal storage (Abengoa Solar, 2015b). Khi Solar One highlights one of the drawbacks of using direct steam generation – a high level of thermal storage is not feasible. A 100 MW_e molten salt power tower called Redstone is currently in development in South Africa. The plant will implement 12 hours of storage and use a dry-cooled power cycle due to water availability concerns in South Africa (SolarReserve LLC., 2016).

Currently the use of molten salt as HTF and storage medium makes molten salt power towers more attractive than direct steam towers due to their storage capabilities and low operating pressures compared to steam.

2.2.2. Components

The major components of a power tower plants are the heliostat field and the central receiver (Figure 6).



Figure 6: Heliostats in the field (left) and the cavity receiver in operation (right) at PS20, Spain

The major components of a typical heliostat are a mirror, a support structure, a drive mechanism and a pylon (Vazquez *et al.*, 2006). The drive mechanism is a two-axis actuator system that is controlled by an on-board control system. The exact target location is determined by the control system of the plant.

The size (reflective area) of a heliostat is carefully selected for each plant to maximize the optical efficiency and reduce the cost of the heliostat field. Large heliostats ($\sim 120 \text{ m}^2$) result in a lower number of heliostats required for the same reflective area. This reduces cost by minimizing the amount of expensive components such as heliostat drives and controls. Large heliostats result in high levels of blocking and shading, which requires them to be more sparsely distributed in the field. Small heliostats ($\sim 2 \text{ m}^2$) experience lower levels of blocking and shading, which increases optical efficiency. Furthermore the wind loads on the heliostat are decreased, which results in more cost effective support structure and drive designs. Upon evaluation of the state-of-the-art plants (Table 4) it is evident that there is no consensus as to the optimum heliostat size for a power tower plant.

Table 4: Heliostat size selection for power tower plants (SolarReserve LLC., 2016; National Renewable Energy Laboratory, 2016b)

| Plant name | Capacity [MW _e] | Operation date | No. of heliostats | Reflecting area [m ²] |
|----------------|-----------------------------|----------------|-------------------|-----------------------------------|
| PS10 | 11 | 2007 | 624 | 120 |
| PS20 | 20 | 2009 | 1 255 | 120 |
| Gemasolar | 20 | 2011 | 2 650 | 115 |
| Ivanpah SEGS | 377 | 2013 | 173 000 | 15 |
| Crescent Dunes | 110 | 2015 | 10 347 | 116 |
| Khi Solar One | 50 | 2016 | 4 120 | 140 |
| Redstone | 100 | 2019 | $\sim 24\ 000$ | 48 |

Heliostat fields contain a large array of heliostats ranging from hundreds to thousands depending on the intended thermal power and the heliostat size. The heliostats are arranged so as to avoid optical interference with one another through blocking and shading. Field arrangements vary from plant to plant. In the northern hemisphere, a northern solar field relative to the receiver has the highest optical efficiency – examples of this type of field are PS10 and PS20 near Seville, Spain (Osuna *et al.*, 2006). In the southern hemisphere, a southern solar field results in higher optical efficiency – this is implemented at Khi Solar One in South Africa (Abengoa Solar, 2015b). One-sided fields tend to be associated with cavity type receivers, which operate at high efficiencies; however they have small acceptance angles.

Surrounding heliostat field arrangements are implemented at Gemasolar (García & Calvo, 2012) and Crescent dunes (Solar Reserve, 2016) plants. These fields surround the receiver tower completely, with an increased number of heliostats to the northern side of the tower to increase optical efficiency.

Receivers can be divided into two main types: Cavity and external receivers (Augsburger, 2013). Cavity receivers are protected from the atmosphere with an opening towards the one sided solar field. A wider acceptance angle can be allowed by using multiple cavities, such as at Khi Solar One in South Africa, which uses three cavities. An external receiver has no protection from the atmosphere but it has the benefit of working with a surrounding field. External receivers are typically cylindrical in shape such as those implemented at Gemasolar and crescent dunes. Ivanpah uses external receivers with a four-sided flat geometry rather than a cylindrical one.

2.2.3. Cost

Kolb *et al.* (2011) compiled a roadmap to cost reduction for power tower technology. They assessed the current costs of power towers and proposed focus areas for cost reduction. Table 5 lists the cost components for power towers in 2011, as well as potential cost components that may be attainable in 2020.

Table 5: Capital expenses for a power tower plant (Kolb *et al.*, 2011)

| Capital expense component | 2011 | 2020 | Unit |
|---------------------------|------|------|-----------------------|
| Site improvements | 20 | 20 | USD/m ² |
| Heliostat field | 200 | 120 | USD/m ² |
| Receiver and tower | 200 | 170 | USD/kW _{th} |
| Thermal energy storage | 30 | 20 | USD/kWh _{th} |
| Steam turbine system | 1000 | 800 | USD/kW _e |
| Steam generating system | 350 | 250 | USD/kW _e |

Turchi *et al.* (2013) reported on a component-based cost model that was developed specifically for molten salt power tower plants. The report used the molten salt power tower roadmap (Kolb *et al.*, 2011) as a starting point, and went on to propose updated values for the major components of a plant (Table 6). Kurup & Turchi (2015) updated the findings of Turchi *et al.* (2013) with indexed prices for 2015. The indexed prices are also listed in Table 6.

Table 6: Capital expenses for a molten salt power tower plant (Turchi *et al.*, 2013)

| Capital expense component | 2013 | 2015 | Unit |
|---------------------------|------|------|-----------------------|
| Site improvements | 15 | 16 | USD/m ² |
| Heliostat field | 180 | 170 | USD/m ² |
| Receiver and tower | 173 | 173 | USD/kW _{th} |
| Thermal energy storage | 27 | 26 | USD/kWh _{th} |
| Steam turbine system | 1200 | 1190 | USD/kW _e |
| Steam generating system | 350 | 340 | USD/kW _e |

2.3. Molten salt as heat transfer fluid

When selecting a fluid to use as HTF and a storage medium, Heller (2013) recommends a number of appropriate thermophysical properties. The fluid should have a low freezing point and a high maximum operating temperature. The fluid should also have a high conductivity - the receiver tube is then allowed to operate at a similar temperature to the HTF temperature which reduces thermal losses. A low viscosity is beneficial as it reduces pumping losses. High fluid density coupled with a high heat capacity results in a high thermal capacity; this makes the fluid a suitable storage medium. The material should have a low corrosivity to preserve the life of the pumps, valves and joints that make up the system. The fluid should not be toxic, flammable or hazardous to the environment. Finally, the fluid should be readily available at a low cost. A comparison of the key characteristics and thermophysical properties of thermal oil and molten salt are listed in Table 7.

Table 7: Comparison of thermal oil and solar salt thermophysical properties

| Property | Unit | Thermal Oil | Molten salt | References* |
|--------------------------|-------------------|-------------|-------------|-------------|
| Melting point | °C | 15 | 222 | (1),(2) |
| Minimum temperature | °C | 292 | 290 | (3),(4) |
| Maximum temperature | °C | 393 | 593 | (1),(5) |
| Operating pressure range | Bar | 11 | 1-20 | (1),(5) |
| Operating density range | kg/m ³ | 815-673 | 1940-1720 | (1),(5) |
| Heat capacity | kJ/kg K | 2.37-2.73 | 1.49-1.55 | (1),(5) |
| Thermal conductivity | W/m K | 0.095-0.077 | 0.50-0.55 | (1),(5) |
| Viscosity | mPa s | 0.25-0.12 | 3.50-1.03 | (1),(5) |
| Cost | USD/kg | 2.10 | 0.50 | |

*1-Dow Chemical Company (2001), 2-Archimede Solar Energy (2016), 3-Llorente García *et al.* (2011), 4-Burgaleta *et al.* (2013), 5-Wagner (2008).

In conventional parabolic trough plants, thermal oil is used as HTF and solar salt as a storage medium. The most common oils in use are *Dowtherm® A* (Dow Chemical Company, 2001) and *Therminol® VP-1* (Solutia Incorporated, 2013). The main disadvantages of using thermal oil are the upper temperature limit (400 °C), the degradation of the oil over time, the high cost and the flammability.

As discussed in previous sections, much of the development using trough and tower technology implements molten salt HTF and a direct storage medium. In 2010, *Centro de investigaciones energéticas medioambientales y tecnológicas* (CIEMAT) constructed an experimental plant for thermal storage using molten salts at its PSA facilities. This facility evaluated components, instrumentation and operation strategies in order to support to the industry in the development of molten salt technology (Rodríguez-garcía *et al.*, 2014)

Many studies have investigated the use of an ‘improved’ salt sold commercially as HitecXL - a ternary salt consisting of 48 % Ca(NO₃)₂, 7 % NaNO₃, and 45 % KNO₃ (Becker, 1980) (Ruegamer *et al.*, 2013). The benefit of HitecXL is its lower freezing temperature of 142 °C (Bauer *et al.*, 2013), with the compromise of a slightly lower operating temperature of ~500 °C. However, Ruegamer *et al.* (2013) found that the implementation of HitecXL resulted in a higher LCOE in trough and tower technology than conventional solar salt. Furthermore, Hitec XL showed decomposition at temperatures in the range of 450-465°C, which resulted in it being eliminated as a potential HTF by Abengoa Solar (Abengoa Solar, 2013b). Solar salt was shown to be chemically stable up to temperatures of 600 °C (Abengoa Solar, 2013a).

Conventional solar salt (sometimes called Hitec *Solar Salt*) has been shown to allow for higher operation temperatures and increased power block efficiencies. It is shown to significantly reduce the LCOE of a parabolic trough plant by ~20 % (Ruegamer *et al.*, 2013). The use of molten salt in power tower technologies has also been proved in the operation of Solar Two and Gemasolar as documented in the previous section.

2.4. Concentrating solar power in South Africa

South Africa has seen three CSP projects completed in the recent years. Four more projects are underway, all scheduled to be operational by 2019 (Doe, 2015). The REIPPPP was introduced in 2011. In Round 1 and Round 2 of the REIPPPP, 200 MW_e of CSP capacity was awarded. The feed-in tariff implemented was constant, and notably higher than those of wind and photovoltaic technologies. (Relancio *et al.*, 2015).

In 2013, the feed-in tariff for CSP plants was changed to a two-tier structure in response to the peak demand for electricity in the evening times (Figure 7), especially in winter (Figure 7). The details of the two-tiered tariff structure are listed in Table 8.

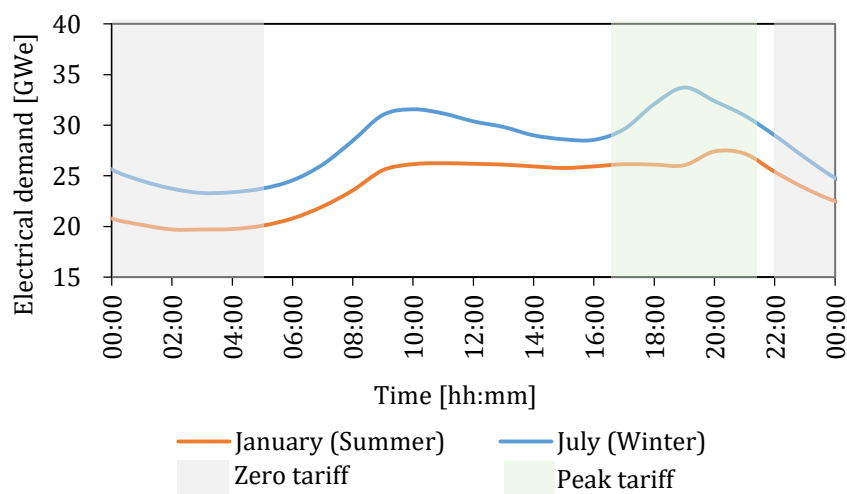


Figure 7: Typical demand on the South African electrical grid in summer and winter including the tariff periods for Renewable Energy Independent Power Producer Procurement Program Round 3 and 3.5

Table 8: Two-tiered feed-in tariff structure for Round 3 and Round 3.5 of the Renewable Energy Independent Power Producer Procurement Program (Relancio *et al.*, 2015; Department of Energy, 2013)

| Name | Hours | Tariff [%] | Tariff [ZAR/kWh] |
|----------|---------------|------------|------------------|
| Standard | 05:00 – 16:30 | 100 | 1.65 |
| | 21:30 – 22:00 | | |
| Peak | 16:30 – 21:30 | 270 | 4.46 |
| Night | 22:00 – 05:00 | 0 | 0.00 |

Since changing the feed in tariff, 200 MW_e capacity has been awarded in Round 3.5. An additional 450 MW_e of CSP capacity has been allocated for Round 4.5, where the preferred bidders are to be announced in the 4th quarter of 2016 (Department of Energy *et al.*, 2015).

An evaluation of the appropriate technologies for CSP development in South Africa was carried out by Fichtner *et al.* (2010), who investigated conventional parabolic trough and molten salt power tower technologies. The report on the investigation includes detailed system design of these plants, which are referred to in Sections 3, 4 and 5.

The yield of a CSP plant is primarily dependent on solar DNI; however site selection cannot be performed based on solar resource alone (Dinter & Busse, 2015). The International Renewable Energy Agency (IRENA) study (Wu *et al.*, 2015b) performed an investigation focused on the multi-criteria analysis for planning renewable energy in Africa. The study is accompanied by a renewable energy zone map (Figure 8) and a site selection tool. The multi-criteria (MC) scoring considers levelized cost of electricity (LCOE) along with other criteria that improve site suitability such as distance from transmission lines and roads, slope, population density, land use, and capacity factor.

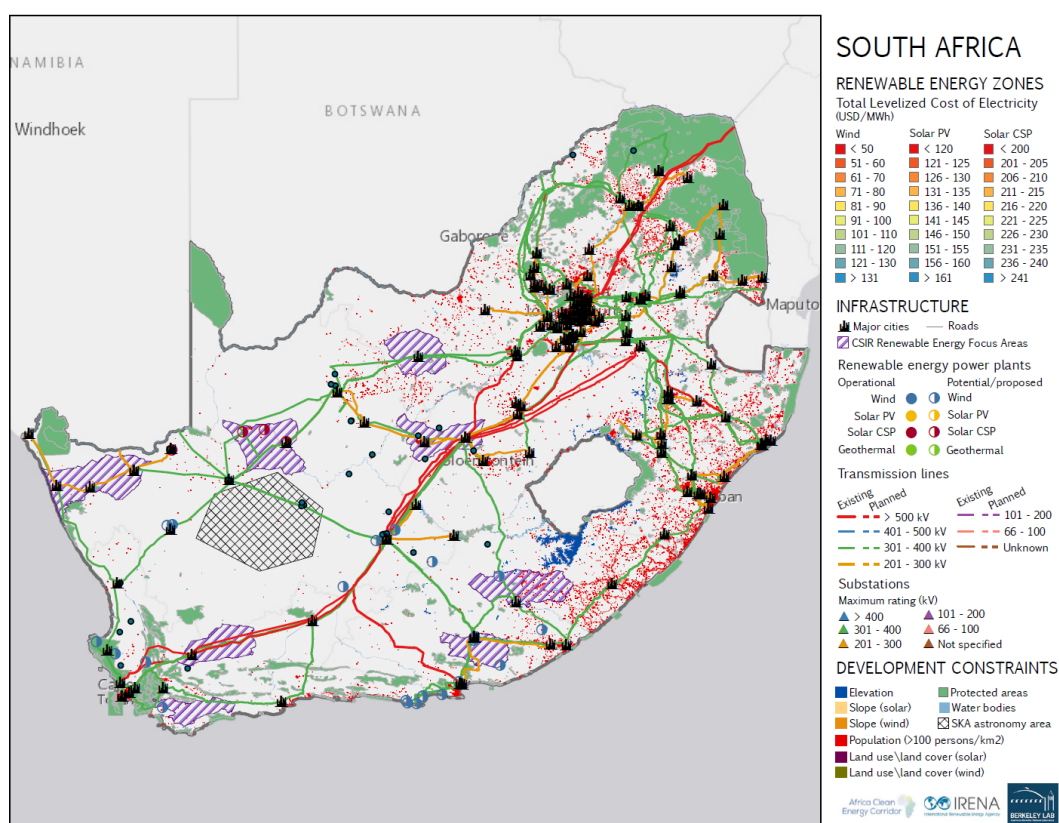


Figure 8: International Renewable Agency renewable energy map for South Africa (Wu *et al.*, 2015a)

The IRENA map in Figure 8 uses CSIR renewable energy focus areas (Rycroft, 2015). These are areas in South Africa with the most favourable solar resource, transmission line access, water availability and proximity to load centres.

2.5. High temporal resolution irradiance data

2.5.1. Direct normal irradiance data

The electrical yield of a CSP plant is primarily dependent on the amount of direct normal irradiance (DNI) available to a site. For this reason, the measurement and accuracy of DNI data is important for yield analysis.

DNI is measured using a pyrheliometer. This is an instrument that uses a collimated detector to measure radiation directly from the sun and small portion of sky surrounding it (Duffie & Beckman, 2013). Pyrheliometers are typically part of a solar resource measurement station.

Most of the available irradiance data from historical and satellite derived sources are hour averaged. However, in order to accurately calculate the daily yield of a CSP plant, it is essential to account for high-resolution temporal variability of the site data (Meyer *et al.*, 2009).

The reason that hourly averaged DNI data is not acceptable for accurate yield analysis of a CSP plant is because hourly measurements are too infrequent to capture the transient effects of clouds (Grantham *et al.*, 2013). The transient nature of DNI causes a nonlinear response of a CSP plant. The effect of using minute averaged data as opposed to hour averaged data has been investigated when modelling a parabolic trough plant (Beyer *et al.*, 2010). It was found that using hourly data resulted in an overestimation of daily electrical energy yield of between 10 % and 20 %. Various methods of synthetic DNI generation resulted in improved yield analysis.

The Southern African Universities Radiometric Network (SAURAN) is a regional network of sixteen solar monitoring stations, which provides a free source of minute averaged DNI data in Southern Africa. The data is accessible to the public via a website interface.

Each of the SAURAN stations measure DNI, diffuse horizontal irradiance (DHI), global horizontal irradiance (GHI) as well as other meteorological data. The data is available in time-averaged formats over 1-minute, hourly and daily intervals. The aim of SAURAN is to provide a long-term record of solar resource in Southern Africa, a region that shows high potential for the implementation of various solar energy technologies (Brooks *et al.*, 2015).

2.5.2. Generating high resolution direct normal irradiance data

In order to utilize the high resolution DNI data measured using SAURAN, a method of combining available hourly averaged data at a site and the high resolution ground measured data is available. The method proposed by Fernández-Peruchena *et al.*, (2015) uses a technique for the nondimensionalization of a series of ground measured, high frequency daily DNI curves.

The process of nondimensionalization transforms each measured day into a dimensionless signature that can be used to create high resolution DNI data from hourly DNI data. The process is described in depth in Appendix A.

2.6. Simulation of concentrating solar power plants

A SolarPACES working group is currently working on a Guideline to Solar Modeling (*guiSmo*). The focus is accurate yield calculation of solar thermal plants (Hirsch *et al.*, 2015). The challenges for standardized methodologies for yield analysis of CSP technologies are identified by the working group. Many of the challenges relate to the nature of CSP as a technology, which results in a plant layout that is highly variable.

The *guiSmo* working group goes on to describe that direct validation using existing plants is not always possible because operational data is highly restricted by the plant owners. Even when operational data is available, the methods of data acquisition are often insufficient for significant model validation.

The *guiSmo* group has provided initial modelling guidelines in a publication at SolarPACES 2015. The guide suggests that steady state assumptions are acceptable with a 10 minute or smaller temporal resolution. It is advised that the solar field is modelled with empirical and physical sub-models and that the power cycle be modelled using mass flow rates and enthalpies. The use of look-up tables is advised when considering the main power cycle impact variables such as thermal power input, HTF input temperature and wet/dry bulb temperature. Thermal energy storage models are advised to use mass flow rates and enthalpies rather than summing up heat fluxes in order to account for deviations from nominal operating conditions.

The guideline goes on to describe the idea that detailed process simulations are often too complex to implement in comparison to the benefit they offer in terms of accuracy. It is advised that annual yield analysis should use simplified approaches to complement a steady state model with proper consideration of transient effects.

Operating strategies are given as the most representative options:

- Pure solar driven (suitable for flat rate tariffs)
- Solar driven with a minimum load during the night
- Load curve driven
- Price driven (similar to the two-tiered tariff described in the REIPPPP)

Finally, it is advised that weather data should typically incorporate 10 years of measurement. When this is not fulfilled at planned sites, the combination of high quality ground measurements and satellite measurements for long term data is required.

2.6.1. Simulation tools

There are existing total system models, most notably NREL's System Advisor Model (SAM). SAM is a performance and financial model designed to facilitate decision making for people involved in the renewable energy industry (NREL, 2015). SAM has a strong financial model, especially when considering development in the US with associated tax incentive and government subsidies. SAM is coupled to a user

friendly graphic user interface, however, the source code to the software is not freely available.

Greenius is an alternative to SAM and it is primarily applicable for feasibility studies where the available information about technology and equipment is typically limited and a large number of simulation runs are required. Comparison of different technologies at a single site is possible with Greenius and it can be used to elaborate the pros and cons of a given CSP technology (Dersch *et al.*, 2010).

SOLERGY simulates the operation and annual power output of a solar thermal power plant. It utilizes weather data at time intervals as short as 3 minutes and calculates the net electrical energy output including parasitic power requirements over a 24-hour day. The code is written in FORTRAN77, and input to the code is entered via user-specified text files, which makes using the software a cumbersome task (Ehrhart & Gill, 2013).

TRNSYS: STEC is a collection of TRNSYS models especially developed to simulate solar thermal power generation (Noureddine & Kamal, 2012). The solar thermal electricity component (STEC) simulation models are intensively used in feasibility studies for solar thermal power projects, as well as in research programs for new solar thermal power technologies. The STEC is a free add-on, however, the TRNSYS program is commercial (Schwarzbözl & Zentrum, 2006).

Additional commercial tools for CSP applications include Epsilon Professional (steag, 2016) and Thermoflow (Thermoflow Inc., 2016) – both of which contain solar thermal add-ons.

2.7. Conclusion

Both power tower and parabolic trough technologies using molten salt as HTF have been identified as having high potential for generation of dispatchable electricity at a low cost. Molten salt has been identified as a more appropriate HTF and storage medium compared to thermal oil. For this reason, molten salt power towers and troughs will be compared going forward in the study.

South Africa has shown to be an ideal location for CSP development thanks to the REIPPPP and the high levels of DNI. South Africa is therefore selected as a relevant location for comparison of molten salt parabolic trough and power tower plants. The IRENA map has provided insight into preferred sites within South Africa for a CSP plant; this data will be used to select sites for the simulation of CSP plants using both the selected technologies.

While there are existing tools for CSP plant modelling – the development of a plant model from the ground up gives in-depth knowledge of how the model is constructed, and provides a fair means of comparison for the two technologies. The initial discussions on the guideline for solar modelling will be followed in the construction of both the parabolic trough and power tower plant models.

3. Parabolic trough plant description

There are no large-scale molten salt parabolic trough plants in operation in the world today. This section proposes the basic system level design of a 100 MW_e molten salt parabolic trough plant. In sections to follow, the operation of the plant is discussed and a detailed simulation model of a molten salt parabolic trough plant is presented.

The feed-in tariff structure has a large influence on the design on a CSP plant (Kost *et al.*, 2012). If we consider the two tariff structures previously implemented in the REIPPPP – the first was a flat tariff structure, which means that plant operators are paid the same rate for electricity generated at any time of the day. The second is a two-tiered tariff structure, which means that the plant operators are only paid for certain hours during the day.

Plants optimized to operate under a flat tariff tend to have an optimum design with a large solar field and large thermal energy storage. They will then tend to operate as a base load power station. Plants optimized to operate under the two-tiered tariff typically have smaller solar fields and smaller thermal storage, which still enables the plan to produce electricity during times of peak demand.

There is currently no indication as to whether future plants in South Africa will be used as peaking plants or as base load plants. For this reason plant designs are carried out to fit both the two-tiered and the flat REIPPPP tariff structure.

3.1. Overview

The molten salt selected for HTF and storage is solar salt (binary mixture, 40 % KNO₃ — 60 % NaNO₃). Solar salt has an upper temperature limit of 600 °C and a freezing point of 228 °C (Kelly, 2010). The plant is operated between recommended molten salt temperatures of 290 °C and 565 °C. The high upper temperature limit allows for the parabolic trough technology to be directly compared to molten salt power tower technology with its high power cycle efficiency and low storage costs (Ruegamer *et al.*, 2013).

A 100 MW_e generating capacity was selected as it is in line with previous plants developed under the REIPPPP. The size of the parabolic trough solar field is varied from location to location. The component selection at each location is the kept constant, as well as the general solar field layout. Figure 9 illustrates the basic design of the plant and Table 9 gives a generic solar field description. Descriptions of the solar collector and receiver tubes can be found in the sections to follow.

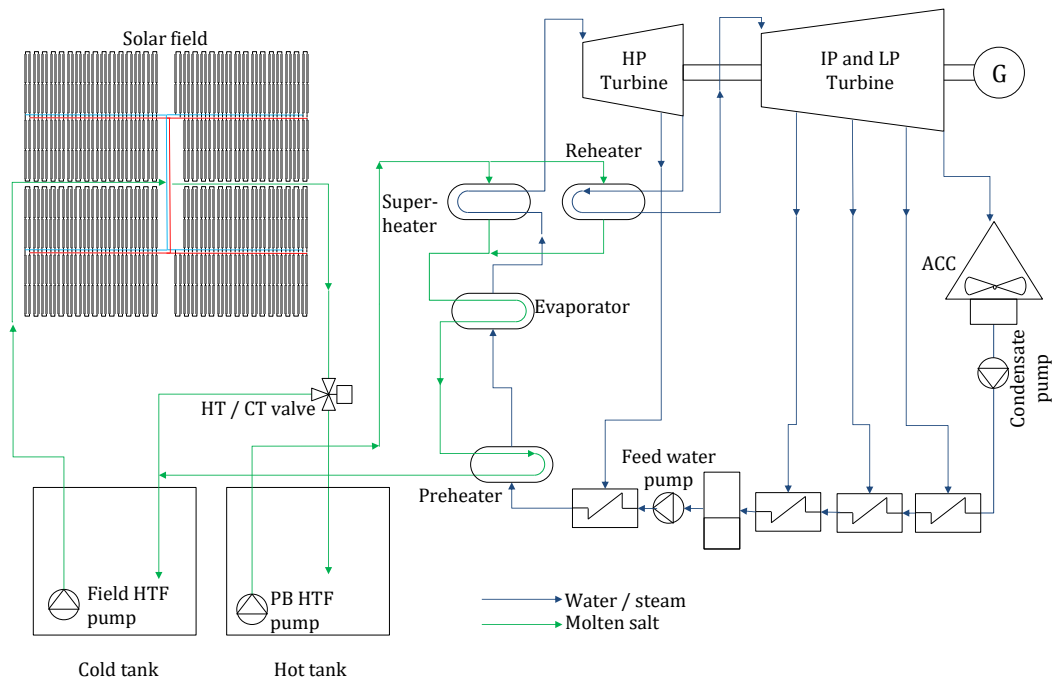


Figure 9: Molten salt parabolic trough plant design

During operation at design point, molten salt HTF at 290 °C is pumped from the cold tank to the solar field. The HTF returns at 565 °C and is stored in the hot tank. During electricity production, the HTF is pumped from the hot tank, through the steam generating system and back to the cold tank. A detailed operating strategy is described in Section 5.

Table 9: Parabolic trough solar field description

| Parameter | Value | Unit |
|--------------------------------|--|--------------------------|
| Plant location | South Africa (6 sites) | - |
| Annual DNI | 2400 – 2800 | kWh/m ² ·year |
| Design point DNI | 947 - 1013 | W/ m ² |
| Collector configuration | 4 Ultimate Trough SCAs | - |
| Collector orientation | North South | - |
| Receiver type | HCMS-11 (60 per SCA) | - |
| Number of loops | 100 – 200 | - |
| Solar field size | 750 000 – 1 300 000 | m ² |
| Heat transfer fluid | Solar salt (KNO ₂ and NaNO ₃) | - |
| Solar field inlet temperature | 565 | °C |
| Solar field outlet temperature | 290 | °C |

3.2. Solar collector

When selecting a solar collector design it was found that an increased aperture trough is beneficial for a number of reasons. An increased aperture results in an increased concentration ratio, which allows higher attainable fluid temperatures. An increased aperture also results in more incident energy available per unit length of receiver tube, which in turn allows for shorter SCA lengths with equivalent energetic gain. A shorter receiver tube length results in lower thermal losses in the solar field (Riffelmann *et al.*, 2013b).

Ultimate Trough solar collectors by FLABEG (Schweitzer *et al.*, 2013) were selected for the plant. The Ultimate Trough has a 7.5 m aperture and has demonstrated high levels of optical efficiency. Each Ultimate Trough solar collector is made up of a torque box, and parabolic shaped cantilever arms, which support the mirror panels. The structure is supported by pylons, and at a single pylon for each SCA, a hydraulic drive is included to tilt the trough to follow the sun (Kurup *et al.*, 2015).

Table 10: Ultimate Trough solar collector assembly specifications

| Parameter | Value | Unit |
|-----------------|-------------------|----------------|
| Length | 247 | m |
| Aperture | 7.51 | m |
| Reflective area | 1716 | m ² |
| Drive system | 1 hydraulic drive | per SCA |

3.3. Receiver tube

Ultimate Trough solar collectors can accommodate a range of receiver tubes from 60 mm to 110 mm in diameter. Based on photogrammetry and deflectometry measurements from a prototype Ultimate Trough collector, FLABEG have performed ray tracing to determine the intercept factor for receiver tubes ranging from 60 mm to 110 mm in diameter (Richert & Nava, 2012). The intercept factor determines how much of the concentrated radiation is intercepted by the receiver tube. Larger diameter receivers have higher intercept factors.

Large diameter receiver tubes also result in a lower pressure drop for the HTF flowing through them, which is beneficial as it reduces the pumping losses of the plant. However, larger diameter receiver tubes allow for higher thermal losses in the field as well as a lower concentration ratio and therefore lower attainable HTF temperatures. Richert & Nava (2012) found that the optimum receiver tube diameter when using Ultimate Trough solar collectors is 70 mm, therefore 70 mm receiver tubes have been selected for the plant design in this study.

A background of the available receiver tubes was given in Section 2.1.2. There are many receiver tube manufacturers available; however the majority of products are designed and optimized for thermal oil HTF and a maximum operating temperature of 400 °C. There are currently only two high temperature tubes available in the CSP market – The Schott PTR 70 HT and the Archimede Solar Energy HCEMS-11. In order to operate at temperatures >550 °C, the receiver tubes are required to use thicker stainless steel absorber tubes and have improved selective coating durability at high temperatures.

For the design plant, HCEMS-11 molten salt tubes (Table 11) developed by Archimede Solar Energy were selected. HCEMS-11 tubes are the only high temperature receiver tubes available on the market today that have been proven to withstand extended operation at high temperature (Matino & Maccari, 2015).

Although the HCEMS-11 receiver tubes have an operation temperature of 550 °C, it has been assumed that they could withstand operation at 565 °C as the selective coating has been tested at temperatures above 600 °C.

Table 11: Receiver tube specifications

| Parameter | Value | Unit |
|-------------------------------|----------------------------|------|
| Length | 4.06 | m |
| Absorber tube outer diameter | 70 | mm |
| Absorber tube thickness | 3 | mm |
| Absorber tube material | Stainless steel (AISI 321) | - |
| Glass tube outer diameter | 125 | mm |
| Glass tube thickness | 3 | mm |
| Glass tube material | Borosilicate glass | - |
| Maximum operating temperature | 580 | °C |

3.4. Solar field layout

The solar field layout was based on existing parabolic trough plants. A typical 'H' shaped solar field layout is used, which divides the solar field into four main sections. Using an 'H' shaped field has been shown to be an optimal compromise between pressure losses and cost effectiveness for large scale parabolic trough plant (Riffelmann *et al.*, 2011).

A single loop in the field is made up of four Ultimate Trough SCAs connected in series. Each SCA accommodates 60 HCEMS-11 receiver tubes. The number of individual loops in a plant varies depending on the location and the design point solar multiple. Cold HTF at approximately 290 °C is pumped from the cold tank through the cold runner pipe to a cold header pipe. From the header pipe it is diverted to an individual loop in the field. The HTF is heated in the loop to 565 °C and is fed into the hot header. The hot header joins to the hot runner pipe, which makes its way into the hot tank for storage of the HTF.

A solar field inlet temperature of 290 °C and a return temperature of 565 °C was selected. The high return temperature allows for a higher steam temperature and thus a more efficient Rankine cycle.

When designing a parabolic trough field with molten salt as HTF it is important to account for freeze protection, receiver tube filling and maintenance procedures. Site works and land preparation should ensure that each SCA loop is on a slope with the highest point at the bridge, and the lowest point at its connection to the header piping. This design allows for the passive draining of the loop and it assists in the drainage of the loop in the event of recovery from freezing (Donnola *et al.*, 2015).

The Archimede Solar Energy demonstration plant is equipped with Joule resistance heating for freeze protection and receiver tube preheating. Joule resistance heating involves the passing of electrical current through the absorber tube of the receiver to increase its temperature. While this has shown to be an effective measure of freeze protection, it results in large parasitic consumption during filling and requires increase capital expenditure on electrical equipment in the field. If HTF temperature remains well above the freezing point of molten salt then the resistance heating will not be used during operation.

For freeze protection a method proposed by Kearney *et al.* (2004) has been implemented into the operation strategy. This involves using energy from the

thermal energy storage system overnight and during times of low irradiation to prevent the HTF temperature dropping below freezing temperature.

Refer to Appendix B for further information regarding the operating strategy. For further information concerning the parasitic losses associated with pumping of the HTF refer to Section 5.7.

3.5. Thermal energy storage

The parabolic trough plant and the power tower plants designed in this study use the same thermal energy storage and power cycle systems. This is possible because both plant designs use the same HTF and have similar operating temperatures.

The thermal energy storage (TES) system is similar to that of Gemasolar in that it is a direct molten salt TES. It comprises of a hot and a cold molten salt tank. The TES is sized to store enough energy to allow for design point electrical generation for a predetermined number of hours. The hot tank receives hot HTF (565 °C) from the solar field where it is stored. When required, the tank then supplies this hot HTF to the power block to generate electricity.

The cold tank stores cold (290 °C) molten salt either from the power block or the solar field during recirculation. Energetic losses from the storage tanks have been considered in line with experience with Spanish CSP plants with molten salt thermal storage the average losses are 1 °C, over a 24 hour period (Dinter & Gonzalez, 2013). The specifications for the storage system are listed in Table 12. A conventional two-tank molten salt storage was selected as it has a proven track record at Gemasolar. Thermocline thermal storage has shown the potential for further cost reduction, however, it has not been proven on a commercial scale at this time.

Table 12: Thermal energy storage specifications

| Parameter | Value | Units |
|---|-----------------|-------|
| Type | Two-tank | - |
| Storage fluid | Solar salt | - |
| Capacity (full load) | 6 – 16 | hours |
| Salt mass | 13 480 – 33 240 | ton |
| Hot tank operating temperature | 565 | °C |
| Hot tank maximum temperature | 570 | °C |
| Cold tank operating temperature | 290 | °C |
| Cold tank freeze protection temperature | 275 | °C |

The hot tank is constructed using primarily stainless steel to withstand the thermal stress and corrosion associated with molten salt at 565 °C. The cold tank will be constructed out of carbon steel as it only has to withstand temperatures of ~300 °C.

3.6. Power cycle

The power cycle is a Rankine cycle, which is used to convert the thermal energy collected into electrical energy. Molten salt from the hot tank is pumped into the steam generating system. The steam generating system consists out of a preheater,

evaporator, superheater and reheater Figure 9. The steam then passes through a high, medium and low pressure turbine.

An air-cooled condenser (ACC) condenses the turbine steam. An ACC is used due to the scarcity of water in South Africa. The design point details of the power cycle are listed in Table 13. The power cycle system is illustrated in the plant overview in Section 3.1.

Table 13: Power cycle design parameters

| Parameter | Value | Units |
|------------------------------------|--------------|------------------|
| Gross turbine - generator output | 100 | MW _e |
| Turbine HP inlet pressure | 120 | bar |
| Turbine HP inlet temperature | 555 | °C |
| Ambient temperature design point | 32 | °C |
| ACC initial temperature difference | 20 | °C |
| Thermal power from HTF | 240 | MW _{th} |
| Thermal to electric efficiency | 0.416 | - |
| HTF mass flow | 575 | kg/s |
| HTF input temperature | 565 | °C |
| HTF desired output temperature | 287 | °C |

3.7. Conclusion

The technology exists for a large scale molten salt parabolic trough plant. The plant design has been described using this technology. Due to the implementation of molten salt as HTF and storage medium – thermal energy storage systems and power cycles from molten salt power tower plant designs are used. This allows for increased simplicity when modelling both parabolic trough and power tower plants, which are described in the section to follow. The performance of the components described in this section and the system as a whole is described in Section 5.

4. Power tower plant description

Gemasolar and Solar Two are both molten salt power tower plants with a number of years of operating experience. The system-level design of these plants has been described in literature. This section uses lessons learned from these plants to provide a system-level description of a 100 MW_e molten salt power tower plant used for plant modelling in Section 5. The primary design areas are the heliostat field and the central receiver.

The design of the plant is once again determined by the feed-in tariff structure that is implemented. Plants designed to operate under a flat tariff structure tend to have an optimum design with a large heliostat field and central receiver with large thermal energy storage. They will then tend to operate as a base load power station. Plants designed to operate under the two-tiered tariff structure typically have smaller heliostat fields and receivers coupled to a smaller thermal storage, which still enables the plan to produce electricity during times of peak demand.

4.1. Overview

The plant design is illustrated in Figure 10. The operating temperatures of Solar Two and Gemasolar were selected for this plant design. During design point operation molten salt HTF at 290 °C is pumped from a cold storage tank, up the tower and through the tubes of the central receiver during operation. The HTF is heated to 565 °C in the receiver and then returns to the hot storage tank. The HTF is pumped through the receiver panels in two parallel flow paths. The molten salt system is linked to the power cycle through a steam generator system.

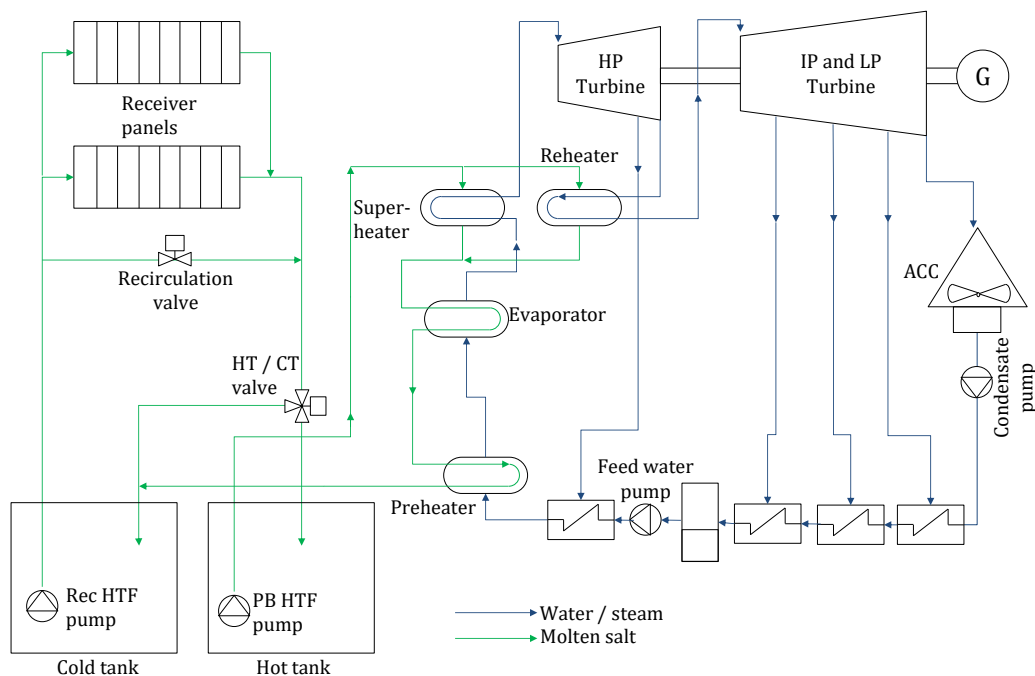


Figure 10: Molten salt power tower plant design

The operating temperatures are identical to those selected in the previous section for a molten salt parabolic trough plant. This is done intentionally as it provides a fair platform for the comparison of the two technologies. Due to the matching operating temperatures and HTF selection, the power tower and parabolic trough plants share the same thermal energy storage and power cycle systems.

4.2. Heliostat

The SENER heliostats installed at Gemasolar were selected for the plant design. While smaller heliostats may offer higher optical efficiency, there is no clear distinction as to the most economically viable solution as of yet. The large heliostats result in a lower number of heliostats in the field which would in turn result in a simpler operating control system as well as a reduction in expensive components such as heliostat controllers and drives. The details of the SENER heliostat are listed in Table 16.

Table 14: Heliostat design parameters

| Parameter | Value | Unit |
|--------------------------|--------|------|
| Width | 10.959 | m |
| Height | 10.950 | m |
| Pylon height | 5.675 | m |
| Reflective surface ratio | 0.958 | - |
| Slope error | 2.6 | mrad |
| Tracking error | 2.1 | mrad |

The solar field size changes from site to site when using the model. Typically plants use a heliostat field layout is optimized for their specific location and receiver design. A surrounding field circular heliostat field design, such as the one implemented at Gemasolar and Crescent Dunes, is implemented in the generic plant design.

Table 15: Power tower heliostat field description

| Parameter | Value | Unit |
|---------------------------|------------------------|--------------------------|
| Plant location | South Africa (6 sites) | - |
| Annual DNI | 2400 - 2800 | kWh/m ² ·year |
| Design point DNI | 947 - 1013 | W/ m ² |
| Heliostat reflective area | 120 | m ² |

4.3. Receiver

An external cylindrical receiver design is selected based on its suitability for using molten salt a HTF and its compatibility with a surround heliostat field. While a cavity receiver may result in lower thermal losses and higher efficiency, it would not allow for large scale nominal thermal power that is attainable using external receivers.

The receiver design uses a concept from the thermal resistance receiver model designed by de Meyer *et al.* for a proposed plant in South Africa. The external receiver is to be constructed out of 16 panels. The HTF flow regime involves a cross

over flow, where the molten salt enters from the southern side and exits from the northern side of the receiver. The nominal receiver design at 575 MW_{th} uses the receiver height and diameter from Table 16. The tower height and the receiver size is scaled according to the nominal thermal design point of the receiver at each of the sites.

Table 16: Receiver design parameters (De Meyer *et al.*, 2015)

| Parameter | Value | Unit |
|--------------------------------|--|-------------|
| Receiver type | External cylindrical | - |
| Heat transfer fluid | Solar salt (KNO ₂ and NaNO ₃) | - |
| Receiver width | 19.2 | m |
| Receiver height | 16.3 | m |
| Parallel flows | 2.0 | - |
| Number of panels | 16.0 | - |
| Tube outer diameter | 50.0 | mm |
| Tube thickness | 1.5 | mm |
| Solar field inlet temperature | 565.0 | °C |
| Solar field outlet temperature | 290.0 | °C |

4.4. Conclusion

The heliostat field and receiver have been selected to represent a state-of-the-art power tower plant. The thermal energy storage and power cycle are identical to those described in Section 3. The performance of these components and the system as a whole is described in Section 5.

5. Plant modelling

In previous sections both parabolic trough and power tower plants using molten salt as HTF have been described. This section describes the models that were built to simulate the operation of these plants.

The Matlab® Simulink (The MathWorks Inc., 2015b) environment was used to construct the model components. Simulink allows for each of the main components of the plant to be managed as smaller sub-components. Both models use a third order, explicit solver (ode3, Bogacki-Shampine) with a fixed time step of 10 seconds.

The modelling of each plant can be divided into the input data, the plant simulation and the control system (Figure 11). In the section to follow, each of the plant simulation model components is described together with its required input data and generated output data.

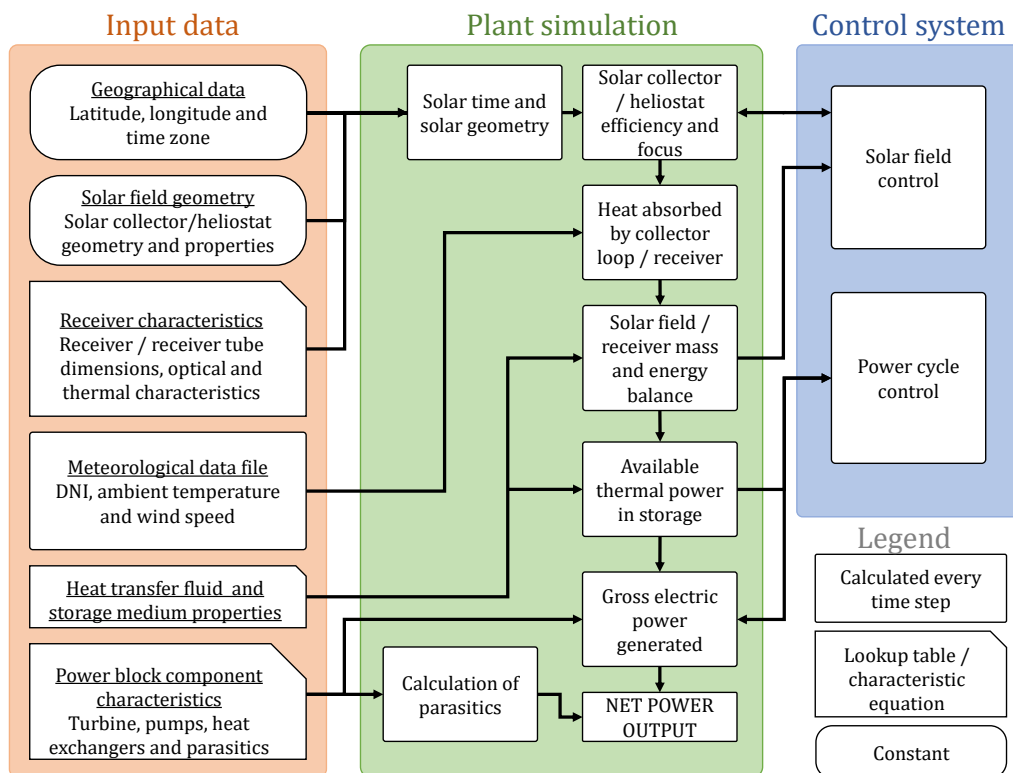


Figure 11: Generic parabolic trough and power tower model schematic diagram

5.1. Solar time and solar geometry

The first function of the model is to calculate the solar time and geometry at the selected site. The solar time and geometry model is used for both the parabolic trough and power tower models.

The sites geographical data is used to calculate solar time (t_s) from the local time (Simulink clock time) according to the procedure prescribed by Stein & Geyer (2001). The procedure makes use of the local clock time (LCT) in 24-hour format.

$$t_s = LCT + \frac{EOT}{60} - LC - D \quad (5.1)$$

Where EOT represents the Equation of Time, LC represents longitude correction and D represents the daylight savings modifier. The equation of time is calculated as follows, using Table 17 where the day number is defined as N .

$$EOT = 60 \sum_{k=0}^5 \left[A_k \cos\left(\frac{360kN}{365.25}\right) + B_k \sin\left(\frac{360kN}{365.25}\right) \right] \quad (5.2)$$

Table 17: Coefficients for the equation of time

| k | A_k | B_k |
|-----|--------------------------|--------------------------|
| 0 | 2.0870×10^{-4} | 0 |
| 1 | 9.2869×10^{-3} | -1.2229×10^{-1} |
| 2 | -5.2258×10^{-2} | -1.5698×10^{-1} |
| 3 | -1.3077×10^{-3} | -5.1602×10^{-3} |
| 4 | -2.1867×10^{-3} | -2.9823×10^{-3} |
| 5 | -1.5100×10^{-4} | -2.3463×10^{-4} |

In Equation 5.3 the correction for the difference in longitude between the plant and the time zone meridian is calculated as follows:

$$LC = \frac{\phi - \phi_{tmz}}{15} \quad (5.3)$$

The daylight savings modifier is a simple Boolean operator. This adjusts for daylight savings if it is implemented in the country in question.

$$D = \begin{cases} 1 & \text{if Daylight savings} \\ 0 & \text{Default} \end{cases} \quad (5.4)$$

Now that the solar time has been calculated, the exact position of the sun relative to the solar field can be calculated. The required solar geometry is the zenith angle (θ_z), the azimuth angle (γ_s) and the incidence angle (θ_i). The zenith angle is calculated first using Equation 5.5.

$$\theta_z = \pi - \sin^{-1}(\sin \delta \sin \phi + \cos \delta \cos \omega \cos \phi) \quad (5.5)$$

Equation 5.5 requires the declination angle (δ), the hour angle (ω) and the latitude coordinate of the site (ϕ).

$$\delta = \sin^{-1}(0.39795 \cos [0.98563(N - 3)]) \quad (5.6)$$

$$\omega = 15(t_s - 12) \quad (5.7)$$

The azimuth angle is calculated in Equation 5.8 (Duffie & Beckman, 2013).

$$\gamma_s = \text{sign}(\omega) \left| \cos^{-1} \left(\frac{\cos \theta_z \sin \phi - \sin \delta}{\sin \theta_z \cos \phi} \right) \right| \quad (5.8)$$

The model assumes that the parabolic trough field is orientated in the North – South direction. The incidence angle for a north-south orientated field is calculated using Equation 5.9.

$$\theta_i = \cos^{-1}(\cos^2 \theta_z + \cos^2 \delta \sin^2 \omega)^{\frac{1}{2}} \quad (5.9)$$

The zenith angle (θ_z), the azimuth angle (γ_s) and the incidence angle (θ_i) are sent to the solar collector component to model the optical performance of the solar field. A summary of the inputs and outputs of the solar time and geometry model is illustrated in Figure 12.

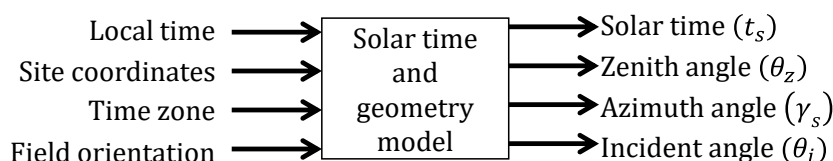


Figure 12: Summary of solar time and geometry model inputs and outputs

The solar time and zenith angle are used in the solar field control system. The zenith, azimuth and incident angles are used in the solar field calculations for both the parabolic trough and power tower models.

5.2. Parabolic trough solar field

The parabolic trough solar field is made up of two main subcomponents: the solar collectors and the receiver tubes. The connection of the receiver tubes via the solar field piping system results in a solar field energy balance.

5.2.1. Solar collector model

As described in Section 2.1.2, the solar collector is a parabolic shaped mirror assembly that concentrates radiation onto the receiver tube. The incidence angle between the aperture normal of a solar collector and the incident solar radiation is shown in Figure 13. The total available radiation on the solar field is equal to the product of the measured DNI and the cosine of the incidence angle ($\cos \theta_i$). The radiative flux focused on the receiver tube ($\dot{q}_{incident}$) is calculated in Equation 5.10.

$$\dot{q}_{incident} = DNI \cos \theta_i \eta_{opt, trough} \quad (5.10)$$

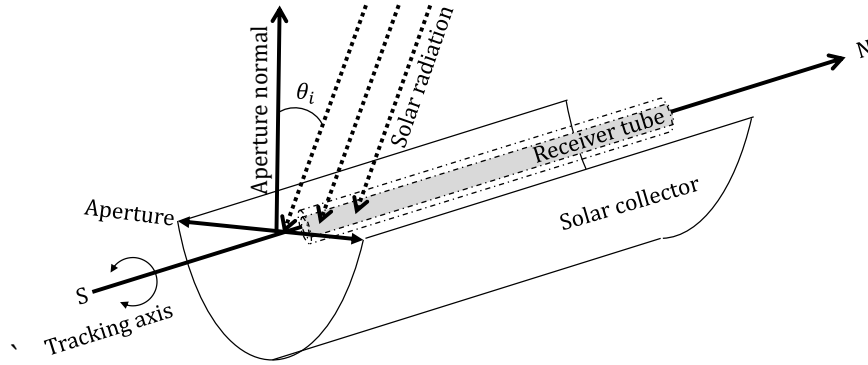


Figure 13: Solar collector assembly diagram showing the incident angle

The solar collector assembly (SCA) that is modelled is the Ultimate Trough by FLABEG (Riffelmann *et al.*, 2013b). Based on photogrammetry and deflectometry measurements from a prototype Ultimate Trough collector, FLABEG have performed ray tracing to determine the optical performance characteristics. The optical efficiency of the SCA (η_{opt}) is made up of a fixed optical efficiency ($\eta_{opt,0^\circ}$), shadowing efficiency (η_{shadow}), end loss efficiency ($\eta_{end\ loss}$) and an incident angle modifier (*IAM*).

$$\eta_{opt,trough} = \eta_{opt,0^\circ} \eta_{shadow} \eta_{end\ loss} IAM(\theta_i) \quad (5.11)$$

The fixed optical efficiency ($\eta_{opt,0^\circ}$) is calculated using a variety of material properties and performance factors, which are measured experimentally by the manufacturer (Table 18). The SCA performance is determined using a 70 mm diameter receiver tube.

$$\eta_{opt,0^\circ} = \rho_0 \gamma_0 \gamma_{track} cf \quad (5.12)$$

Table 18: Solar collector performance characteristics with a 70 mm receiver tube (Riffelmann *et al.*, 2013b)

| Parameter | Variable | Value [%] |
|----------------------------|------------------|-----------|
| Mirror reflectance | ρ_0 | 94.0 |
| Geometry / optical defects | γ_0 | 97.0 |
| Tracking / alignment error | γ_{track} | 99.8 |
| Cleanliness factor | cf | 97.0 |

The shadowing, end losses and IAM are calculated at every time step by the model because they are dependent on solar geometry. Shadowing is a result of one row of solar collectors casting a shadow onto the adjacent row. The shading efficiency is calculated in Equation 5.13 (Stuetzle, 2002). Shading is a function of the spacing between collector rows ($L_{spacing}$) and the aperture of the solar collector (W).

$$\eta_{shadow} = \frac{L_{spacing} \cos \theta_z}{W \cos \theta_i} \quad (5.13)$$

End losses are a result of a portion of the receiver tube not receiving focused radiation from one end of the solar collector row. The end losses can be calculated using Equation 5.14 (Lippke, 1995).

$$\eta_{\text{end loss}} = 1 - \frac{L_{\text{focus}} \tan \theta_i}{L_{\text{SCA}}} \quad (5.14)$$

The incidence angle modifier for a 70 mm receiver tube was calculated by FLABEG from measurements at the Ultimate Trough test loop. The incidence angle is calculated using Equation 5.15 (Riffelmann *et al.*, 2013a)

$$IAM(\theta_i) = 1 - 0.008 \frac{\theta_i}{\cos \theta_i} - 0.117 \frac{\theta_i^2}{\cos \theta_i} \quad (5.15)$$

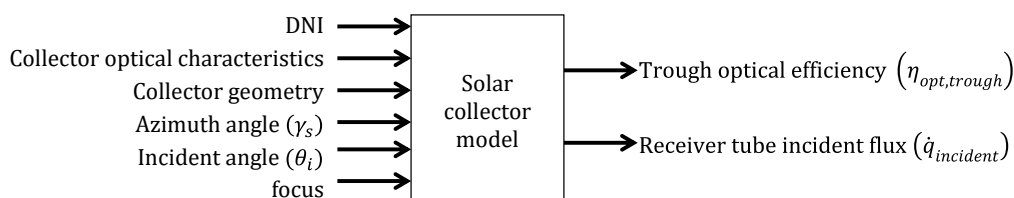


Figure 14: Solar collector model inputs and outputs

The troughs optical efficiency is sent to the solar field control system and the receiver tube incident flux is sent to the receiver tube model. The solar collector model is also influenced by focus control, as described in Appendix B.

5.2.2. Receiver tube model

As described in Section 2.1.2, the receiver tube is a stainless steel absorber tube within an evacuated glass tube. The absorber tube is coated in a spectrally selective material to increase its absorptivity and decrease its emittance.

The Archimedes Solar Energy HCEMS-11 receiver tubes (Table 11) have been selected for this model. The performance modelling of the receiver tube relies on performance data from the receiver tube manufacturer. Figure 15 represents the simplified energy balance of the receiver tube.

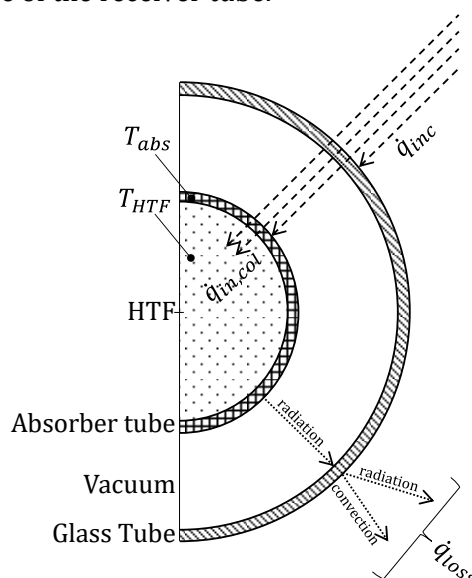


Figure 15: Receiver tube energy diagram

The characteristics of the glass tube and the selective coating on the absorber tube are used to determine the flux that is absorbed into the HTF ($\dot{q}_{in,col}$) from the incident flux on the receiver tube ($\dot{q}_{incident}$). The geometrical and optical characteristics are listed in Table 19.

$$\dot{q}_{in,col} = \dot{q}_{incident} \eta_{opt,rec} \quad (5.16)$$

Table 19: Receiver tube geometrical and optical performance characteristics

| Parameter | Variable | Value [%] |
|---|-----------------|-----------|
| Transmissivity of glass tube | τ_{glass} | 96.6 |
| Absorptivity of the selective coating | α_{rec} | 95.0 |
| Ratio of bellow length to receiver length | η_{bellow} | 93.6 |
| Cleanliness factor of glass tube | cf_{rec} | 96.0 |

The optical efficiency of the receiver tube ($\eta_{opt,rec}$) is then calculated as the product of the performance characteristics in Table 19:

$$\eta_{opt,rec} = \tau_{glass} \alpha_{rec} \eta_{bellow} cf_{rec} \quad (5.17)$$

Equations 5.16 and 5.17 are adapted from Wagner & Gilman (2011) with the assumption that the conductivity through the stainless steel absorber tube and the convection coefficient into the HTF are sufficiently high to allow for all of the incident radiation to be absorbed. There are, however, several loss mechanisms when considering the incident concentrated radiation on the receiver tube. The first losses occur at the glass tube. Glass tube reflectivity (τ_{glass}) and the absorbance (α_{rec}) of the glass tube intercept the concentrated flux before it reaches the absorber tube. Of the incident flux on the receiver tube, the absorbance of the spectrally selective coating on the absorber tube then determines how much energy is absorbed into the stainless steel tube, and subsequently into the HTF.

During operation, the temperature of the HTF and the absorber tube will rise. The high temperature difference between the absorber tube and the glass tube result in radiation losses to the glass tube. Convection losses are kept to an absolute minimum due to the vacuum between the absorber tube and the glass tube. From the outer surface of the glass tube, convection and radiation losses take place to the atmosphere. In a simplified approach, the heat loss is modelled using the empirical heat loss equation supplied by the manufacturer.

The heat loss (\dot{q}_{loss}) from the receiver tube is governed by radiative heat transfer and is therefore primarily dependant on the temperature of the absorber tube (T_{abs}) (Matino & Maccari, 2015). Burkholder & Kutscher (2009) find that ambient temperature and wind conditions don't significantly affect evacuated HCE heat loss. They accredit this insensitivity of HCE heat loss to ambient conditions to small heat transfer values between the absorber and the glass tube.

The heat loss coefficients for the HCEMS-11 are given in Table 20 and the heat loss curve is illustrated in Figure 16. Should the vacuum of the receiver tube fail, or the glass tube break, the heat loss will increase dramatically. This is accounted for by estimating that a small portion of the tubes in the field will have broken or have a

vacuum failure. The heat loss curve is then a weighted average of the curves for the three receiver tube variants.

$$\dot{q}_{loss} = c_1 T_{abs} + c_4 T_{abs}^4 \quad (5.18)$$

Table 20: Receiver tube performance characteristics (Matino & Maccari, 2015)

| Condition | c_1 | c_4 | Weighting |
|--------------|-------|----------|-----------|
| Standard | 0.18 | 7.5E-09 | 0.980 |
| Broken glass | 1.01 | 8.0 E-09 | 0.015 |
| Lost vacuum | 0.50 | 7.9 E-09 | 0.005 |

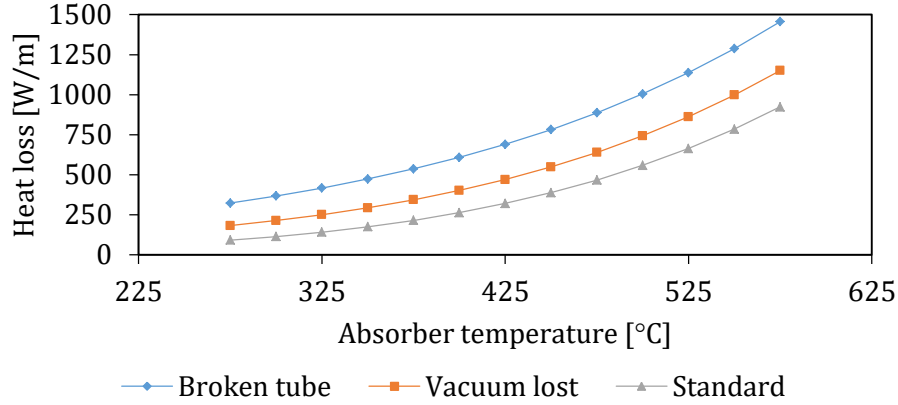


Figure 16: Heat loss curves for the Archimede Solar Energy HCEMS-11 receiver tube

Rather than using an iterative energy balance at every control volume, it is assumed that the absorber temperature (T_{abs}) is 5 °C higher than the bulk HTF temperature (T_{HTF}) during solar field operation (Figure 15). This assumption is based on the low thermal resistance of the stainless steel absorber tube and the turbulent internal flow of the HTF compared to the high thermal resistance (insulation) of the evacuated glass tube. During recirculation overnight, the absorber tube is assumed to be equal to the HTF temperature.

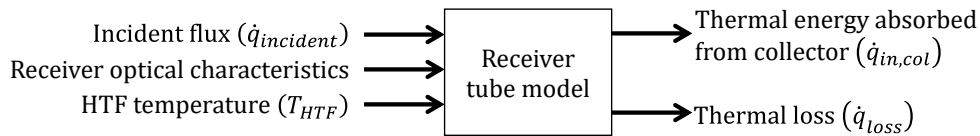


Figure 17: Receiver tube model inputs and outputs

The receiver tube model sends the thermal energy absorbed and thermal loss data to the solar field energy balance model.

5.2.3. Solar field energy balance

The process developed by Wagner & Gilman (2011) is followed when performing the solar field energy balance using single sections of the receiver tube. The energy balance is implemented at every time step during the simulation (Figure 18).

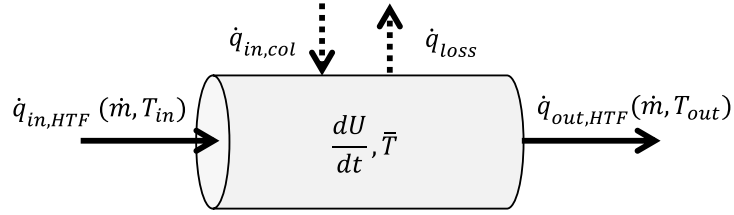


Figure 18: Solar field energy balance control volume

$$\Delta T = T_{out} - T_{in} = \frac{\dot{q}_{abs}}{\dot{m} c_{HTF}} \quad (5.19)$$

The control volume in Figure 18 represents an energy balance between the incoming and outgoing mass flows, the energy absorbed from the collector and the energy loss to the environment. The internal energy term represents the change in internal energy with respect to time. The change in internal energy can also be expressed as:

$$\frac{\partial U}{\partial t} = (m_{HTF} c_{HTF} + m_{SCA} c_{p,SCA}) \frac{\partial T}{\partial t} \quad (5.20)$$

It is assumed that the thermal capacity of the molten salt in the tube is substantially greater than the thermal capacity of the thin stainless steel tubes of the SCA ($m_{HTF} c_{HTF} \gg m_{SCA} c_{p,SCA}$), therefore Equation 5.20 can be simplified to:

$$\frac{\partial U}{\partial t} = m_{HTF} c_{HTF} \frac{\partial T}{\partial t} \quad (5.21)$$

If the net energy absorbed is represented as the difference between the energy absorbed from the collector and the loss to the environment:

$$\dot{q}_{abs} = \dot{q}_{in,col} - \dot{q}_{loss} \quad (5.22)$$

Then the energy balance over the control volume is simplified as follows:

$$\dot{q}_{in,HTF} + \dot{q}_{abs} = \frac{\partial U}{\partial t} + \dot{q}_{out} \quad (5.23)$$

If the incoming and outgoing energy due to mass flow is simplified using an average temperature (\bar{T}) with a linear temperature distribution.

$$\begin{aligned} \dot{q}_{in} - \dot{q}_{out} &= \dot{m} c_{HTF} (T_{in} - T_{out}) \\ &= 2 \dot{m} c_{HTF} (T_{in} - \bar{T}) \end{aligned} \quad (5.24)$$

By substituting Equation 5.24 and Equation 5.21 into Equation 5.19, a first order differential equation for the change in temperature of the control volume can be derived:

$$\frac{\partial \bar{T}}{\partial t} = \frac{2 \dot{m} (T_{in} - \bar{T}) + \dot{q}_{abs}}{\dot{m} c_{HTF}} \quad (5.25)$$

The general solution to Equation 5.25 is:

$$\bar{T} = \frac{\dot{q}_{abs}}{2 \dot{m} c_{HTF}} + C_1 \exp \left[-\frac{2 \dot{m}}{m} \Delta t \right] + T_{in} \quad (5.26)$$

By enforcing the boundary condition that $\bar{T} = \bar{T}_0$ when $t = 0$, and considering the linear approximation for average temperature ($\bar{T} = (T_{out} + T_{in})/2$), the solution for the constant C_1 is found as:

$$C_1 = \bar{T}_0 - \frac{\dot{q}_{abs}}{2 \dot{m} c_{HTF}} - T_{in} \quad (5.27)$$

By substituting the integration constant from equation 3.24 into the general solution, the equation to calculate the outlet temperature of a control volume is determined:

$$T_{out} = \frac{\dot{q}_{abs}}{\dot{m} c_{HTF}} + T_{in} + 2 \left(\bar{T}_0 - \frac{\dot{q}_{abs}}{2 \dot{m} c_{HTF}} - T_{in} \right) \exp \left[-\frac{2 \dot{m}}{m} \Delta t \right] \quad (5.28)$$

The control volume used for the model is the receiver tube volume of a single SCA. This results in four control volumes per loop. Therefore the outlet temperature of a single SCA is calculated using the net energy absorbed (\dot{q}_{abs}) by the receiver tubes, the mass of HTF in the SCA (m), the thermal capacity of the HTF in the SCA (c_{HTF}), mass flow rate (\dot{m}), the time step (Δt), the inlet temperature (T_{in}) and the average temperature of the SCA from the previous time step (\bar{T}_0).

The thermal capacity and the mass of the HTF in the SCA are a function of the average temperature in the SCA from the previous time step. The HTF mass is calculated using the receiver tube volume of a single SCA ($V_{rec,SCA}$), the density of the HTF (ρ) and the thermal capacity (c_{htf})

$$m = \rho(\bar{T}_0) V_{rec,SCA} \quad (5.29)$$

There are two additional control volumes that have been considered for the modelling of the solar field; the hot and cold header lines. Using a method similar to the one previously described, the outlet temperature of the header lines has been derived, taking into account the transient nature of the mass flow in the large diameter piping:

$$T_{out} = T_{h,0} \exp \left[-\frac{\dot{m}}{\bar{V}_h \rho_h} \Delta t \right] + T_{in} \quad (5.30)$$

In the case of the hot header line, T_{out} represents the inlet temperature into the hot tank and T_{in} is the outlet temperature of the last SCA in the loop. For the cold header line, T_{out} represents the inlet temperature to the first SCA and T_{in} is the cold tank temperature.

Figure 19 shows how the different solar field components are implemented in the parabolic trough model. The performance of the solar field is modeled according to a single loop which is made up of four SCAs connected in series (refer to Figure 59 for

scale). The energetic gains are multiplied by the number of loops in the field (N_{loops}). The trough optical model uses the DNI, wind, focus and solar geometry to calculate the optical efficiency of the troughs at each time step using Equations 5.11 to 5.15. The influence of wind and focus is determined by the system control described in Appendix B.

The incident radiative flux on each length of receiver tubes is used for SCA energy balances. The energy balance for each SCA uses Equation 5.16 to 5.29 to determine the outlet temperature of the SCA. The outlet temperature of the cold header and the hot header are calculated using Equation 5.30. The temperature into the cold header ($T_{CT,out}$) is equal to the cold tank temperature.

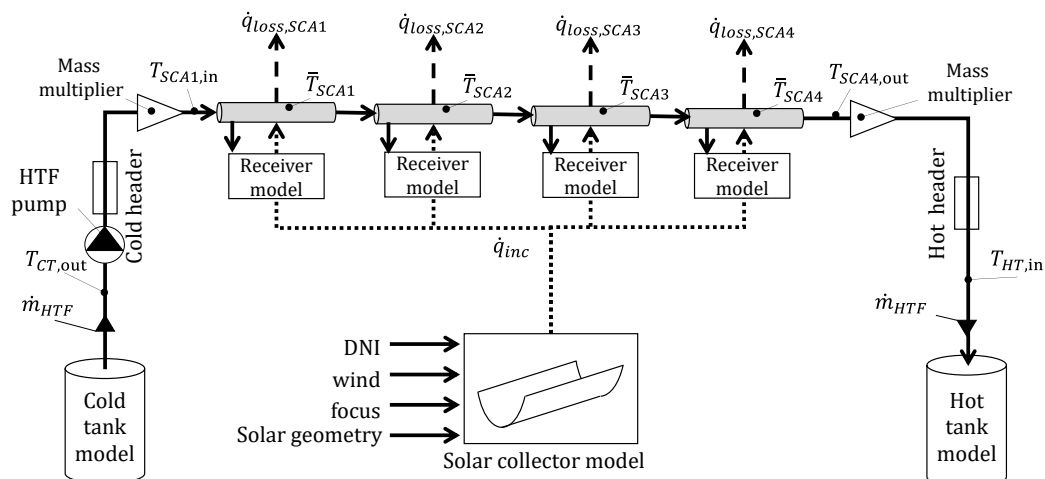


Figure 19: Solar field energy balance diagram showing the connection of the solar collector, receiver tube and thermal energy storage models.

The mass flow rate is determined by the HTF pump controller and the number of loops in the solar field. The mass flow rate is set by the system control described in Section Appendix B and is constant throughout the loop.

5.2.4. Sizing of the solar field

A Matlab® (The MathWorks Inc., 2015a) script is used to determine the design point performance of the plant and size of the solar field before the simulation process begins. A design point of solar noon on the Vernal equinox is selected (12:00 solar time, 20th of March 2016).

The script loads the DNI, wind and ambient temperature data from a file. The required solar geometry is calculated for the design point: the zenith angle (θ_z), the azimuth angle (γ_s) and the incidence angle (θ_i).

The design point DNI is defined as the 95th percentile of the DNI data set (excluding zero values). This design point results in a larger solar field for locations with lower DNI and vice versa.

The sizing of the solar field begins with the calculation of the required thermal power, given the solar multiple. The solar multiple (SM) is defined as the design point thermal power delivered by the solar field relative to the design point thermal

power required for power cycle operation. The design point thermal power for the power cycle is taken as: $\eta_{PC,dp} = 0.417$ (Section 5.5). The thermal design point thermal power is then:

$$P_{th,dp} = P_e / \eta_{PB,DP} \quad (5.31)$$

The required thermal power from the solar field can then be calculated using the given solar multiple for the plant:

$$P_{th,SF} = P_{th,DP} SM \quad (5.32)$$

In order to estimate the required solar field area needed to meet the design point thermal power, the solar field efficiency at design point is required. The combined optical efficiency of the solar collector and the receiver tube can be expressed as follows:

$$\eta_{SF} = \eta_{opt,trough} \eta_{opt,rec} \cos \theta_i \quad (5.33)$$

The solar geometry at design point is used to calculate the optical efficiency of the solar collector ($\eta_{opt,trough}$) and the cosine factor ($\cos \theta_i$).

The sizing of the solar field uses an energy balance method for a single loop of the field. The thermal power into a single loop at design point can be calculated using the design point DNI, the optical efficiency of an SCA, and the aperture area of a full loop.

$$P_{th,in,loop} = DNI \eta_{SF} A_{loop} \quad (5.34)$$

The aperture area of a single loop is calculated using the SCA geometry given in Table 10. A design point thermal loss from the receiver tube is calculated using the average temperature of the loop and the heat loss equation of the receiver tube (Equation 5.18). A linear temperature distribution through the loop is assumed to calculate the average temperature. The absorber temperature is assumed to be 5 °C hotter than the bulk fluid temperature during operation.

$$\bar{T}_{DP} = \frac{(T_{out} + T_{in})}{2} + 5 \quad (5.35)$$

$$\dot{q}_{loss,dp} = c_1 \bar{T}_{DP} + c_4 \bar{T}_{dp}^4 \quad (5.36)$$

An energy balance over a single loop is used to determine the amount of thermal energy delivered to the HTF per loop:

$$P_{th,net,loop} = P_{th,in,loop} - \dot{q}_{loss,dp} L_{loop} \quad (5.37)$$

The number of loops required to meet the thermal design point of the plant is then calculated as the design point thermal power divided by the power delivered by a single loop (rounded up to the nearest whole number). The total aperture area of the solar field is thereby the product of the number of loops and the aperture area per loop.

$$N_{loop} = \left[\frac{P_{th,DP}}{P_{th,net,loop}} \right] \quad (5.38)$$

$$A_{SF} = N_{loop} A_{loop} \quad (5.39)$$

5.3. Power tower solar field

The power tower solar field consists of the heliostat field and the receiver. The modelling of each of these components is described in this section.

5.3.1. Heliostat Field

In power tower plants, the heliostat field concentrates the incident radiation in the field onto the receiver near the center of the field. The radiative power reflected by the field that is incident on the receiver is calculated as follows:

$$\dot{Q}_{rec} = DNI A_{SF} \eta_{opt,0} \eta_{opt,field} \quad (5.40)$$

The power focused on the receiver is therefore a function of the DNI at that time step, the reflective area of the solar field (A_{SF}), the fixed optical efficiency of the heliostats ($\eta_{opt,0}$), and the optical efficiency of the field at that timestep ($\eta_{opt,field}$).

The fixed optical efficiency is determined by the performance parameters of the heliostats. It accounts for the reflectivity ($\eta_{refl} = 0.95$) and the cleanliness ($cf = 0.95$) of the mirror surface. Also included in the fixed optical efficiency are the spillage (η_{spill}) and atmospheric attenuation factors (η_{atten}).

$$\eta_{opt,0} = \eta_{refl} cf \eta_{att} \eta_{spill} \quad (5.41)$$

Spillage losses represent the fraction of the radiation reflected by the heliostat field that does not concentrate on the receiver surface. The spillage losses of individual heliostats increase as the distance from the receiver increases. Furthermore, a slope error as a result of heliostat manufacturing will increase the spillage losses. In order to reduce spillage losses a larger receiver or more accurate heliostats can be used. Spillage losses can be accurately calculated using ray tracing software and literature has estimated spillage losses for Gemasolar to be between 5 % (Rinaldi *et al.*, 2013) and 10 % (Augsburger, 2013) of the total concentrated radiation. The model assumes a spillage loss of 10 %, resulting in a spillage efficiency of $\eta_{spill} = 0.9$.

Atmospheric attenuation is caused by the reflected beam from the heliostat being diffused and absorbed by the ambient air it passes through before it reaches the receiver. This attenuation is sensitive to the air quality of the site, and the level attenuation is typically attributed to the range of visibility in the field. Attenuation in the field increases as the distance from the heliostat to the receiver increases. This model uses a correlation developed by Hottel (1975) for a dry location with a high range of visibility (23 km). The distribution of heliostats in the field is not calculated, therefore a representative heliostat at half the total radius from the receiver ($r/2$) is used to calculate the attenuation efficiency for the field as a whole:

$$\eta_{att} = 1 - [0.6739 + 10.46 r - 1.7 r^2 + 0.2845 r^3] \quad (5.42)$$

Calculation of individual blocking, shading and cosine losses for heliostats in the field requires the design, optimization and evaluation of a heliostat field layout, which is beyond the scope of this study. Rather than designing the layout of individual heliostats in the field and calculating a field efficiency using individual heliostat efficiencies, the modeled optical efficiency of the heliostat field is calculated using a polynomial developed by Gauché *et al.*, (2012). Originally developed for the Gemasolar plant with a tower height of 140 m, this polynomial utilizes the fact that heliostat field efficiency has a primary dependence on the solar zenith angle. The polynomial accounts for blocking, shading and cosine losses.

$$\eta_{opt,field} = 0.4254 \theta_z^6 - 1.148 \theta_z^5 + 0.3507 \theta_z^4 + 0.755 \theta_z^3 - 0.5918 \theta_z^2 + 0.0816 \theta_z + 0.832 \quad (5.43)$$

When compared to field efficiencies for larger plant designs (Figure 20) with tower heights greater than 260 m, the use of the polynomial is shown to estimate lower efficiencies at higher zenith angles. This indicates that the polynomial efficiency implemented is more conservative than previous studies. For further information on heliostat efficiency refer to the detailed heliostat field calculations carried out by Collado *et al.* (2006) and Augsburg (2013).

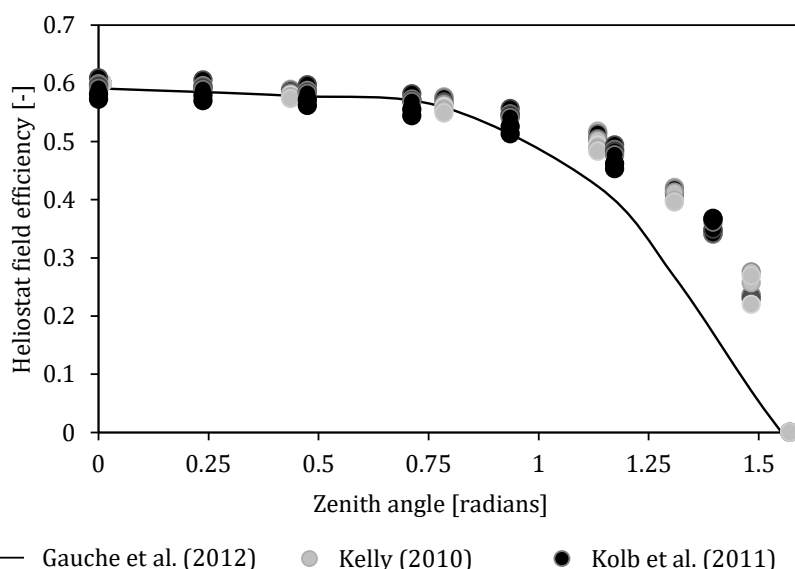


Figure 20: Heliostat field efficiency vs. zenith angle (Gauché *et al.*, 2012; Kelly, 2010; Kolb *et al.*, 2011)

Figure 21 shows a summary of the heliostat field model inputs and outputs. The receiver incident power is sent to the receiver model.

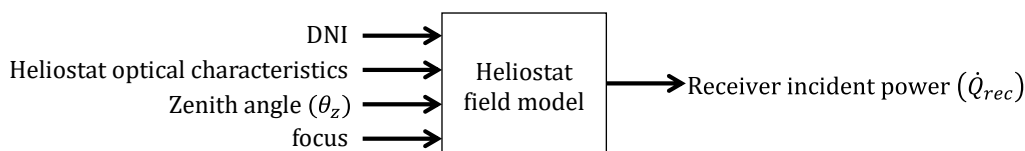


Figure 21: Heliostat field model inputs and outputs

5.3.2. Receiver

The receiver design is adapted from the thermal resistance receiver model designed by de Meyer *et al.* (2015) for a proposed plant in South Africa. The external receiver is to be constructed out of 16 panels with tube diameters of 50 mm and a thickness of 1.5 mm. The HTF flow regime involves a cross over flow, where the molten salt enters from the southern side and exits from the northern side of the receiver.

The net energy absorbed by the HTF (\dot{Q}_{HTF}) is calculated using the product of the incident energy focused onto the receiver multiplied by the receiver efficiency.

$$\dot{Q}_{HTF} = \dot{Q}_{rec} \eta_{rec} \quad (5.44)$$

The efficiency of the receiver is primarily dependent on the incident thermal power and the wind speed it is exposed to. Ambient temperature further influences the performance of the receiver, however, to a lesser degree. The receiver efficiency (η_{rec}) is calculated using the curves represented in Figure 22.

The thermal resistance modelling of the receiver by de Meyer *et al.* was performed with a fixed design point of 575 MW_{th}. To allow for a variety of receiver sizes, the receiver model assumes this performance curve relative to the design point gross power of the receiver. The relative gross power onto the receiver is a term used to define how far from the design point the receiver is operating: $\dot{Q}_{rec}/\dot{Q}_{rec,DP}$. The relative gross power is used to calculate the receiver efficiency from the data in Figure 22.

The wind speed at the height of the receiver (V_{rec}) is calculated using the measured wind speed (V_0) 10 m above ground level (H_0). The Hellman exponential law is used to extrapolate the measured wind speed to the height of the receiver (H_{rec}). The friction coefficient (p) depends on the type of landscape where the wind speed is measured. Touma (1977) recommends a friction coefficient of $p = 1/7$ for a wide range of terrains including grasslands and scrublands, typical of CSP plant locations.

$$V_{rec} = V_0 \times \left(\frac{H_{rec}}{H_0}\right)^p \quad (5.45)$$

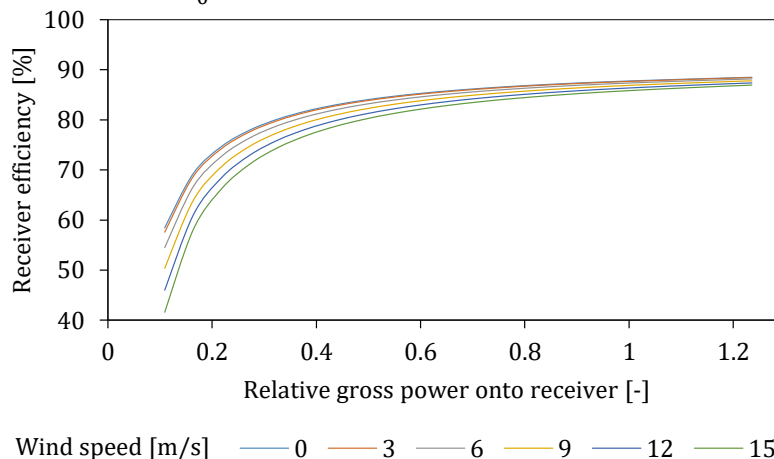


Figure 22: Receiver efficiency curve according to wind speed at the receiver height and incident thermal power

The receiver model uses the incident thermal power to calculate the thermal power absorbed by the HTF. An energy balance method similar to the one described in Section 5.2.3 is used to calculate the outlet temperature of the receiver. The receiver is treated as a lumped control volume:

$$T_{out} = \frac{\dot{q}_{HTF}}{\dot{m} c_{htf}} + T_{in} + 2 \left(\bar{T}_0 - \frac{\dot{q}_{HTF}}{2 \dot{m} c_{htf}} - T_{in} \right) \exp \left[-\frac{2 \dot{m}}{m} \Delta t \right] \quad (5.46)$$

The outlet temperature of the receiver is calculated using the power absorbed (\dot{q}_{HTF}) by the HTF flowing through the receiver, the mass of HTF in the receiver (m), the thermal capacity of the HTF (c_{htf}), mass flow rate (\dot{m}), the time step (Δt), the inlet temperature (T_{in}) and the average temperature of the receiver from the previous time step (\bar{T}_0).

The thermal capacity and the mass of the HTF in the SCA are a function of the average temperature in the SCA from the previous time step. The HTF mass is calculated using the receiver tube volume of a single SCA and the density.

$$m = \rho(\bar{T}_0) V_{rec} \quad (5.47)$$

There are two additional control volumes that have been considered for the modelling of the receiver: the riser and the downcomer within the tower. Using a method similar to the one previously described, the outlet temperature of the riser and downcomer have been derived, taking into account the transient nature of the mass flow in the large diameter piping:

$$T_{out} = T_{h,0} \exp \left[-\frac{\dot{m}}{\bar{V}_h \rho_h} \Delta t \right] + T_{in} \quad (5.48)$$

In the case of the downcomer, T_{out} represents the inlet temperature into the hot tank and T_{in} is the outlet temperature receiver. For the riser, T_{out} represents the inlet temperature to the receiver and T_{in} is the cold tank temperature.

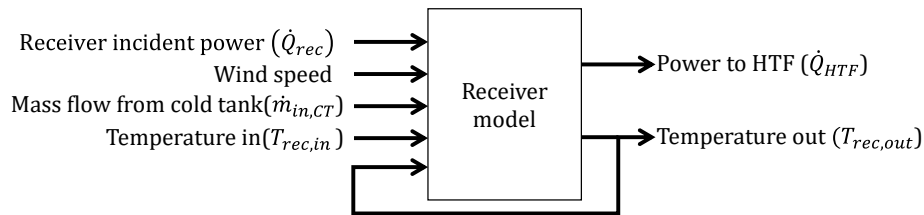


Figure 23: Summary of inputs and outputs for the receiver model

The interconnection of the models for the thermal energy storage, the riser and downcomer as well as the receiver and heliostat field models are illustrated in Figure 24.

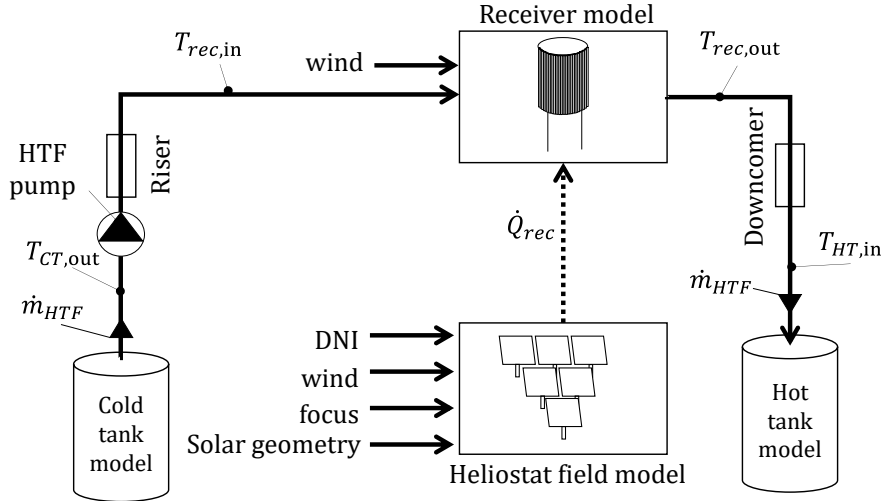


Figure 24: Linking the heliostat field and receiver models to the thermal energy storage models

5.3.3. Sizing of the solar field

The required thermal power from the solar field during design point operation is calculated using identical process to Section 5.2.4. Once again the design point is calculated at solar noon on the Vernal equinox is selected (12:00 solar time, 20th of March 2016). The design point ambient temperature is 30 °C and the design point wind speed for the receiver efficiency calculation is 3 m/s.

The thermal power required from the solar field in Equation 5.32 ($P_{th,SF}$) is set as the design point thermal power to the HTF from the receiver ($\dot{Q}_{HTF} = P_{th,SF}$). The solar field area is calculated using the receiver and the heliostat field efficiencies under design point conditions:

$$A_{SF} = \frac{\dot{Q}_{HTF}}{\eta_{opt,0} \eta_{opt,field} \eta_{rec}} \quad (5.49)$$

Equations 5.43 to 5.41 and data from Figure 22 are used to calculate the heliostat field and receiver efficiencies at design point.

5.4. Thermal energy storage system model

Both the parabolic trough and the power tower models use the same thermal energy storage model. The thermal energy storage system (TES) uses both mass and energy balance equations to calculate the amount of energy stored in the system. The mass balance in the hot and cold tank considers the initial mass in the tank (m_0) and the mass flow rate in (\dot{m}_{in}) and out (\dot{m}_{out}) of the tank. The equations only consider the mass of the molten salt and assume that the temperature of the salt is evenly distributed throughout the tank.

$$m_{\text{stored}} = m_0 + \int_{t_0}^{t_n} (\dot{m}_{in} - \dot{m}_{out}) dt \quad (5.50)$$

The energy balance uses the conservation of energy principle as a basis.

$$Q_{stored} = Q_0 + \int_{t_0}^{t_n} (\dot{Q}_{in} - \dot{Q}_{out} - \dot{Q}_{loss}) dt \quad (5.51)$$

The incoming thermal power is calculated using the incoming fluid temperature and the enthalpy equation ($h(T_{in})$) together with the incoming mass flow rate (\dot{m}_{in}).

The incoming mass flow rate of the hot tank is determined by the solar field HTF pump in the parabolic trough model or the receiver HTF pump in the power tower model. The incoming temperature is the temperature from the solar field / receiver.

$$\dot{Q}_{in,HT} = h(T_{in,HT}) \dot{m}_{in,HT} \quad (5.52)$$

The outgoing thermal power for the hot tank is calculated using the hot tank temperature and the mass flow rate of HTF to the power cycle.

$$\dot{Q}_{out,HT} = h(T_{HT}) \dot{m}_{HTF,PB} \quad (5.53)$$

The incoming thermal power to the cold tank is determined by both the thermal power returning from the solar field / receiver and the power cycle.

$$\dot{Q}_{in,CT} = h(T_{in,field/rec}) \dot{m}_{in,field/rec} + h(T_{in,PB}) \dot{m}_{HTF,PB} \quad (5.54)$$

The outgoing thermal power for the cold tank is calculated using the cold tank temperature and the HTF mass flow rate to the solar field / receiver.

$$\dot{Q}_{out,HT} = h(T_{CT}) \dot{m}_{out,field/rec} \quad (5.55)$$

The initial energy in the tank is determined using the initial mass and temperature of the HTF in the tank. \dot{Q}_{loss} is calculated using the principal of 1°C per 24 hours as discussed in Section 2.1.2.

$$Q_0 = m_{initial} h(T_{initial}) \quad (5.56)$$

The temperature of the storage is updated using an internal energy calculation. The fluid is assumed to be well mixed with even temperature distribution in the tank. The calculation uses an inverse of the enthalpy equation ($h = f(T)$) to calculate the temperature ($T = f^{-1}(h)$). The enthalpy of the molten salt in the tank is calculated as the quotient of the energy stored and the total mass in the tank.

$$T_{tank} = h^{-1} \left(\frac{Q_{stored}}{m_{stored}} \right) \quad (5.57)$$

The tank temperatures and storage masses are updated at every time step. Inputs and outputs for the hot and cold tank model are shown in Figure 25 and Figure 26.

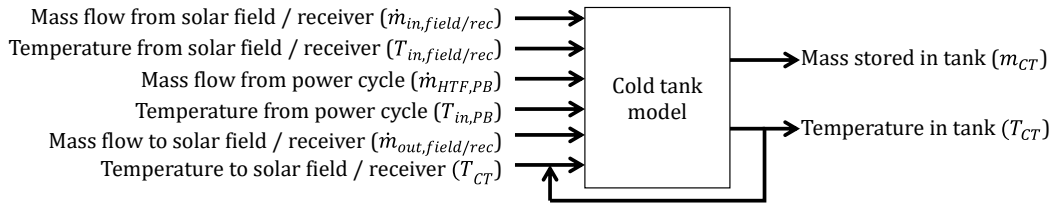


Figure 25: Cold tank model inputs and outputs

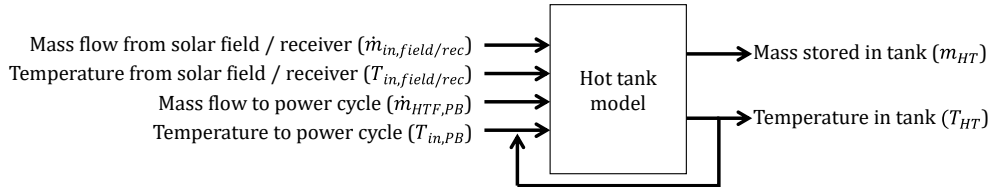


Figure 26: Hot tank model inputs and outputs

5.5. Power cycle model

Thermal energy is sent to the power cycle from the hot storage tank in the form of hot HTF that is pumped through the steam generation system illustrated in Figure 10. The model uses the power cycle control system to calculate the required HTF mass flow based on the temperature of the salt in the hot tank and the required thermal power to the power cycle. The thermal power into the power cycle is determined from the mass flow rate ($\dot{m}_{HTF,PC}$) and the enthalpy derived from the fluid temperature ($h(T_{HT})$) from the hot tank.

$$P_{th,HTF\ in} = h(T_{HT}) \dot{m}_{HTF,PB} \quad (5.58)$$

The thermal to electric efficiency is determined by the input thermal energy from the hot tank. This efficiency is then modified according to the ambient temperature and the temperature of the HTF:

$$P_{e,gross} = P_{th,HTF\ in} \eta_{th} \kappa_{T,amb} \kappa_{T,HTF} \quad (5.59)$$

The thermal to electric efficiency and efficiency modifiers are adapted from performance data provided from De Meyer *et al.* (2015). The thermal to electric efficiency is scaled according to the HTF mass flow rate from the hot tank. The design point mass flow rate of 575 kg/s results in the highest thermal to electric efficiency (Figure 27). If the power cycle is operated in a part-load condition, the HTF flow rate is adjusted.

The HTF mass flow rate to the steam cycle is reduced during power cycle start up for 30 minutes. Figure 27 shows that this is represented by a $\sim 1.5\%$ reduction in efficiency of the power cycle.

If the ambient temperature is less than the design point ambient temperature of $30\text{ }^{\circ}\text{C}$, then the power cycle efficiency increases due to a lower outlet temperature of the Rankine cycle (Figure 28). The air cooled condenser (ACC) is designed with an initial temperature difference (ITD) of $20\text{ }^{\circ}\text{C}$. The ITD is the difference between the steam condensate temperature and the dry bulb temperature of the air. The efficiency of the steam cycle cannot improve in ambient conditions lower than $20\text{ }^{\circ}\text{C}$ due to the limiting back pressure of the turbine generated by the ACC.

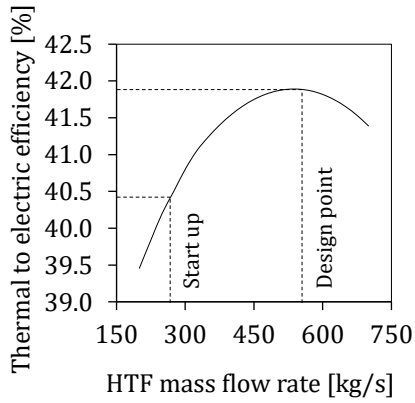


Figure 27: Power cycle thermal to electrical efficiency

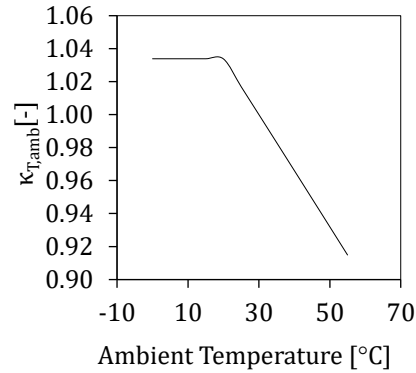


Figure 28: Power cycle ambient temperature modifier

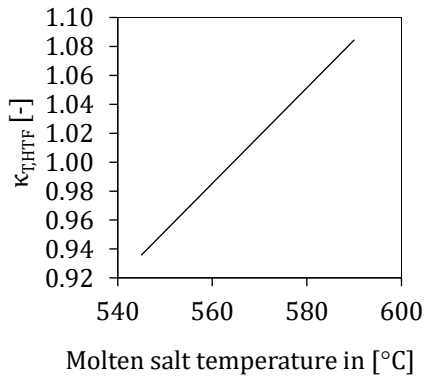


Figure 29: Power cycle molten salt temperature modifier

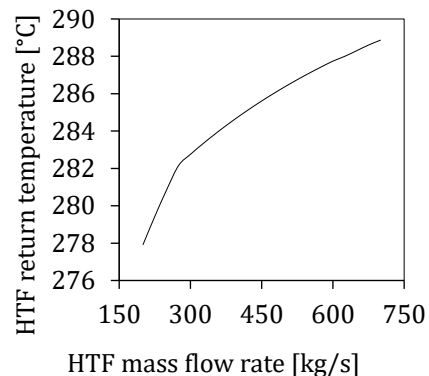


Figure 30: HTF return temperature from the steam generator system

The thermal to electric efficiency is further modified according to the inlet temperature of the HTF (Figure 29), as a lower hot salt temperature also results in lower steam cycle efficiencies.

The return HTF temperature is primarily dependent on the HTF flow rate (Figure 30). A lower flow rate results in increased heat transfer between the HTF and the steam, which leads to a lower outlet temperature. The HTF is returned from the steam generator to the cold tank.

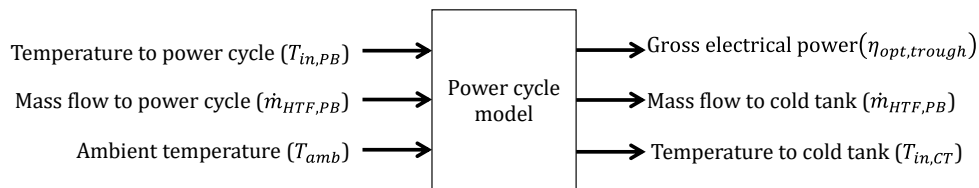


Figure 31: Power cycle model inputs and outputs

5.6. Plant control and operating strategy

The control system of the plant is implemented using MATLAB® Stateflow. Stateflow is a logic tool that allows for the modelling of reactive systems. Predefined states represent real modes of operation of a CSP plant. The operating mode is changed once set-points have been reached or a certain period of time has passed.

The state-based control method is described in Appendix B for the main control areas: the parabolic trough solar field, the power tower receiver and heliostat field and the power cycle.

The parabolic trough solar field and power tower receiver control systems operate according to the level of DNI available and the time of day. The control systems attempt to maintain an HTF outlet temperature of 565 °C to be pumped into the hot tank. The control system also monitors the defocusing of heliostats / solar collectors in the case of the hot storage tank filling up during times of high solar irradiance.

The parabolic trough and the power tower models share the same power cycle control. The power cycle control operates independently of the solar field, and its strategy varies according to the tariff structure that is implemented. Under a flat tariff, the power cycle is only dependent on the energy available in the hot tank. Under the two-tiered tariff the power cycle is also controlled by the time of day tariff that is being implemented. The plant control and operating strategy is documented in detail in Appendix B.

5.7. Parasitic consumption

A CSP plant can suffer substantial parasitic losses. The model considers the following major parasitic losses: solar field HTF pumps for the parabolic trough model / receiver HTF pumps for the power tower model, power cycle HTF pumps, fan drives for the ACC, feed water pumps for the steam cycle, trace heating for piping and a fixed auxiliary load to run the balance of the plant.

5.7.1. Solar field and receiver molten salt pumps

The solar field / receiver molten salt pumps are typically the largest parasitic consumers in molten salt CSP plants. For this reason, a fairly detailed pressure drop calculation is performed for both the parabolic trough solar field and the power tower receiver. Detailed pressure drop calculations for both the parabolic trough solar field and power tower receiver are described in Appendix C.

The pressure drop in the parabolic trough solar field is calculated using the design field layout shown in Figure 59. The major piping components are the runners, header and receiver tubes (Figure 32).

The power tower pressure drop is calculated for the external cylindrical receiver described by de Meyer et.al (2015). The major losses in the power tower molten salt loop are in the tower piping (riser and downcomer) and the receiver tubes themselves.

The pressure drop in the solar field is calculated at each time step in the model using lookup tables. The lookup tables are generated using the pressure drop calculation in Appendix C. The electrical energy used to pump the fluid is calculated using the pumping efficiency ($\eta_p = 0.85$).

$$P_{e,pump} = \frac{\Delta P}{\eta_p} \frac{\dot{m}_{SF}}{\rho_{HTF}} \quad (5.60)$$

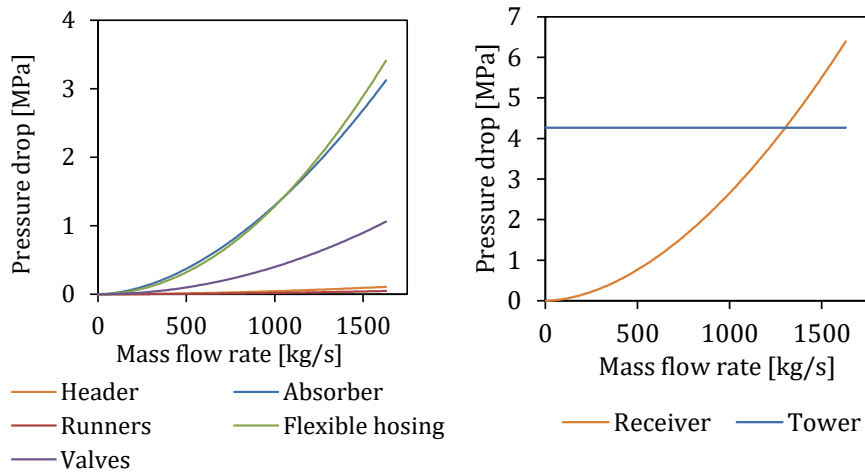


Figure 32: Pressure drop over a parabolic trough solar field with a solar multiple of 2 (left) and a power tower receiver with tower piping with a solar multiple of 2.4 (right).

5.7.2. Balance of plant parasitics

The remainder of the plant parasitics are calculated using coefficients and assumptions largely developed by Wagner & Gilman (2011) and Wagner (2008) for the System Advisory Model.

The electrical energy used on the molten salt pump to the power block is calculated using a coefficient ($\kappa_{\text{cycle pump}} = 1.15 \text{ kJ/kg}$) and the mass flow rate ($\dot{m}_{\text{HTF,PC}}$).

$$P_{e,\text{cycle pump}} = \dot{m}_{\text{HTF,PC}} \kappa_{\text{cycle pump}} \quad (5.61)$$

The parasitic consumption of the ACC fans and feed water pumps is also related to the mass flow to the power block ($\kappa_{\text{ACC}} = 4.4 \text{ kJ/kg}$) as this is a good indication of the level of operation of the power cycle as a whole.

$$P_{e,\text{ACC}} = \dot{m}_{\text{HTF,PC}} \kappa_{\text{ACC}} \quad (5.62)$$

Trace heating and thermal losses for the header piping and components in the parabolic trough model and the riser and downcomer in the receiver model are treated using a thermal loss coefficient of 10 200 W/m . This is equated to an electrical parasitic loss using the power cycle thermal to electric efficiency at the time step.

A fixed parasitic load of 0.55 MW_e is implemented for smaller parasitics that are not covered by the major parasitic calculations. These may include powering the operating room, lighting and other miscellaneous equipment.

5.8. System Advisor Model comparison

In this section the parabolic trough model is compared to the System Advisor Model (SAM) physical trough model. The power tower model is compared to the SAM molten salt power tower model.

5.8.1. Parabolic trough model comparison

The SAM physical trough model has been validated against the performance of Andasol I (NREL, 2012a). In order to compare the performance of the molten salt parabolic trough model to SAM, the same parabolic trough plant was designed using both the model and SAM. The main input parameters for the site comparison are shown in Table 21. Both models were run using a single year of data (2015) from the SAURAN station at the University of the Free State in South Africa.

Table 21: Plant description for power tower model validation

| Parameter | Value | Unit |
|---------------------------|--------------|-------------------|
| Location | Bloemfontein | - |
| Design point DNI | 1040 | W/ m ² |
| Solar field size | 720 000 | m ² |
| Number of loops | 105 | - |
| Gross generating capacity | 100 | MW _e |
| Hours of storage | 14 | hours |

The HTF and the storage medium were both set to solar salt in SAM in an attempt to simulate a plant with direct molten salt storage. Schott PTR70 (2008) receiver tubes were used in both the models, as the HCEMS-11 receiver tubes used in the original plant design are not available in the SAM database. The major difference between SAM and the parabolic trough model is that SAM can only be set to use electrical trace heating for freeze protection while the model uses energy stored in the cold tank for freeze protection.

Hourly meteorological data (Figure 33(a)) was used as input because the maximum resolution of SAM is 1 hour. Figure 33 illustrates the modeled operation of the plant over five days in summer in Bloemfontein, South Africa.

Figure 33(b) shows the gross electrical power and the hot tank fill level using both of the models. During the four clear days of operation the two models are shown to perform almost identically. The day with low levels of DNI results in low hot tank fill levels for both models. SAM is shown to intelligently lower the power cycle production level to maintain operation while the parabolic trough model continues operation at design point.

During the clear days in Figure 33(b), both the model and SAM show the same rate of charging of the hot tank. This indicates that both models are receiving the same thermal energy output from the solar field. The partly cloudy day in Figure 33(b) shows that the model charges the hot tank notably more than SAM. This indicates that the thermal energy output from the solar field during periods of low or transient DNI is higher than that of SAM.

During discharge, the model's discharge rate is lower than that of SAM – this indicates that the power cycle efficiency is slightly higher than that of SAM. This is further evident in the longer power cycle operation period of the model compared to SAM.

Figure 33(c) compares the field inlet and return temperatures for both models. The four good days show high correlation between SAM and the model with regards to

the return temperature. The field inlet represents the temperature of the cold tank. The cold tank temperature of the model is notably higher than SAM due to the thermal freeze protection implemented, as described in Appendix B. SAM uses electrical trace heating in the field for freeze protection rather than using energy in the cold tank.

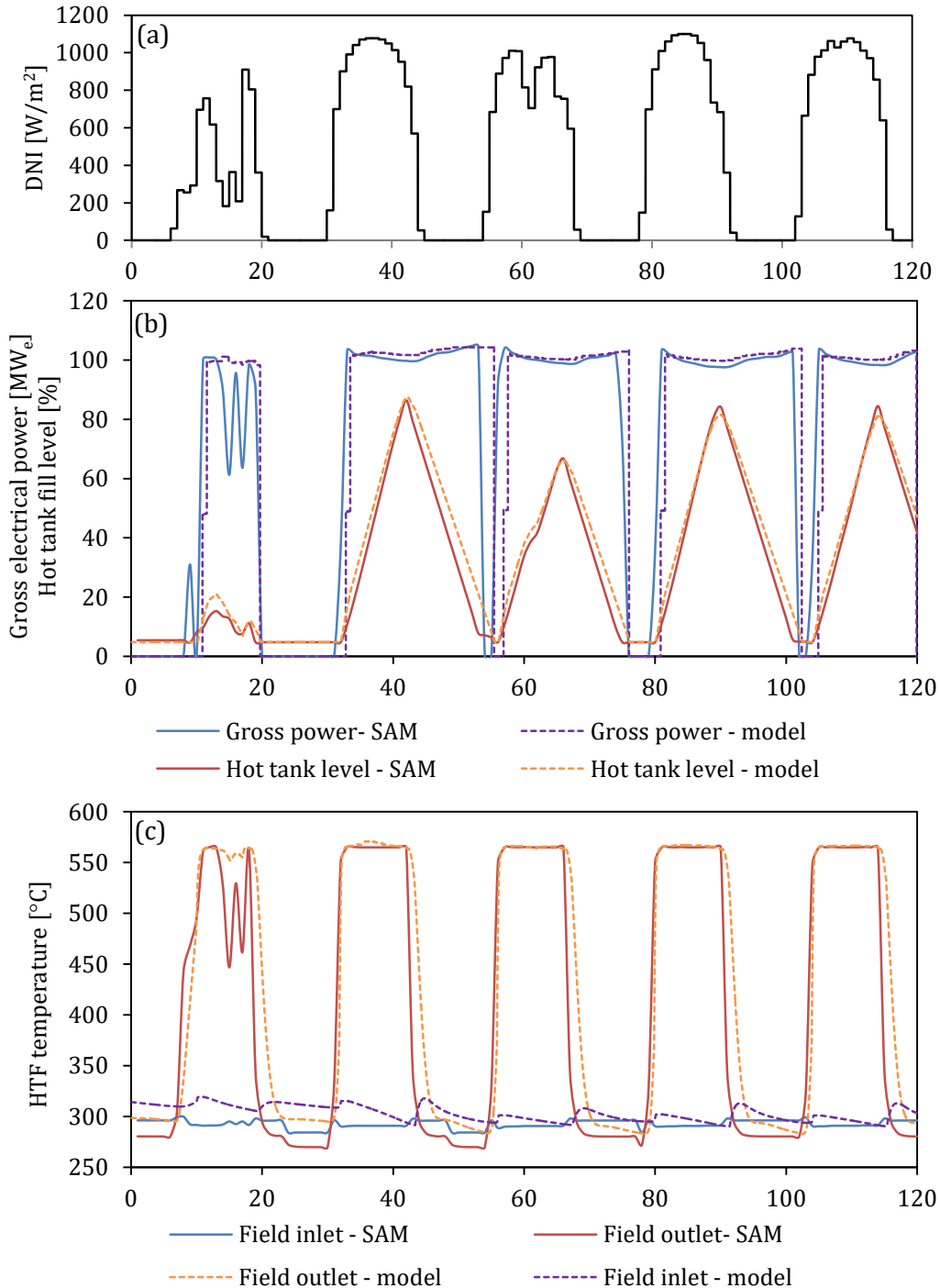


Figure 33: Plant operation comparison using SAM physical parabolic trough model vs. the designed molten salt parabolic trough model

The monthly net electrical yield is compared for the SAM and the model in Figure 34. The model is shown to overestimate the net electrical yield in all but two of the months. The annual yield of the model was 258.9 GWh_e compared to 246.0 GWh_e for SAM, this equates to a 5.0 % lower annual yield calculation using SAM.

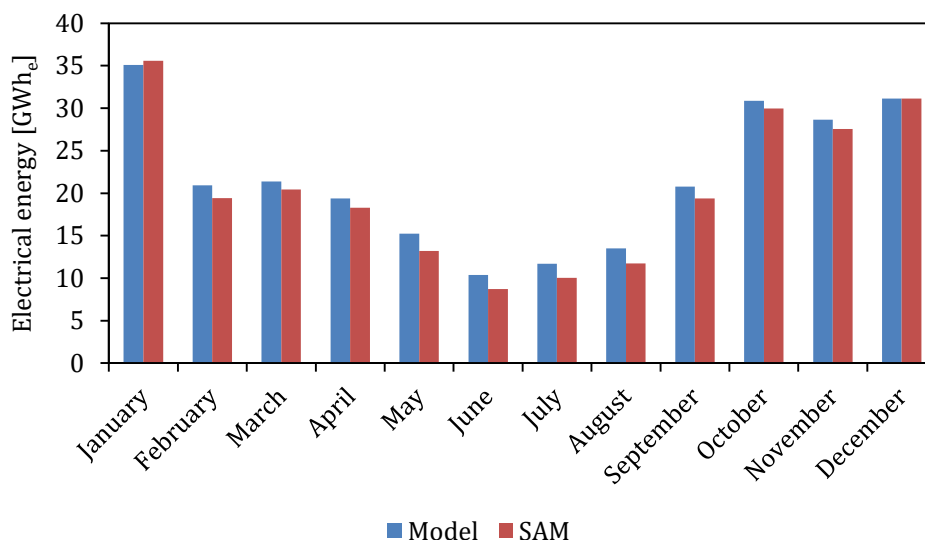


Figure 34: Monthly net electrical yield comparison between SAM and the parabolic trough model

5.8.2. Power tower model comparison

The SAM molten salt power tower model has been validated against the performance of Gemasolar (NREL, 2012b). In order to compare the performance of the molten salt power model with SAM, the same power tower plant was designed using both the model and SAM. The main input parameters for the site comparison are shown in Table 22. Once again, both models were run using a single year of data (2015) from the SAURAN station at the University of the Free State.

Table 22: Plant description for power tower model validation

| Parameter | Value | Unit |
|---------------------------|--------------|-------------------|
| Location | Bloemfontein | - |
| Design point DNI | 1020 | W/ m ² |
| Solar field size | 820 000 | m ² |
| Receiver size | 485 | MW _{th} |
| Gross generating capacity | 100 | MW _e |
| Hours of storage | 14 | hours |

Figure 35 compares the operation of SAM and the model over three days in March in Bloemfontein, South Africa. Figure 35(b) compares the gross electrical power and the hot tank fill level of the two models. The model is shown to predict slightly higher fill levels and duration of power generation compared to SAM. The increased rate of hot tank charging from the model indicates that there is more thermal energy delivered from the receiver in the model than in SAM.

In Figure 35(c) the receiver inlet and outlet temperatures are also compared for the two models. The temperatures show excellent correlation on days with consistent DNI values. The return temperatures vary on days with irregular irradiation due to differences in the receiver operation set points used in SAM and the model.

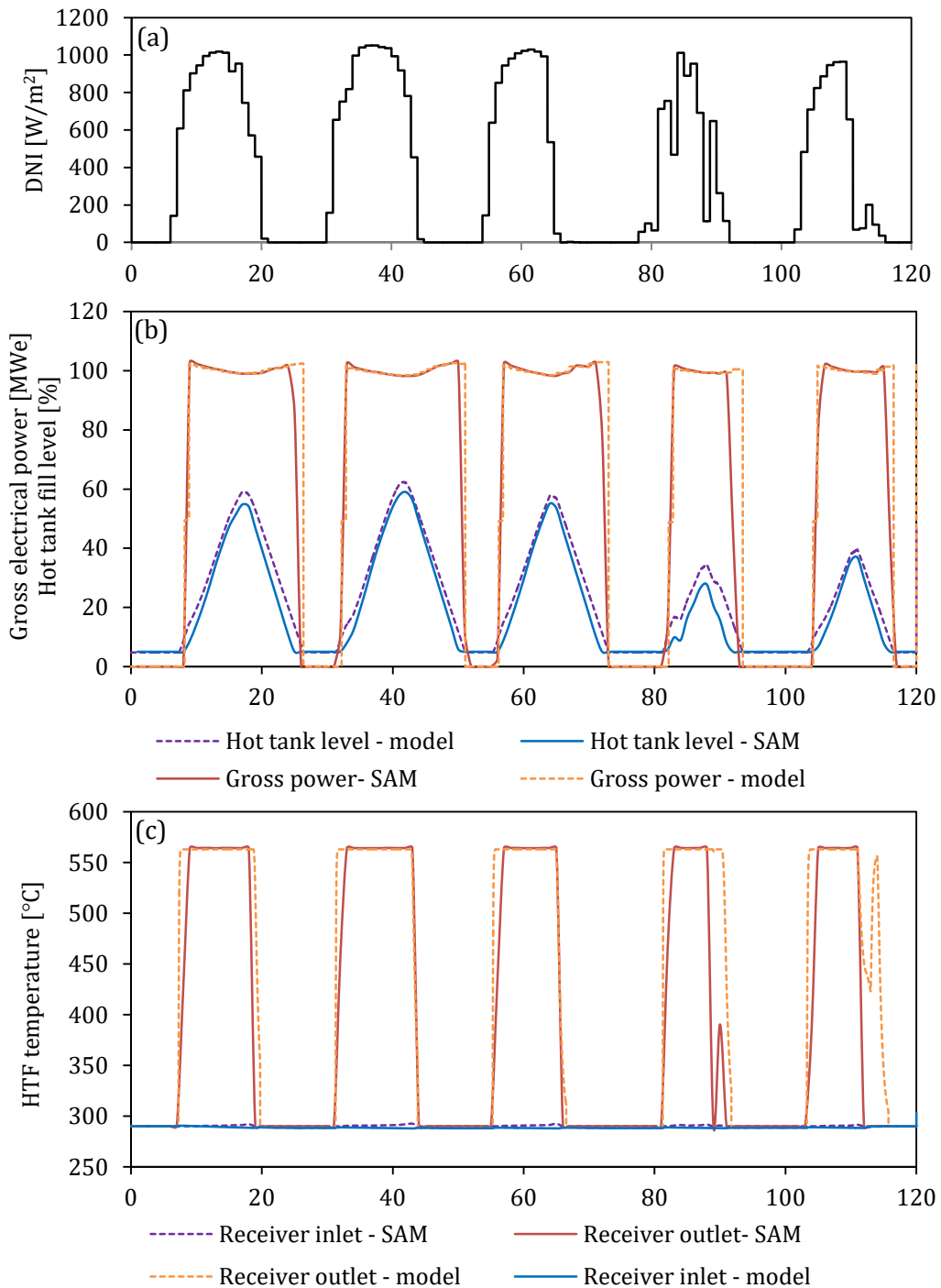


Figure 35: Plant operation comparison between the molten salt power tower model and SAM

The monthly net electrical yield predicted by the two models is illustrated in Figure 36. The model is shown to over predict electrical yield during the summer months and under predict yields during winter months. This is a result of the simplified heliostat field efficiency model used. The annual yield using the model is 301.0 GWh_e compared to 289.4 GWh_e using SAM, which equates to a 4.0 % difference.

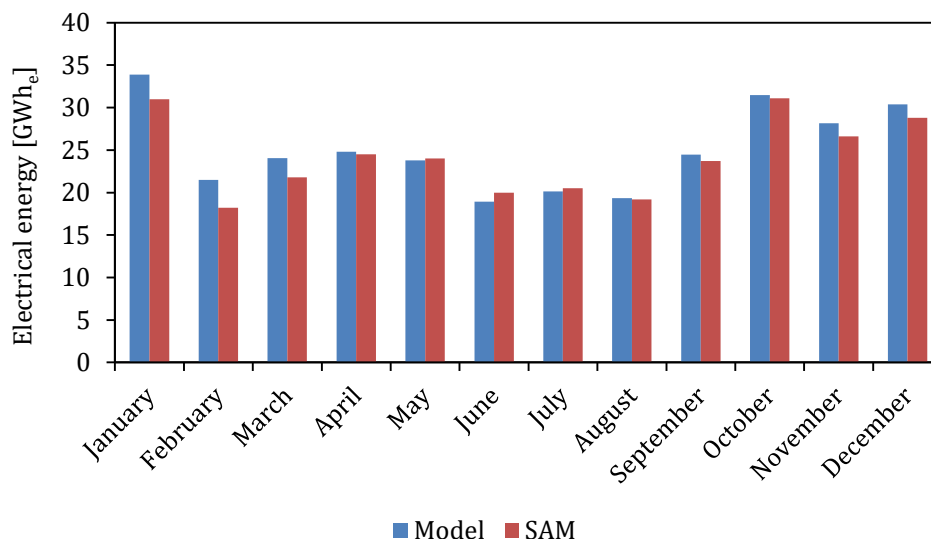


Figure 36: Monthly net electrical yield comparison between the molten salt power tower model and SAM

The parabolic trough and power tower models show that the power cycle operates more efficiently than SAM. SAM contains a very detailed steam cycle model that includes consideration for part-load operation and considers losses over the molten salt to steam heat exchangers that have not been considered in the simplified power cycle model used in this study.

Both the parabolic trough and the power tower models show a larger thermal energy yield from the solar field during periods of low or transient DNI. This suggests that the transient behaviour of the collector field and receiver may need further refinement.

This is by no means an extensive validation of either the parabolic trough or power tower models. The comparison with SAM is intended to demonstrate that both models are operating in a similar manner to the way in which actual plants operate. The power cycle control and fluid temperature calculations have shown to be within an acceptable limit of the validated model.

5.9. Financial model

A simple financial analysis was used to evaluate the performance of the parabolic trough and power tower technologies. The most commonly used indicator is the LCOE. The LCOE represents the equivalent cost of producing 1 kWh_e of electricity over the lifetime of the plant. Equation 5.63 is used to calculate the LCOE for a plant. The model for each of the technologies is used to calculate the net electrical energy produced over the year ($E_{e,a}$).

$$LCOE = \frac{CRF \times CAPEX_{total} + OPEX_{fixed}}{E_{e,a}} + OPEX_{variable} \quad (5.63)$$

The LCOE equation considers the capital expense of constructing the plant (*CAPEX*) as well as the annual operating expenses (*OPEX*). The *CAPEX* can be calculated by summing up the individual component costs of the plant. The individual capital cost components for parabolic trough plants and power tower plants are listed in Table 23 and Table 24 respectively. The operating expenses for both plants are listed in Table 25.

The capital return factor is calculated using Equation 5.64. The CRF is determined using the discount rate (k_d) and the project lifetime (n).

$$CRF = \frac{k_d(1 + k_d)^n}{(1 + k_d)^n - 1} \quad (5.64)$$

Both the parabolic trough and power tower cost models assume a discount rate of 8 % and a project lifetime of 25 years.

Table 23: Capital expenses for a molten salt parabolic trough plant

| Capital expense component | Cost | Unit |
|----------------------------|-------|------------------------------------|
| Purchasing of land | 0.2 | USD/m ² _{land} |
| Site improvements | 30.0 | USD/m ² |
| Collector field | 178.0 | USD/m ² |
| Heat transfer fluid system | 70.0 | USD/m ² |
| Thermal energy storage | 25.0 | USD/kWh _{th} |
| Steam turbine system | 800.0 | USD/kW _e |
| Steam generating system | 250.0 | USD/kW _e |

The cost categories for parabolic trough plants are detailed in Section 2.1.3. The cost of purchasing land is based on advertised farm costs in the Upington area. Site improvement, collector field and heat transfer fluid system costs are based on the 2015 cost estimates of Kurup and Turchi (2015). The cost of the collector field is set as 178 USD/m², which is calculated for Ultimate Trough collectors using molten salt receiver tubes rather than the 170 USD/m², which uses thermal oil receiver tubes.

The thermal energy storage, steam turbine system and steam generating system costs are selected using cost calculations by Kolb *et al.* (2011) for power tower plants. The thermal energy storage and power cycle component costs are set using power tower estimates because the molten salt parabolic trough plant uses the same HTF with the same operating temperatures as the power tower plants in the study.

Table 24: Capital expenses for a molten salt power tower plant

| Capital expense component | Cost | Unit |
|---------------------------|-------|------------------------------------|
| Purchasing of land | 0.2 | USD/m ² _{land} |
| Site improvements | 16.0 | USD/m ² |
| Heliostat field | 170.0 | USD/m ² |
| Receiver and tower | 173.0 | USD/kW _{th} |
| Thermal energy storage | 25.0 | USD/kWh _{th} |
| Steam turbine system | 800.0 | USD/kW _e |
| Steam generating system | 250.0 | USD/kW _e |

The power tower plant cost model uses the same thermal energy storage, steam turbine system, steam generating system and land costs as the parabolic trough cost model. The cost of site improvements lower compared to parabolic troughs plants because trough plants require precise earthworks, which ensure that the field is perfectly sloped to allow for the draining of the parabolic trough loops. The use of individual heliostats in the field results in lower levels of accuracy in site preparation, and thus lower costs for power tower plants. The heliostat field and receiver costs are selected from the figures calculated by Turchi *et al.* (2013), which were indexed for 2015 by Kurup & Turchi (2015).

The operating expenses for both the parabolic trough and power tower plants are assumed to be identical. The cost figures calculated by Kurup and Turchi (2015) discussed in the literature review are selected (Table 25). Fixed operating costs depend on the size of the plant and they represent the payment of onsite staff and consumables. Variable operating costs depend on the amount of electricity produced and they represent the expense of maintenance and repair of equipment as well as maintenance-related consumables.

Both models also include an indirect capital expense component that takes into account EPC, project management and owners costs – as detailed in Section 2.1.3. The indirect capital expense is calculated as 30 % of total capital cost.

Table 25: Operating expenses for a molten salt parabolic trough and power tower plants

| Operating expense component | Cost | Unit |
|-----------------------------|------|----------------------|
| Fixed operating cost | 66 | USD/ kW _e |
| Variable operating cost | 3 | USD/MWh _e |

LCOE is typically used to indicate the performance of a power generation system, however, using LCOE as a performance indicator is only valid when using a flat tariff system. This is due to the fact that there is no distinction between the time of day tariff in place when electrical energy is generated. Silinga *et al.* (2014) make use of an indicator called the levelized profit of energy (LPOE). The LPOE is used to determine the implications of the two-tier tariff structure on the proposed CSP system by establishing the most profitable configuration. LPOE is the difference between the income and the cost of generating 1 kWh_e of electricity. The income generated is calculated as the sum of the electrical energy generated (E_e) and the tariff being implemented (tar) at each time step of the simulation (t).

$$LPOE = \frac{\sum_{t=1}^n (E_{e,t} tar_t)}{E_{e,a}} - LCOE \quad (5.65)$$

The REIPPPP tariffs that were used for the two-tiered model are from Round 3.5 and are listed in Table 26. An exchange rate of 13:1 ZAR:USD was used for the LPOE calculations.

Table 26: Two-tiered feed-in tariff structure

| Name | Hours | Tariff [%] | Tariff [ZAR/kWh _e] | Tariff (<i>tar</i>) [USD/kWh _e] |
|----------|---------------|------------|--------------------------------|---|
| Standard | 05:00 – 16:30 | 100 | 1.62 | 0.1246 |
| | 21:30 – 22:00 | | | |
| Peak | 16:30 – 21:30 | 270 | 4.37 | 0.3365 |
| Night | 22:00 – 05:00 | 0 | 0 | 0 |

5.10. Conclusion

The power tower and parabolic trough models have been constructed and documented in depth. Both models have shown acceptable levels of agreement with SAM. Going forward, these models will provide the basis of the comparison between the two technologies and allow for plant simulation using a variety of meteorological data.

6. Site selection and meteorological data

The methodology for selecting six potential sites in South Africa for a CSP plant is described in this section. A method for generating high resolution DNI is implemented at each of the sites. This method is described and evaluated in Appendix A, an Appendix which should be used as a technical reference to this section. Finally meteorological files are compiled at each of the locations to be used in the simulation models discussed in Section 5.

6.1. Selecting sites in South Africa

The IRENA site selection tool and renewable energy map (Figure 37) was used to identify six sites for further evaluation. The tool uses multi-criteria (MC) scoring, which considers levelized cost of electricity (LCOE) along with other criteria that improve site suitability such as distance from transmission lines and roads, slope, population density, land use, and capacity factor.

Use of the site selection tool requires the user to weight the importance of various factors, which indicate site suitability. For this investigation LCOE was given the highest weighting of 60 %, distance to load centers was weighted with 20 % importance; while land use, population density, human footprint and slope were each given a weighting of 5 %. Figure 37 illustrates the CSP development zones for CSP and the electrical transmission lines.

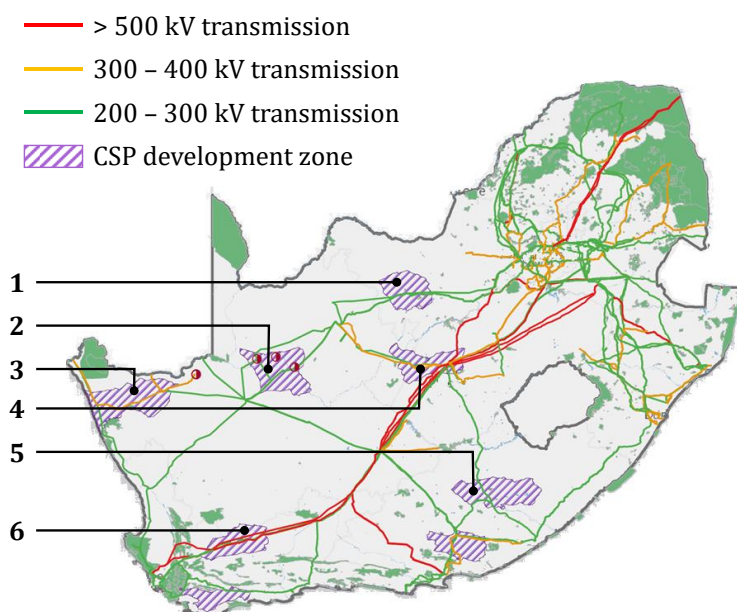


Figure 37: International Renewable Energy Agency zones for concentrating solar power development (Wu *et al.*, 2015a)

Using the IRENA tool, the top rated sites were found to be in the Northern Cape area due to the high levels of solar radiation. The issue with CSP development in the Northern Cape, however, is that there is very limited electrical transmission capacity

available. The Northern Cape consists of two main transmission areas. The transmission capacity is currently 470 MW_e for the north-western area and 880 MW_e for the eastern area of the province (Eskom, 2015). For this reason, it is unlikely that large amounts of CSP development will be available in the Northern Cape beyond the round 4.5 selected projects, especially considering that it will be competing with PV for transmission access.

Instead of simply selecting the six sites with the highest MC scores, the top rated site was selected from each of the CSP zones numbered 1 to 6 in Figure 37. Distributing the generating capacity of CSP to alternative provinces is intended to ease the load on the transmission grid and the water supply of a particular region. Details of the selected sites are listed in Table 27. The six selected sites are plotted on a map indicating annual DNI resource in Figure 38

Table 27: IRENA site information

| Closest city / town name | Province | IRENA Zone ID | Latitude | Longitude |
|--------------------------|---------------|---------------|---------------|---------------|
| Springbok | Northern Cape | BC | 29°27'02.07"S | 18°49'11.13"E |
| Upington | Northern Cape | BJ | 29°18'22.44"S | 22°06'43.10"E |
| Kimberley | Free State | D | 28°40'45.04"S | 24°53'29.43"E |
| Laingsburg | Western Cape | AB | 32°56'51.27"S | 19°55'49.55"E |
| Vryburg | North West | U | 27°05'18.78"S | 24°18'41.28"E |
| Molteno | Eastern Cape | AL | 31°24'37.13"S | 26°19'39.58"E |

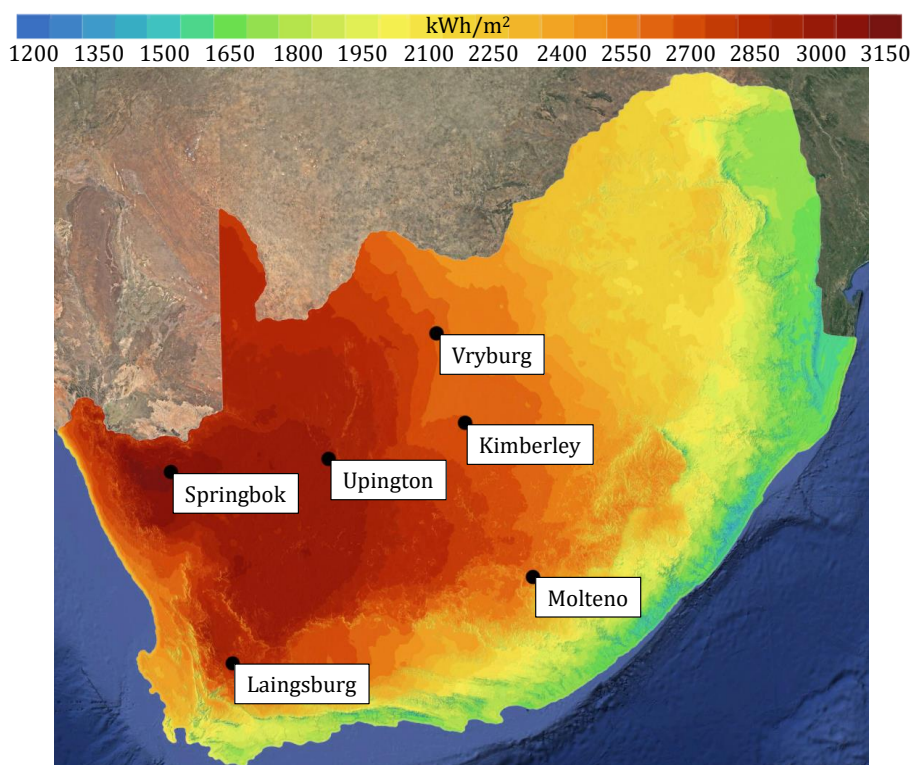


Figure 38: Proposed sites for a 100 MW_e CSP plant showing the annual average direct normal irradiation (GeoModel Solar, 2014; Google Inc., 2015)

The first two selected sites are from the Northern Cape Province. The Springbok site is close to the area with the highest level of available DNI in the country. The Upington site is 300 km to the east of this. While these two sites are expected to yield the highest levels of electricity due to the high DNI levels, it must be considered that the transmission grid availability in the area is limited, as well as access to surface water. All of the operating CSP plants in South Africa are situated in the Northern Cape between Upington and Springbok.

The Kimberley site is situated 20 km outside of the town of Kimberley in the Free State Province. While there are lower levels of DNI in this area than the Northern Cape, it is well situated near the load centers of Kimberley and the major city of Bloemfontein. The site is in close proximity to surface water, transmission lines and a 300 kV substation.

Moving to the North West Province, the Vryburg site was selected as it one of the areas in the province with the highest annual DNI values. The site is within 50 km from a 300 kV substation, however, once again water access is limited.

In the Eastern Cape, the Molteno site was selected. This is the site with the lowest solar resource; however it has adequate water availability. While the site is located on a transmission line, the nearest substation is 100 km away.

The final site selected is Laingsburg in the Western Cape Province. This site is ideally situated in the Karoo, where there are high levels of DNI coupled with grid availability and water access possibilities.

6.2. Compilation of site meteorological data

Typical meteorological year datasets for the six sites was not available for the selected sites, however, the following data was available at the time of the research:

- Satellite derived DNI information from European Community Solar Data (SoDa) datasets (Stoffel *et al.*, 2010) was available for all six of the sites with an hourly resolution (2005-2014).
- Ground measured, 1 minute resolution DNI data is available from the South African Universities Radiation Network (SAURAN) (Brooks *et al.*, 2015) (1 year). The individual measurement stations utilized for the study were as follows: Richtersveld station, University of Free State (UFS) station and Eskom's Sutherland station (2013-2015).
- Historical wind and temperature data from weather stations near to the sites, courtesy of the South African Weather Service (South African Weather Service, 2015) (2005-2014). The measurement stations used are listed in Table 28.

In order to generate a DNI dataset representative of each of the locations typical meteorological conditions, a script was written in order to compile a single year of hourly DNI, wind and temperature information. The script uses DNI data and finds the individual month, which is closest to the average month from the 10 year dataset. Each average month is then compiled to form a representative solar year. The dry-bulb temperature or wind speed for the selected month is then used.

The hourly DNI for each site was used in combination with the closest SAURAN station to generate synthetic DNI for each site using the method described and evaluated in Appendix A.

Each site meteorological file is then compiled using minute resolution DNI data, hour resolution temperature data and hour resolution wind data. Table 28 shows a summary of the compiled meteorological input files. The annual DNI, average wind speed and average dry-bulb temperature are shown for each of the proposed sites is listed in Table 29.

Table 28: Meteorological data sources for the six selected sites

| Site name | Hourly DNI data (Satellite) | Minutely DNI data (Ground) | SAWS wind and temperature |
|------------|--------------------------------|-------------------------------|------------------------------|
| Springbok | SoDa | Richtersveld | Pofadder |
| Upington | SoDa | Richtersveld | Prieska |
| Laingsburg | SoDa | Sutherland | Laingsburg |
| Kimberley | SoDa | UFS | Kimberley |
| Vryburg | SoDa | UFS | Vryburg |
| Molteno | SoDa | Graaf Reneit | Jamestown |

Table 29: Meteorological information for the six selected sites

| Site name | Annual DNI [kWh/(m ² ·a)] | Average wind speed [m/s] | Average dry-bulb temperature [°C] |
|------------|---|-----------------------------|--------------------------------------|
| Springbok | 2797 | 3.1 | 19.84 |
| Upington | 2581 | 3.0 | 21.01 |
| Laingsburg | 2652 | 2.4 | 18.17 |
| Kimberley | 2481 | 3.8 | 19.34 |
| Vryburg | 2442 | 2.8 | 20.01 |
| Molteno | 2449 | 2.3 | 13.96 |

6.3. Conclusion

In this section the IRENA site selection tool is used to select sites with high potential for CSP development in South Africa. Hourly DNI data is acquired for each of these sites. The IRENA tool is thought to have provided sufficient consideration for limiting factors for CSP in South Africa, such as transmission line access and water availability. This ensures that relevant sites have been selected for the comparison of the two technologies.

A method proposed by Fernandez-Peruchena *et al.* (2015) in combination with high temporal resolution DNI data from SAURAN is used to generate high resolution DNI (Appendix A) at each of the sites. The minute resolution DNI data is combined with temperature and wind information from nearby SAWS stations to compile a full year of representative meteorological data for each site. The meteorological data allows for both the power tower and parabolic trough plants to be simulated at each of the sites. The results of these simulations are documented in the section to follow.

7. Simulation results

This section contains results and analysis of annual simulations that were performed at each of the six sites using the compiled meteorological data (Section 6) and the two plant models (Section 5).

First, the operation of the parabolic trough and power tower plants is compared over three days in winter and summer. This comparison demonstrates the fundamental differences in performance between the two technologies in operation.

The optimum design of a plant varies according to the site conditions and the tariff under which it operates. In an attempt to find the optimum design, a parametric analysis is carried out, where the solar multiple and storage hours were varied for each of the technologies at each of the sites.

Using the optimum plant designs, a simulation was run for both technologies at each of the six sites under a flat tariff and a two-tiered tariff structure in order to model the performance under Round 2 and Round 3.5 of the REIPPPP in South Africa. The effect of technology selection, location and tariff structure on annual plant efficiencies is then discussed.

7.1. Operation of parabolic trough and power tower plants

7.1.1. Operation under a flat tariff structure

In this section the operation of the parabolic trough and power tower plant models are compared over three days in winter and summer at the Vryburg site. Both plants were designed for the same annual electrical yield of 500 GWh_e. Table 30 and Table 31 give the primary design considerations for the power tower and the parabolic trough plant respectively. Both plants have a solar multiple of 2.6 with 14 hours of storage. The design point for both of the plants is at vernal equinox, March 20 at 12:00 solar time. The higher solar to electrical efficiency of the parabolic trough plant at design point results in a smaller solar field size compared to the power tower plant.

The primary efficiencies of the plants are defined as follows:

- Solar field efficiency (η_{SF}) compares the energy focused on the receiver (power tower) / receiver tubes (parabolic trough) to the incident energy on the solar field. This takes into account optical losses.
- Receiver efficiency (η_{rec}) is a comparison between the incident energy on the receiver / receiver tubes and the thermal power delivered to the hot tank. This efficiency takes into account all receiver / solar field thermal losses.
- Power cycle efficiency (η_{PC}) is the thermal to electric efficiency of the steam cycle.

- Auxiliary efficiency (η_{aux}) compares the net electrical energy to the gross electrical energy produced, accounting for the parasitic electrical consumption of plant pumps, drives and other components.
- Net efficiency (η_{net}) compares the annual net electrical energy generated to the annual incident energy on the solar field. This takes into account all of the major losses of the plant.

An additional loss is caused by the dumping of solar energy by defocusing the solar collectors / heliostats when the hot tank is full. This effect is quantified using an annual dumping efficiency (η_{dump}), which compares the thermal energy incident on the receiver to the thermal energy effectively defocused in the solar field.

Table 30: Power tower plant design for flat tariff structure

| Parameter | Value | Unit |
|--|-----------|-------------------|
| Location | Vryburg | - |
| Design point DNI | 947 | W/ m ² |
| Solar multiple | 2.6 | - |
| Solar aperture area | 1 308 000 | m ² |
| Receiver size | 623.5 | MW _{th} |
| Power cycle thermal | 240 | MW _{th} |
| Hours of storage | 14 | hours |
| Salt mass | 31 700 | tons |
| Generating capacity | 100 | MW _e |
| Solar field efficiency ($\eta_{SF,dp}$) | 57.1 | % |
| Receiver efficiency ($\eta_{rec,dp}$) | 88.3 | % |
| Power cycle design point efficiency ($\eta_{PC,dp}$) | 41.7 | % |
| Auxiliary efficiency ($\eta_{aux,dp}$) | 90.0 | % |
| Net efficiency ($\eta_{net,dp}$) | 18.9 | % |

Table 31: Parabolic trough plant design for flat tariff structure

| Parameter | Value | Unit |
|--|-----------|-------------------|
| Location | Vryburg | - |
| Design point DNI | 947 | W/ m ² |
| Solar multiple | 2.6 | - |
| Solar field size | 1 118 000 | m ² |
| Number of loops | 172 | - |
| Power cycle thermal | 240 | MW _{th} |
| Hours of storage | 14 | hours |
| Salt mass | 32.4 | tons |
| Generating capacity | 100 | MW _e |
| Solar field efficiency ($\eta_{SF,dp}$) | 62.2 | % |
| Receiver efficiency ($\eta_{rec,dp}$) | 89.7 | % |
| Power cycle design point efficiency ($\eta_{PC,dp}$) | 41.7 | % |
| Auxiliary efficiency ($\eta_{aux,dp}$) | 90.0 | % |
| Net efficiency ($\eta_{net,dp}$) | 20.9 | % |

Figure 39 and Figure 40 show three days of operation for both parabolic trough and power tower plants. The operation is under a flat feed in tariff at the Vryburg site.

Figure 39(a) shows winter DNI in Vryburg where days are typically clear and the DNI level peaks at 900 W/m^2 , the day length is approximately 10 hours.

Figure 39(b) compares the solar field efficiency of the parabolic trough and power tower plant. It is evident that the trough plant has low midday efficiency. This is caused by a large incident angle, which results in cosine losses in parabolic trough plants.

Figure 39(c) illustrates the net thermal power delivered to the hot tank. The high solar field efficiency of the tower plant in winter results in a large amount of thermal energy being absorbed. It is shown that the net thermal power delivered is negative for the trough plant overnight. This is caused by thermal losses as the hot HTF is circulated around the solar field. The peak thermal loss occurs as soon as there is no solar radiation and the average HTF temperature in the field is high. The overnight thermal losses result in a temperature drop in the HTF, which is explained in the operating strategy in Appendix B.

Figure 39(d) compares the power cycle operation of the two models. The power tower plant has extended power cycle operating hours and higher hot tank fill levels because more thermal power is absorbed during the day compared to the parabolic trough plant. The downward spike in the net power of the parabolic trough plant prior to production is a result of the HTF field pump controller changing mass flow instantaneously. The large amount of inertia in the field results in an increased auxiliary consumption, which decreases the net electrical output of the parabolic trough plant.

Figure 40 illustrates the performance of a parabolic trough and a power tower plant over three summer days at the Vryburg site from December 25th. Figure 40(a) shows that during the summer in Vryburg the DNI peaks at approximately 950 W/m^2 and the day length is 14 hours.

Figure 40(b) illustrates that the solar field efficiency of the parabolic trough plant is shown to be much greater than the power tower plant. When compared to Figure 39(b), this shows the dramatic seasonal change of parabolic trough and the relative consistency of power tower solar field efficiency.

Figure 40(c) shows that in the summer the thermal power delivered by the parabolic trough plant is greater than the power tower plant due to its high levels of summer efficiency. Upon inspection of the first day of Figure 40(c) it is evident that there is a dramatic decrease in thermal power, first for the parabolic trough plant and then for the power tower plant. This is an illustration of the effect of dumping - caused by the defocusing of solar collectors / heliostats when the storage is full.

Figure 40(d) indicates that the net power generated by both technologies continues overnight. The dip in net electrical power during the day is caused by the HTF pumps reaching their maximum during daytime operation, which increases the parasitic load on the plant. The power tower power cycle is shown to stop operation temporarily during the third day of operation while the trough power cycle keeps operating. This is due to the difference in thermal energy delivered to the hot tank, which is a direct result of the lower solar field efficiency of power towers during summer operation.

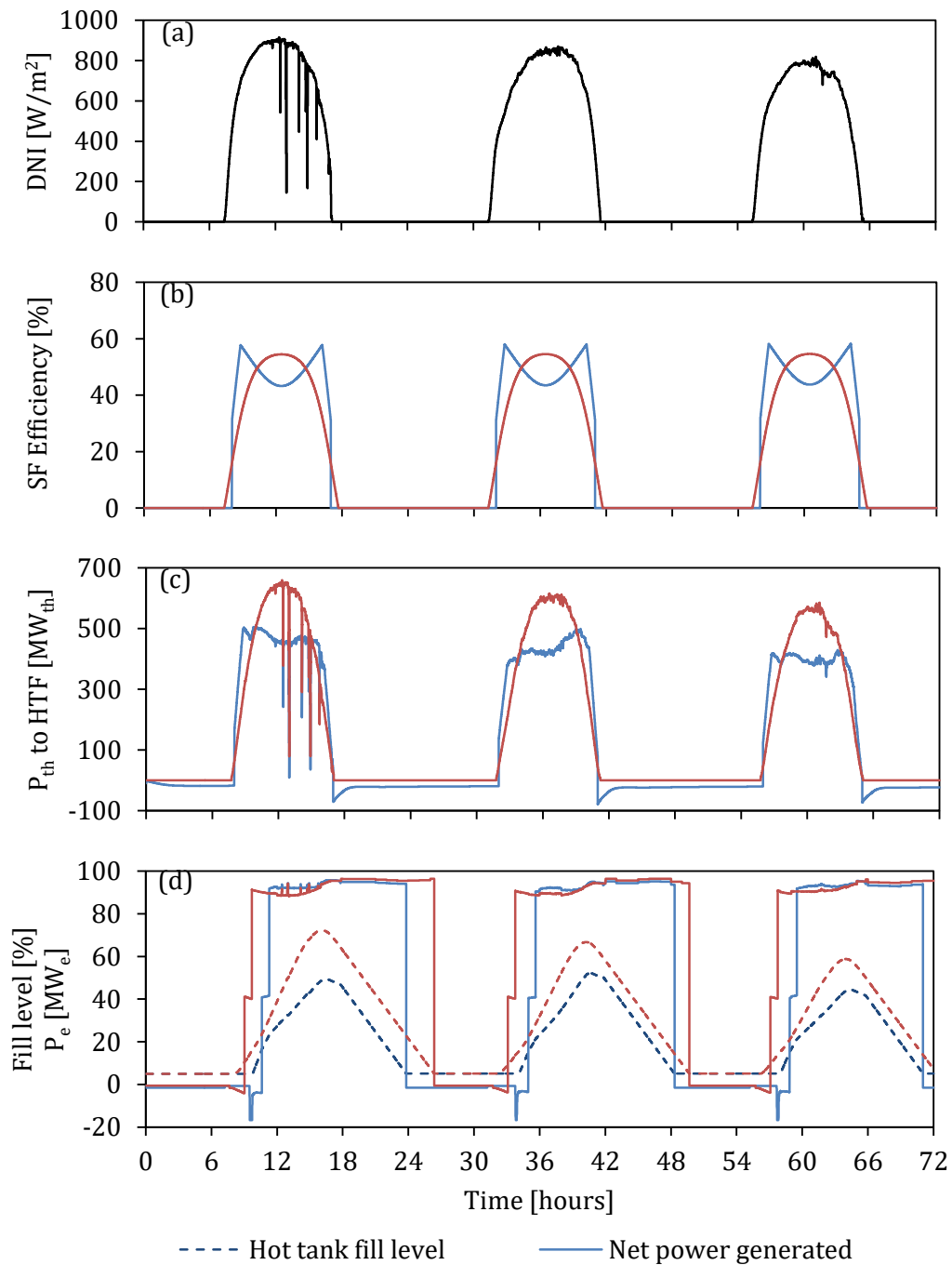


Figure 39: Performance of parabolic trough (blue) and power tower (red) plants over three winter days at the Vryburg site from June 10th

When comparing Figure 39 and Figure 40 it becomes evident that the power tower technology has similar solar field efficiency year round, however, the parabolic trough plants experience seasonal variation. The seasonal variation is problematic when it comes to the sizing of a parabolic trough plant. Both the plants were sized at vernal equinox in an attempt to find a fair average of annual performance – however

the increase in performance of the parabolic trough plant still results in excessive dumping in the summer time.

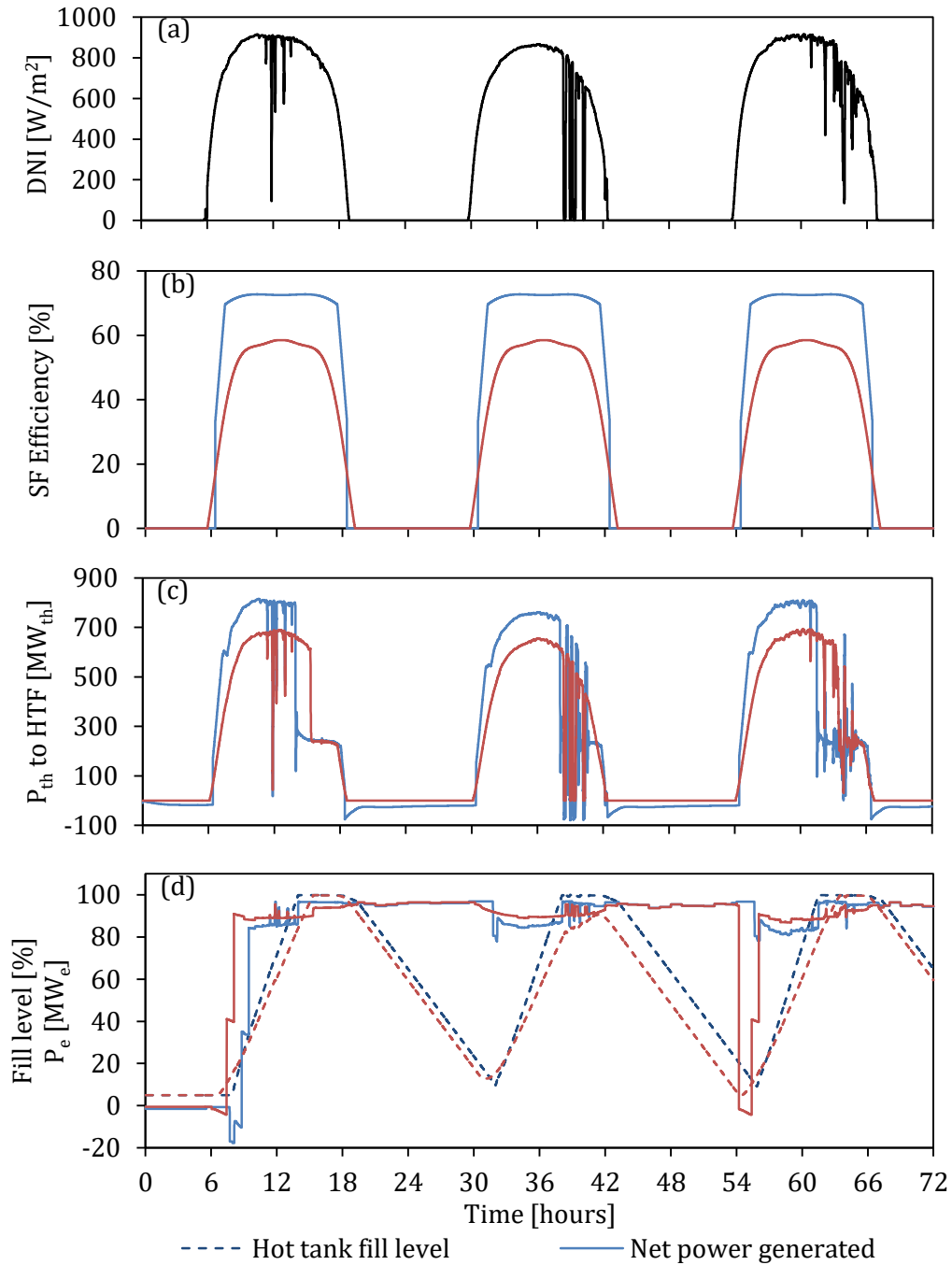


Figure 40: Performance of parabolic trough (blue) and power tower (red) plants over three summer days at the Vryburg site from December 25th.

Simulation of the parabolic trough plant and power tower plant designs in Table 30 and Table 31 resulted in the winter and summer performance curves shown in Figure 39 and Figure 40. The next step in comparing the two technologies is an

annual plant efficiency comparison. Table 32 together with Figure 41 show the annual results of the plants operating under a flat tariff structure.

Table 32: Yield analysis for a power tower and parabolic trough plant design for a flat tariff structure

| Site name | $E_{e,a}$ [GWh _e] | η_{SF} [%] | η_{dump} [%] | η_{rec} [%] | η_{PC} [%] | η_{aux} [%] | η_{net} [%] |
|------------------|----------------------------------|--------------------|----------------------|---------------------|--------------------|---------------------|---------------------|
| Power tower | 501.4 | 49.8 | 99.6 | 84.1 | 42.3 | 90.5 | 15.9 |
| Parabolic trough | 503.3 | 59.7 | 96.4 | 79.0 | 42.3 | 90.9 | 17.5 |

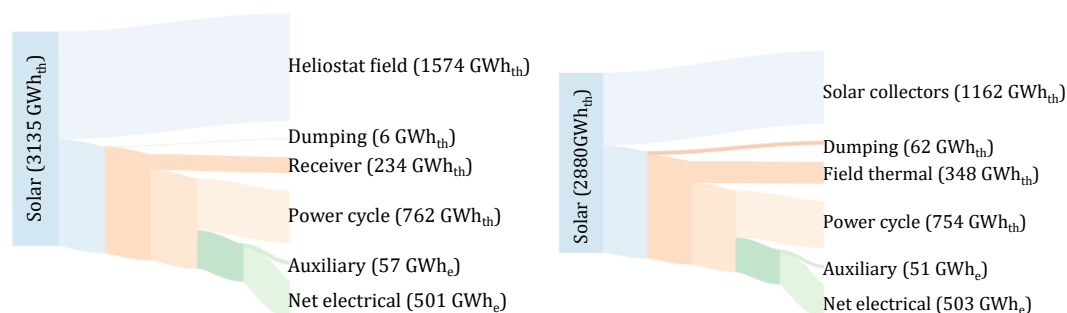


Figure 41: Power tower (left) and parabolic trough (right) loss diagrams for a flat tariff structure

Both plants are shown to generate approximately the same amount of energy (~ 500 GWh_e) over a one year simulation in Vryburg. The parabolic trough plant has a higher annual solar to electric net efficiency of 17.5 % compared to 15.9 % attained by the power tower plant.

The annual solar field efficiency for parabolic trough plant is shown to be notably higher than for power towers. This is in part due to the large heliostat fields, which in turn results in high levels of atmospheric attenuation and a decrease the solar field efficiency. Figure 41 indicates that the losses in the heliostat field are shown to be far greater than the losses in the parabolic trough solar field.

The receiver efficiency for the parabolic trough plant is lower than the power tower as a result of the thermal losses experienced during night-time recirculation of HTF. The power tower plant shows higher dumping efficiency than the parabolic trough plant. This is due to the large variation in optical efficiency of parabolic trough solar collectors, which results in large amounts of thermal energy being collected in summer months. Figure 41 illustrates the large thermal losses and dumping losses experienced by the parabolic trough plant.

The power cycle efficiencies are identical for the two plants as expected, due to the common power cycle model and identical operating temperatures. Gross to net conversion (η_{aux}) of the two technologies is also comparable.

The yield data has been used to evaluate the financial performance of the power tower and parabolic trough plant in this example. The power tower plant has a capital

expense of 540 million USD and a resulting LCOE of 0.147 USD/kWh_e. The parabolic trough plant has a capital expense of 518 million USD a LCOE of 0.141 USD/kWh_e.

The direct comparison of the two plant designs therefore favours parabolic trough technology as it has a lower capital cost and a lower LCOE than the power tower alternative when operating under a flat rate. It is important to note that these plants have been designed to produce the same annual electrical energy, and that they have not been optimized to reduce the cost of electricity for the location.

7.1.2. Operation under a two-tiered tariff structure

In order to show the effect of a two-tiered tariff structure on the operation of the two technologies, both plants were resized to produce 380 GWh_e at the Vryburg site. The plants were designed with smaller solar multiples and smaller storage than the plants designed for the flat tariff structure as follows:

Table 33: Power tower plant design for two-tiered tariff structure

| Parameter | Value | Unit |
|-------------------------------------|---------|-------------------|
| Location | Vryburg | - |
| Design point DNI | 947 | W/ m ² |
| Solar multiple | 2 | - |
| Solar field size | 991 200 | m ² |
| Receiver size | 543 | MW _{th} |
| Power cycle thermal | 240 | MW _{th} |
| Hours of storage | 6 | hours |
| Salt mass | 13 800 | tons |
| Generating capacity | 100 | MW _e |
| Solar field efficiency | 58.0 | % |
| Receiver efficiency | 88.3 | % |
| Power cycle design point efficiency | 41.7 | % |
| Auxiliary efficiency | 90.0 | % |
| Net efficiency | 19.2 | % |

Table 34: Parabolic trough plant design for two-tiered tariff structure

| Parameter | Value | Unit |
|-------------------------------------|-----------|-------------------|
| Location | Vryburg | - |
| Design point DNI | 947 | W/ m ² |
| Solar multiple | 2.4 | - |
| Solar field size | 1 091 000 | m ² |
| Number of loops | 159 | - |
| Power cycle thermal | 240 | MW _{th} |
| Hours of storage | 6 | hours |
| Salt mass | 14 400 | tons |
| Generating capacity | 100 | MW _e |
| Solar field efficiency | 62.2 | % |
| Receiver efficiency | 89.7 | % |
| Power cycle design point efficiency | 41.7 | % |
| Auxiliary efficiency | 90.0 | % |
| Net efficiency | 20.9 | % |

For power tower technology, an increase in solar field size results in a lower optical

design point efficiency due to atmospheric attenuation. In the case of parabolic trough technology, an increase in solar field size has no effect on the optical efficiency of the plant. Increasing solar field area increases the thermal losses from the field as there is a larger length of receiver and distribution piping.

Both plants were simulated for a year of operation at the Vryburg site – the electrical yield and component efficiencies are listed in Table 35. The component losses are analysed in Sankey diagrams in Figure 42.

Table 35: Yield analysis for a power tower plant design for a two-tiered tariff structure

| Site name | $E_{e,a}$ [GWh _e] | η_{SF} [%] | η_{dump} [%] | η_{rec} [%] | η_{PB} [%] | η_{aux} [%] | η_{net} [%] |
|------------------|----------------------------------|--------------------|----------------------|---------------------|--------------------|---------------------|---------------------|
| Power tower | 380.8 | 50.4 | 97.0 | 84.8 | 42.2 | 91.2 | 15.7 |
| Parabolic trough | 380.0 | 58.4 | 79.9 | 75.3 | 42.1 | 90.7 | 14.3 |

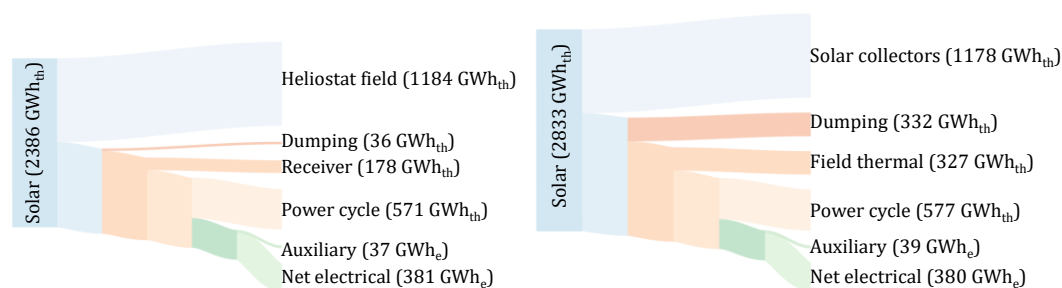


Figure 42: Power tower (left) and parabolic trough (right) loss diagrams for a two-tiered tariff structure

The most notable difference between the losses under the flat tariff and the two-tiered tariff structure is the level of dumped energy. The level of dumping in both plants increases due to the smaller storages that are used. Once again, the parabolic trough plant experiences large dumping losses due to its seasonal variation in optical efficiency.

The receiver efficiency of the parabolic trough plant has improved compared to the previous plant design. The smaller solar field results in lower thermal losses during recirculation, improving the annual receiver thermal efficiency.

Both plants show a small drop in power cycle efficiency. This is due to the increased number of start-ups experienced while operating under a two-tariff structure.

The yield data has been used to evaluate the financial performance of the power tower and parabolic trough plant in this example. The power tower plant has a capital expense of 408 million USD and a resulting LCOE of 0.151 USD/kWh_e. The parabolic trough plant has a capital expense of 445 million USD and a LCOE of 0.163 USD/kWh_e. The direct comparison of the two plants therefore favours power tower technology as it has a lower capital cost and a lower LCOE than the power tower alternative when operating under a flat rate. Once again, it is important to note that these plants have been designed to produce the same annual electrical

energy, and that they have not been optimized to reduce the cost of electricity for the location.

7.2. Optimization of plant design

At each site the optimum design of a plant is different. The two major design decisions when sizing a CSP plant are the solar field size and the storage size. In an attempt to find the optimum design, a parametric analysis was carried out where the solar multiple and storage hours were varied for each of the technologies at each of the sites.

Levelized cost of electricity (LCOE) is used to evaluate the performance of plants operating under the flat tariff system. The LCOE considers the net electrical energy generated per year, the capital cost and the operating cost of a plant (Section 5.9). Levelized profit of electricity (LPOE) is used to determine the performance of a plant under the two-tier tariff structure. This allows for the determination of the CSP system with the most profitable configuration.

The optimization of a power tower plant in Springbok, operating under a flat tariff, is illustrated in Figure 43. The optimum design is a solar multiple of 2.8 with 14 hours of storage. This correlates to an LCOE of 0.129 USD/kWh_e.

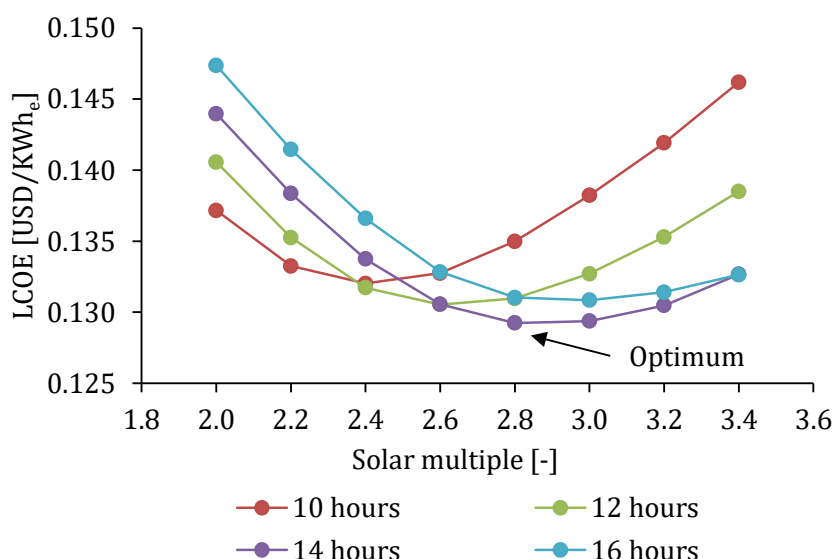


Figure 43: Optimization of a power tower plant at the Springbok site according to levelized cost of electricity

The optimization of a power tower plant in Springbok operating under the REIPPPP two-tariff system is illustrated in Figure 44. The optimum design is a solar multiple of 2.2 with 6 hours of storage. This correlates to an LPOE of 0.059 USD/kWh_e. It is interesting to observe that if the power tower plant in Figure 44 had been optimized according to LCOE, the optimum design point would remain at a solar multiple of 2.2, however, a storage size of 8 hours would be selected. This shows that even though the optimum combination of SM=2.2 and 6 hours of storage does not result

in the lowest cost of electricity, it is the most profitable under the two-tariff structure, and therefore is selected as the optimum design.

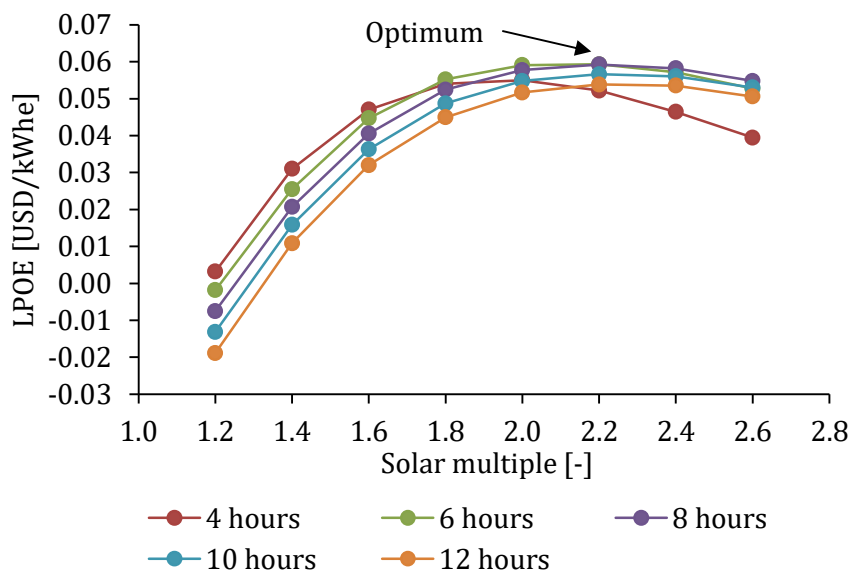


Figure 44: Optimization of a power tower plant at the springbok site operating under the two-tiered tariff system according to levelized profit of electricity

7.3. Optimized plant simulation results

The optimization process illustrated in Figure 43 and Figure 44 was repeated for both technologies at each of the six selected sites. The optimum plant designs for a flat tariff structure are listed in Table 36 and Table 37. The optimum plant designs for a two-tiered tariff structure are listed in Table 38 and Table 39.

Figure 43 and Figure 44 as well as the optimized plant tables show the differences in plant design under two different feed in tariffs. Under a flat tariff, a large storage (14 hours) and large solar multiple results in a lower cost of electricity. This is primarily due to the fact that the plant will generate a large amount of electricity during the year.

Under the two-tiered tariff, a smaller storage (6 to 8 hours) and solar multiple (2.0 to 2.4) results in an optimum configuration. This is because the plant is only required to generate electricity at certain hours during the day. A smaller storage allows the plant to generate electricity during the day and the peak hours in the evening without the added cost of storing energy for overnight electricity generation.

Table 36: Optimized power tower plant designs for a flat tariff structure

| Site name | DNI $\left[\frac{\text{kWh}_{th}}{\text{m}^2}\right]$ | AsF [m ²] | Storage [hours] | $E_{e,a}$ [GWh _e] | CAPEX [mil USD] | OPEX [mil USD] | LCOE $\left[\frac{\text{USD}}{\text{kWh}_e}\right]$ |
|------------|--|--------------------------|--------------------|----------------------------------|--------------------|-------------------|--|
| Springbok | 2798 | 1.316 | 14 | 582.1 | 549.2 | 8.3 | 0.129 |
| Upington | 2581 | 1.378 | 14 | 557.8 | 560.8 | 8.3 | 0.137 |
| Molteno | 2449 | 1.457 | 14 | 539.0 | 583.8 | 8.2 | 0.147 |
| Vryburg | 2443 | 1.523 | 14 | 570.7 | 596.1 | 8.3 | 0.142 |
| Laingsburg | 2652 | 1.358 | 14 | 551.0 | 557.0 | 8.3 | 0.138 |
| Kimberley | 2482 | 1.511 | 14 | 560.8 | 593.8 | 8.3 | 0.144 |

Table 37: Optimized parabolic trough plant designs for a flat tariff structure

| Site name | DNI $\left[\frac{\text{kWh}_{th}}{\text{m}^2}\right]$ | AsF [m ²] | Storage [hours] | $E_{e,a}$ [GWh _e] | CAPEX [mil USD] | OPEX [mil USD] | LCOE $\left[\frac{\text{USD}}{\text{kWh}_e}\right]$ |
|------------|--|--------------------------|--------------------|----------------------------------|--------------------|-------------------|--|
| Springbok | 2798 | 1.064 | 14 | 531.5 | 485.6 | 8.2 | 0.127 |
| Upington | 2581 | 1.009 | 14 | 472.9 | 470.2 | 8.0 | 0.138 |
| Molteno | 2449 | 1.105 | 14 | 461.8 | 497.0 | 8.0 | 0.148 |
| Vryburg | 2443 | 1.277 | 14 | 527.3 | 544.9 | 8.2 | 0.141 |
| Laingsburg | 2652 | 1.064 | 14 | 491.2 | 485.6 | 8.1 | 0.137 |
| Kimberley | 2482 | 1.236 | 14 | 507.3 | 533.4 | 8.1 | 0.144 |

Table 38: Optimized power tower plant designs for a two-tiered tariff structure

| Site name | DNI $\left[\frac{\text{kWh}_{th}}{\text{m}^2}\right]$ | AsF [m ²] | Storage [hours] | $E_{e,a}$ [GWh _e] | CAPEX [mil USD] | OPEX [mil USD] | LCOE $\left[\frac{\text{USD}}{\text{kWh}_e}\right]$ |
|------------|--|--------------------------|--------------------|----------------------------------|--------------------|-------------------|--|
| Springbok | 2798 | 1.020 | 6 | 424.4 | 421.3 | 7.9 | 0.139 |
| Upington | 2581 | 1.068 | 6 | 409.5 | 430.3 | 7.8 | 0.147 |
| Molteno | 2449 | 1.150 | 8 | 416.3 | 465.9 | 7.8 | 0.155 |
| Vryburg | 2443 | 1.096 | 6 | 404.5 | 435.6 | 7.8 | 0.150 |
| Laingsburg | 2652 | 0.951 | 6 | 384.3 | 400.4 | 7.8 | 0.147 |
| Kimberley | 2482 | 1.192 | 8 | 436.9 | 473.8 | 7.9 | 0.150 |

Table 39: Optimized parabolic trough plant designs for a two-tiered tariff structure

| Site name | DNI $\left[\frac{\text{kWh}_{th}}{\text{m}^2}\right]$ | AsF [m ²] | Storage [hours] | $E_{e,a}$ [GWh _e] | CAPEX [mil USD] | OPEX [mil USD] | LCOE $\left[\frac{\text{USD}}{\text{kWh}_e}\right]$ |
|------------|--|--------------------------|--------------------|----------------------------------|--------------------|-------------------|--|
| Springbok | 2798 | 0.803 | 8 | 393.9 | 376.9 | 7.8 | 0.136 |
| Upington | 2581 | 0.920 | 8 | 389.7 | 409.3 | 7.8 | 0.148 |
| Molteno | 2449 | 0.920 | 8 | 361.3 | 409.4 | 7.7 | 0.159 |
| Vryburg | 2443 | 1.002 | 8 | 408.3 | 432.4 | 7.8 | 0.149 |
| Laingsburg | 2652 | 0.776 | 8 | 354.2 | 369.2 | 7.7 | 0.149 |
| Kimberley | 2482 | 0.954 | 8 | 381.7 | 419.0 | 7.7 | 0.154 |

A comparison of the LCOE, capital cost and net electrical yield of parabolic trough and power tower plants at the various locations is shown in Figure 45. The lowest LCOEs and highest electricity generation figures occur at the Springbok site, as is expected with the high solar resource available. The next lowest LCOE values are attainable at the Laingsburg site.

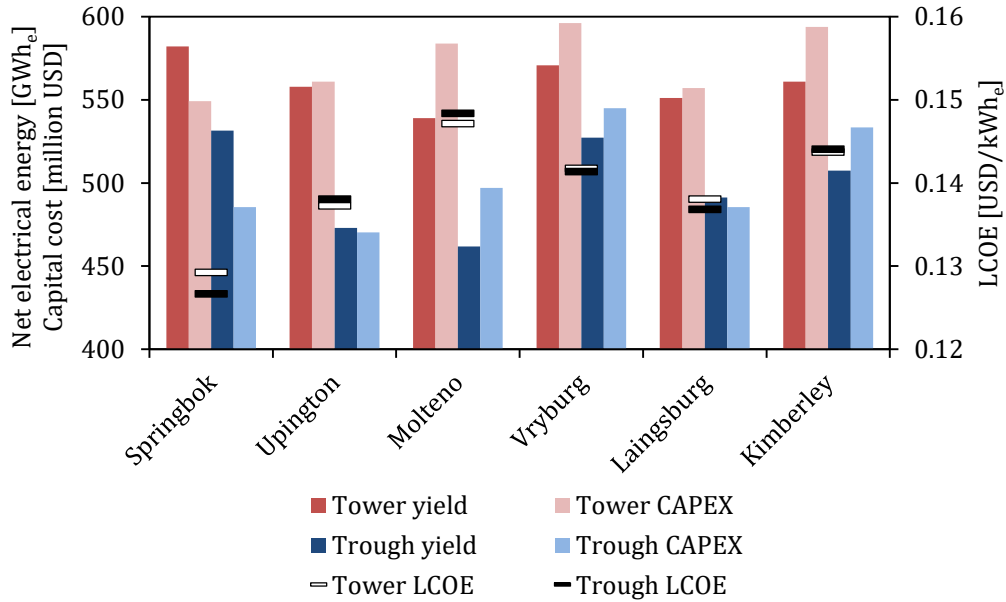


Figure 45: Electrical yield, capital cost and LCOE comparison of parabolic trough and power tower plants at the six locations operating under a flat tariff structure

Figure 46 illustrates the performance of technologies according to LCOE and electrical yield while operating under the two-tiered tariff. Once again the lowest LCOE is attainable at the Springbok site, with the Upington and Laingsburg sites as the best alternatives.

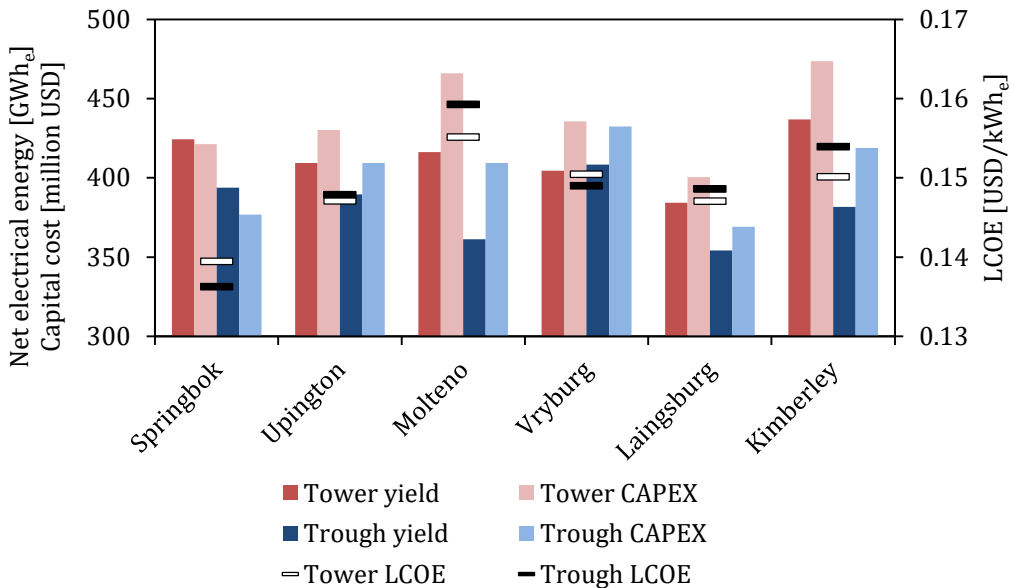


Figure 46: Electrical yield, capital cost and LCOE comparison of parabolic trough and power tower plants at the six locations operating under a two-tier tariff structure

7.4. Discussion

This section contains a discussion of the parabolic trough and power tower plants performance at the selected sites under the two-tiered tariff structures.

Table 36 and Table 37 show that the optimum solar multiples of the parabolic trough plants are generally lower than the power tower plants. There are two reasons for this: (1) the cost of a parabolic trough solar field, which includes the cost of the HTF system and the solar collectors, equates to a total cost of 248 USD/m², compared to the power tower solar field cost of 170 USD/m². (2) The overnight thermal losses for the of the parabolic trough plant increase dramatically as the size of the solar field increases.

The power tower plants are shown to have an optimum solar field area that tends to be larger than those of the parabolic trough plants. This is determined to be a result of the combination of the high cost of a parabolic trough solar field per m² and the large thermal losses experienced in the solar field of parabolic trough plants.

The net electrical yield of the optimized power tower plants is on average 12.5 % higher than the parabolic trough plants. The LCOE of the two technologies at each of the sites is closely comparable. Using power towers results in a lower LCOE at the Upington, Molteno and Kimberley sites, while parabolic trough plants result in the lower LCOE at the Springbok, Vryburg and Laingsburg sites.

When comparing LCOE of the two technologies, it is important to consider that it is very sensitive to the cost estimates made in Section 5.9. A sensitivity analysis is carried out in Appendix D. The sensitivity analysis shows that the parabolic trough and power tower plants are very sensitive to the selected discount rate, solar field costs per m² and the EPC cost percentage. Therefore the LCOE of both technologies is likely to change in the near future as the cost of the different components vary.

The lowest achievable LCOE is shown to be 0.127 USD/kWh_e achieved using parabolic trough technology at the Springbok site. The plant would cost an estimated 486 million USD and yield 532 GWh_e per annum. In comparison, an optimized power tower plant at the same site achieves an LCOE of 0.129 USD/kWh_e. The power tower plant will cost 549 million USD and yield 582 GWh_e per annum. The Springbok site results in low LCOE values because of its substantial solar resource. It must be considered that both LCOE figures are sensitive to their different component costs, most notably the solar field costs (Appendix D).

When comparing the results of the optimization process under the different tariff structures it is evident that the flat rate results in larger plants with a higher capital cost and the two-tiered tariff results in smaller plants with a lower capital cost. The implementation of a two-tiered tariff results in an average increase of 7 % in LCOE for both of the plants. This is because the plants have no incentive to generate electricity at night, which results in substantially lower annual electrical energy yields compared to flat tariffs. The low electrical yield results in a higher levelized cost of electricity.

The lowest achievable LCOE under the two-tiered tariff is shown to be 0.136 USD/kWh_e, which is once again achieved using parabolic trough technology at

the Springbok site. The plant would cost an estimated 377 million USD and yield 394 GWh_e per annum. In comparison, an optimized power tower plant at the same site achieves an LCOE of 0.139 USD/kWh_e. The power tower plant will cost 421 million USD and yield 424 GWh_e per annum.

Under the two-tiered tariff power tower plants result in a lower LCOE at the Upington, Molteno, Laingsburg and Kimberley sites, while parabolic trough plants result in the lower LCOE at the Springbok and Vryburg sites. All sites, except the Vryburg site, show the power tower plants optimized to produce more electrical energy.

At the Vryburg site the parabolic trough plant has a higher electrical yield and a lower LCOE. The distribution of solar resource for each of the sites is illustrated in Appendix E. When comparing the available DNI at Laingsburg and Vryburg, it is evident that the Laingsburg site experiences very high levels of DNI in the winter and lower levels in the winter, while at the Vryburg site the available DNI in the summer and winter remains constant. Parabolic trough technology is well suited to a site such as Vryburg because constant DNI across the year reduces the amount of dumping typically experienced by a parabolic trough plant during summertime operation.

7.5. Conclusion

An in-depth comparison of the two technologies under operation at the Vryburg site was performed in order to illustrate the primary differences between the two technologies. It is concluded that the power tower plants have a lower annual optical efficiency than the parabolic trough plants. However, the parabolic trough plants suffer from substantial thermal losses as the HTF is circulated in the field overnight whereas the power tower receiver is drained overnight.

The performance of the optimized plants at the selected locations show that under a flat tariff structure, power tower plants are better suited to larger solar fields – resulting in higher capital expenditure but an increase annual electrical yield. Parabolic trough plants are better suited for smaller solar field results in higher thermal efficiency and a lower capital cost of the plant.

An unexpected finding of the simulations was that the parabolic trough plant operating under the two-tiered tariff structure performs comparatively well at the Vryburg site. This is determined to be a result of the constant levels of DNI in the summer and winter time. This finding indicates that the distribution of solar resource over the year should be considered when selecting a CSP technology.

8. Conclusion

8.1. Summary of findings

The investigation into molten salt parabolic trough plants identified freeze protection and overnight thermal losses as the primary design concerns. Simulations using the parabolic trough model have shown that the method of using residual thermal energy in the cold tank as freeze protection during overnight recirculation is effective. While the method results in increased thermal losses overnight, it eliminates the need for inefficient joule resistance heating in the solar field during operation.

The difference in performance of parabolic trough and power tower plants is found to be a result of three main component efficiencies:

- *Solar field efficiency* - parabolic trough solar collectors result in higher annual solar field efficiency than the heliostat field of a power tower plant.
- *Receiver thermal efficiency* - the power tower central receiver is drained when it is not in operation, limiting thermal losses and increasing the annual efficiency. In a parabolic trough plant the HTF is circulated through the receiver tubes continuously to prevent freezing. This circulation results in thermal losses which reduce the thermal efficiency of the plant.
- *Dumping of solar energy* - Parabolic trough solar fields show a large seasonal variation in efficiency while power tower plants are shown to benefit from relatively consistent solar field efficiency throughout the year. The seasonal variation in solar field efficiency results in substantially higher thermal energy being available in the summer than in the winter which results in storages being filled and the subsequent dumping of solar energy.

The optimization of solar field and storage size to achieve the lowest possible LCOE at six different sites in South Africa has shown that parabolic trough plants have smaller optimum solar field sizes when compared to power towers. The smaller parabolic trough plants tend to produce less electrical energy per year, but have a lower cost compared to the optimized power tower plants.

The LCOE calculations performed in this study use estimated component costs for a 100 MW_e parabolic trough and power tower plant. The LCOE results are highly sensitive to changes in the cost of components. Using the latest available cost estimations, the parabolic trough plants have shown to generate the lowest LCOE value of 0.127 USD/kWh_e at the Springbok site. The power tower plant at the Springbok site was shown to provide the lowest LCOE of 0.129 USD/kWh_e.

Two additional findings were made in a South African context:

- *Site selection* - Springbok holds the highest potential for a low cost of generating electricity, however, the transmission access and water availability at the sites in the Northern Cape are limited. The Laingsburg site

has been identified as the site with the highest potential for CSP, as it has high DNI values coupled with access to a substation and surface water.

- *Tariff structure* - Plants designed under the two-tariff structure have smaller optimum storage and solar field sizes. The fact that there is no tariff paid for generating electricity overnight results in plants with lower annual efficiency and higher LCOE when compared to the flat tariff plants.

8.2. Conclusion

Pending the successful commercialization of the technology, this study indicates that molten salt parabolic trough plants may be a feasible CSP solution.

The comparison between parabolic trough and power tower plants has shown that both technologies have a variety of strengths and weaknesses. The models developed are shown to be a useful tool for comparing the two technologies at different sites under different operating conditions.

In a South African context, the Springbok site in the Northern Cape Province is shown to provide the potential for the lowest LCOE for both technologies thanks to the abundant solar resource in the region. The site with the next greatest potential was shown to be Laingsburg in the Western Cape Province. Additionally, it was found that the two-tiered tariff structure currently being implemented by the REIPPP results in an increase in LCOE and a decrease in plant efficiency compared to a conventional flat feed in tariff structure.

8.3. Contributions

The description and modelling of a large-scale molten salt parabolic trough plant indicates that the technology may be competitive to molten salt power tower plants, and therefore encourages further research into the technology. The models developed in this study provide a means to use high resolution DNI data in order to estimate the performance of molten salt parabolic trough and power tower plants.

A paper written using the power tower model developed in this study is to be presented at SolarPACES 2016: "A High Temporal Resolution Molten Salt Tower Model used for Site Selection with South African Infrastructure Considerations". Furthermore, a paper written on the method used for generating high resolution DNI using SAURAN data is to be presented at SASEC 2016: "Increasing the Temporal Resolution of Direct Normal Solar Irradiance Data Using the South African Universities Radiometric Network". The SolarPACES and SASEC papers are intended for publication.

8.4. Recommendations for further work

The operation strategy implemented in the molten salt model for freeze protection and start-up has not been tested. The strategy shows high potential to reduce the required costs of trace heating and freeze protection. The parabolic trough plant is most sensitive to solar field costs, and any savings that can be made in the field may effectively reduce the levelized cost of electricity. It is recommended that this

strategy be tested on a molten salt test bench or possibly a demonstration loop such as Archimede Solar Energy or the Evora Molten Salt Platform.

The system-level models used in this work utilized simplified component models. Further work to improve the detail and accuracy of these models would lead to an increasingly accurate yield and financial analysis model.

In order for a performance model to be accepted for further development, validation is required. The power tower model could potentially be validated using operating data from commercial molten salt power tower. Alternatively the individual components could be analyzed using small scale testing.

The Laingsburg site investigated in this study showed a large amount of potential for future development. The site has high solar radiation, access to an electrical substation and access to water. An in depth feasibility study into this site is recommended.

Appendix A: Synthetically developed direct normal irradiance data

A.1. The effect of direct normal irradiance data on plant modelling

As discussed in Section 2.5 of the literature review, in order to accurately calculate the daily yield of a CSP plant it is essential to account for high-resolution temporal variability of the site data (Meyer *et al.*, 2009).

The reason that hourly averaged DNI data is not acceptable for accurate daily yield analysis of a CSP plant is because hourly measurements are too infrequent to capture the transient effects of clouds (Grantham *et al.*, 2013). The transient nature of DNI causes a nonlinear response of a CSP plant. The effect of using minute averaged data as opposed to hour averaged data has been investigated when modelling a parabolic trough plant (Beyer *et al.*, 2010). It was found that using hourly data resulted in an overestimation of daily electrical energy yield of between 10 % and 20 % (Figure 47).

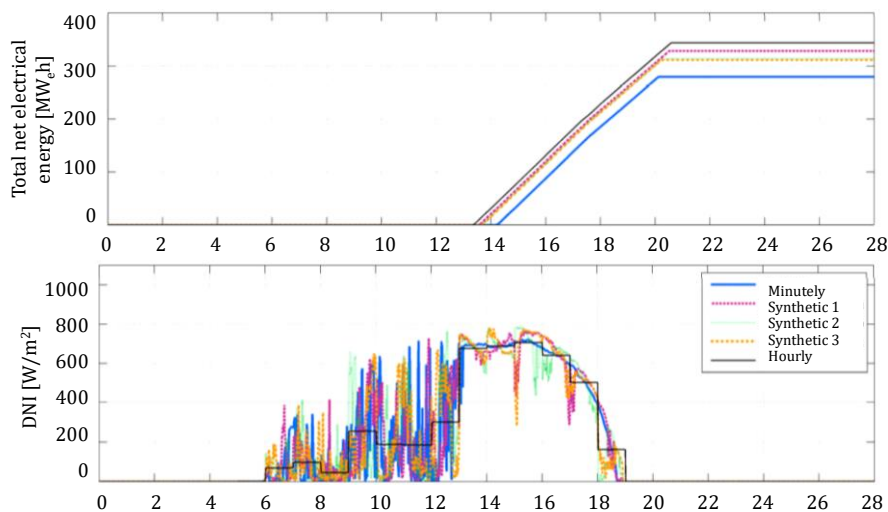


Figure 47: Daily time trace of the accumulated electrical energy as simulated on the bases of measured and synthesized minutely DNI data sets and on a set with hourly time resolution (Beyer *et al.*, 2010)

Figure 48 illustrates the effect of varying temporal resolution DNI data on the parabolic trough (a) and power tower models (b) from this study. Hourly DNI data shows a ~45 % higher electrical yield for both the power tower and parabolic trough models when compared to minute resolution data.

The synthetic minute resolution data is generated using the method described in the Section to follow.

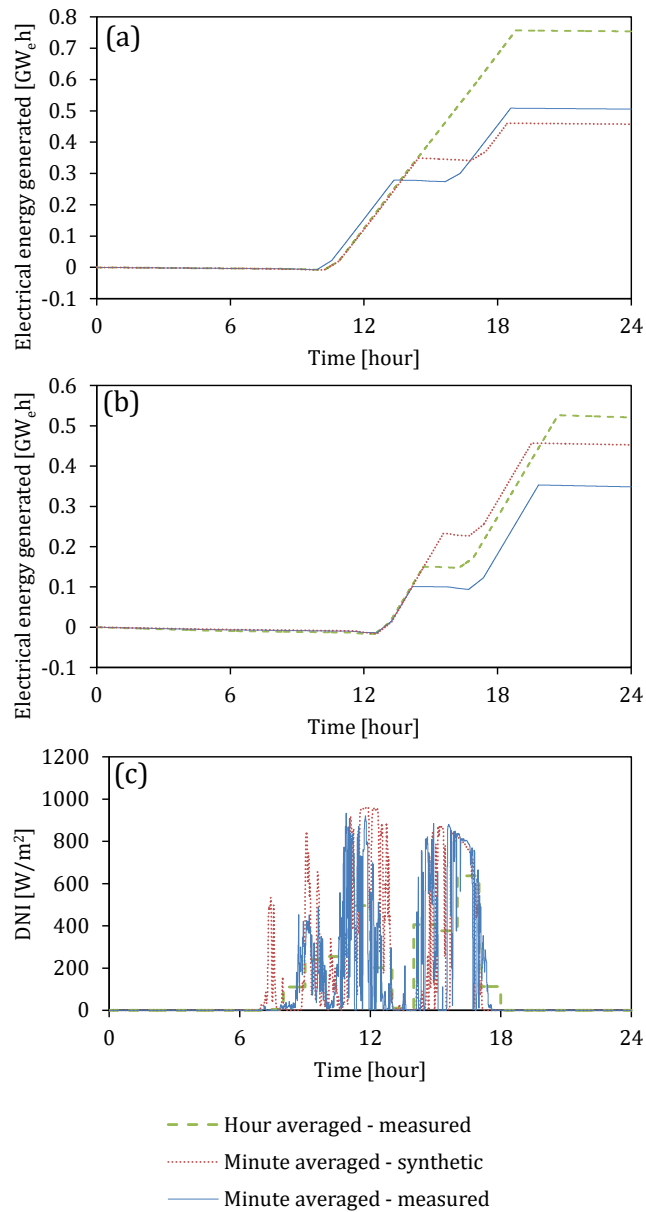


Figure 48: Evaluating the effect of hour vs. minute averaged data

While the resolution of DNI data may have a large impact on daily electrical yield over one day with low DNI, it does not have a major effect on annual electrical yield. Simulations with the parabolic trough and power tower models showed a difference in annual electrical yield of $\sim 1\%$. High resolution DNI data is therefore more important for daily yield analysis than annual yield analysis.

As discussed in Section 3, the monitoring of fluid temperatures in the parabolic trough solar field is important to ensure that freezing does not occur. The effect of varying DNI temporal resolution on the HTF temperatures in the parabolic trough solar field and storage tanks is illustrated in Figure 49.

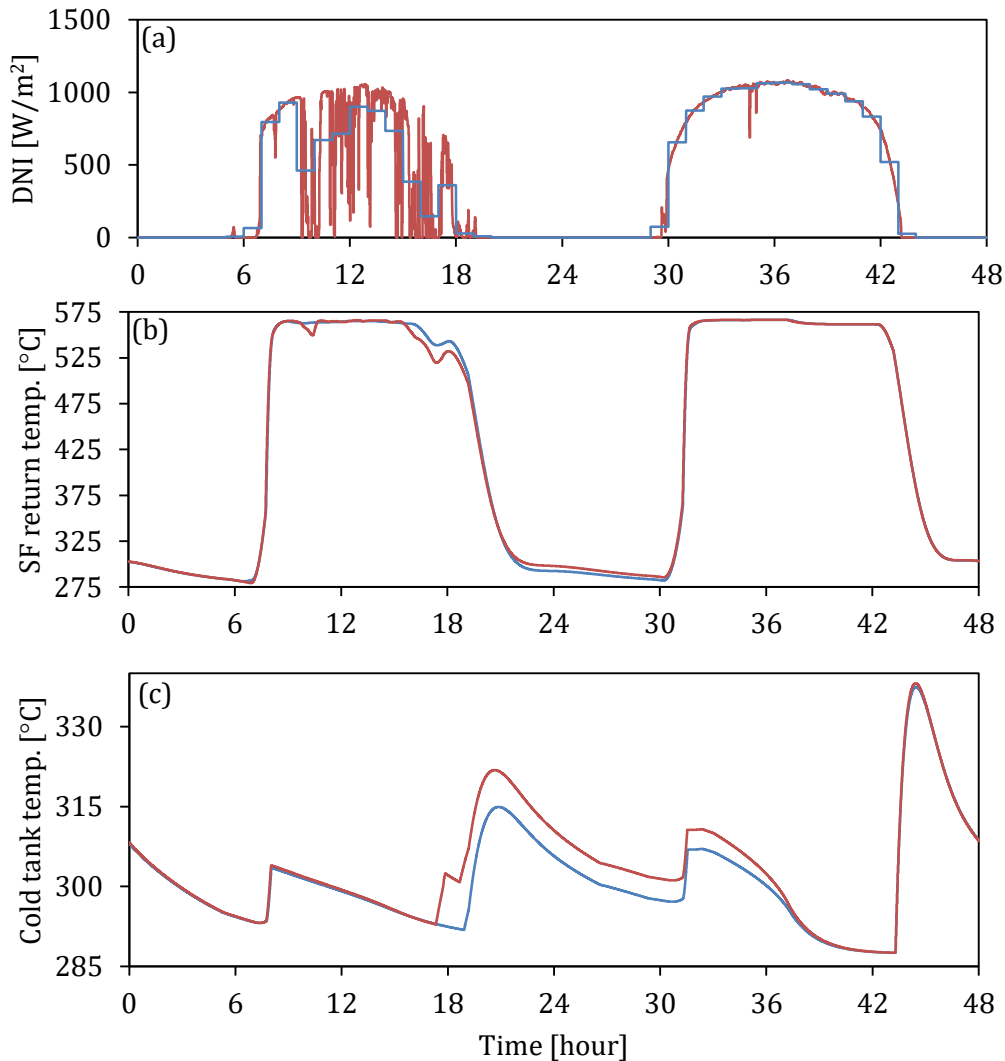


Figure 49: Comparing the effect of minute resolution (red) vs. hour resolution (blue) DNI on parabolic trough solar field return temperature and cold tank storage temperature

Figure 49(a) shows the minutely and the hourly DNI. Figure 49(b) illustrates how the return temperature from the solar field differs using the different time resolutions. Hourly resolution DNI results in a constant outlet temperature of 565 °C, even during partly cloudy days. The minute resolution DNI results in the outlet temperatures dropping below 565 °C as a result of the fluctuating DNI.

Due to the lower solar field outlet temperature, the minute resolution model diverts HTF to the cold tank for recirculation sooner than the hour resolution model. This results in a 10 °C difference in the cold tank temperature overnight as shown in Figure 49(c).

Therefore the result of the increased resolution of the DNI results in different solar field outlet temperatures and cold tank temperatures. Minute resolution DNI is therefore important in determining the accurate fluid temperature. This is valuable in the modelling of parabolic trough plants considering the importance of

monitoring solar field and storage tank HTF temperature in order to prevent freezing when designing a plant with molten salt as HTF.

A.2. Method for generating synthetic irradiation data

The method proposed by Fernandez-Peruchena *et al.* uses a technique for the nondimensionalization of a series of ground measured, high frequency daily DNI curves. The process of nondimensionalization transforms each measured day into a dimensionless signature that can be used to create high resolution DNI data from hourly DNI data.

The first step of this process is to calculate a clear sky envelope for each of the 365 measured days. The characteristic peaks of the DNI curve are identified using a simple filtering method (Figure 50(a)). The equation for the clear sky envelope is defined as:

$$DNI_{env} = E_0 \exp\left(-\frac{\kappa}{\sin(\alpha)}\right) \quad (\text{A.1})$$

Curve fit parameters (E_0 and κ) are used to adjust the envelope curve to fit the DNI curve of each given day. In order to determine the best fit envelope, the characteristic peaks are inputted into a linearized envelope equation:

$$\log(DNI_{env}) = \log(E_0) - \log\left(\frac{1}{\sin(\alpha)}\right) \quad (\text{A.2})$$

The Matlab® polyfit function (The MathWorks Inc., 2015a) is then used to determine a linear curve fit for the resulting points (Figure 50(b)). The E_0 and κ values are then used in Equation A.2 to generate a well fit DNI envelope (Figure 50(c)).

The fitted envelope is then used to generate a dimensionless DNI curve for each day. At each time step the measured DNI value is divided by the value of the envelope curve. In order to nondimensionalize the time scale the elapsed solar time starting at sunrise is divided by the day length for each individual day. The result of the nondimensionalization is a high resolution DNI signature for the day that has a time scale and a DNI scale ranging from 0 to 1 (Figure 50(d)).

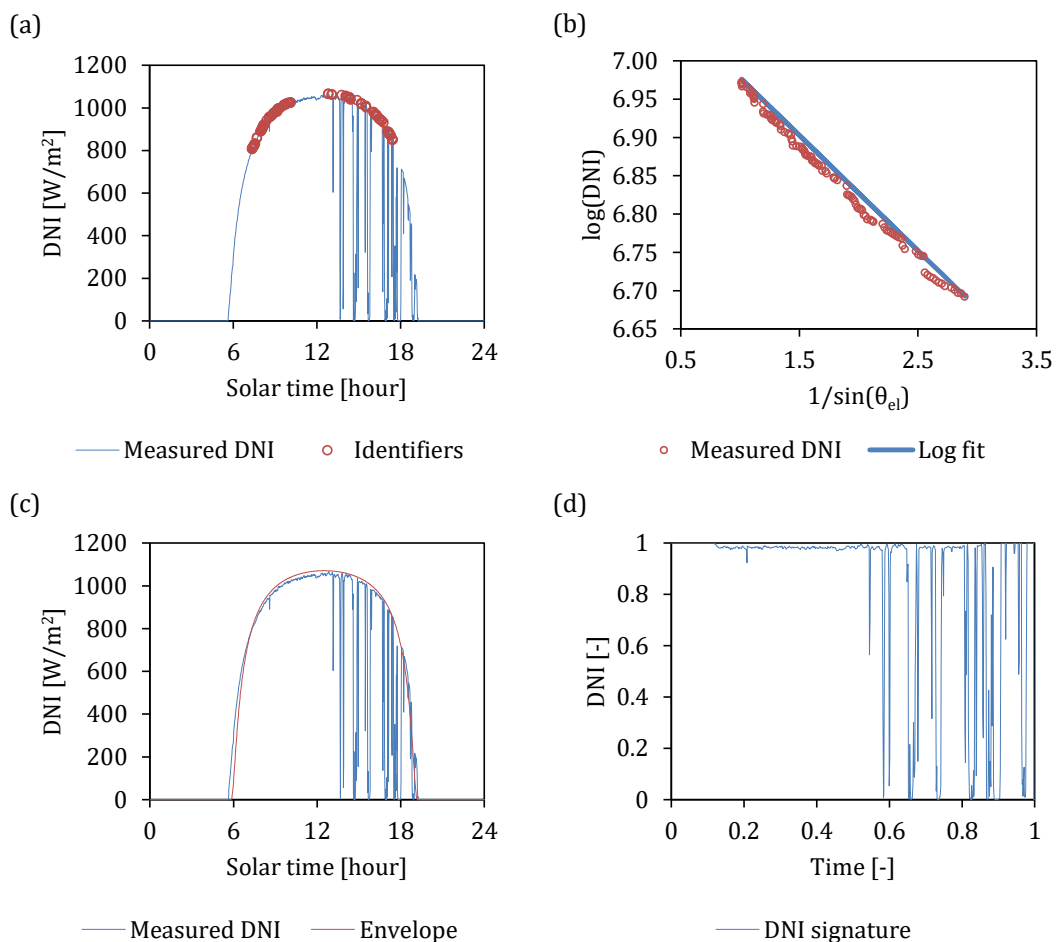


Figure 50: The process of generating a dimensionless DNI signature (Fernández-Peruchena *et al.*, 2015)

Dimensionless signatures are developed using the process illustrated in Figure 50 for all 365 days of the measured high resolution DNI data.

For each day of the hour averaged data range, a clear sky envelope is fit to the DNI curve. Each of the high resolution signatures is then applied to the clear sky envelope. This results in an estimated minute resolution DNI curve for the day.

An algorithm is then used to search for the most appropriate signature to fit the given DNI curve in terms of the Euclidean distance between hourly values of the measured and generated DNI series. The best fit signature is selected for each of the days, which results in a full year of synthetically generated DNI data.

A.3. Evaluation of synthetic direct normal irradiation data

In order to evaluate the accuracy of the method described in the previous section, it was applied to hourly and minutely DNI measured at two SAURAN stations. The DNI datasets used were taken from SAURAN stations at the University of the Free State (UFS) in Bloemfontein and Graaff-Reinet (GRT) in the Eastern Cape (Table 40).

Table 40: SAURAN station locations

| Station | Lat. [°] | Long. [°] | Elev. [m] |
|---------|----------|-----------|-----------|
| UFS | -29.110 | 26.185 | 1491 |
| GRT | -32.485 | 24.585 | 660 |

The datasets were collected by Kipp & Zonen CH1 Pyrheliometers mounted onto Solsys solar trackers. Both stations were calibrated in the second half of 2013. Minute averaged DNI datasets were used from both stations for the 2014 and 2015 years. Hour averaged datasets were also used for the 2014 year. A simple quality control procedure was used to detect any missing data points or irregularities in measurement.

A.3.1. Daily comparison of measured and synthetically generated data

In order to evaluate the performance of the method when using SAURAN data, the generated data is compared to the measured data for four different days at the Bloemfontein site (Figure 51).

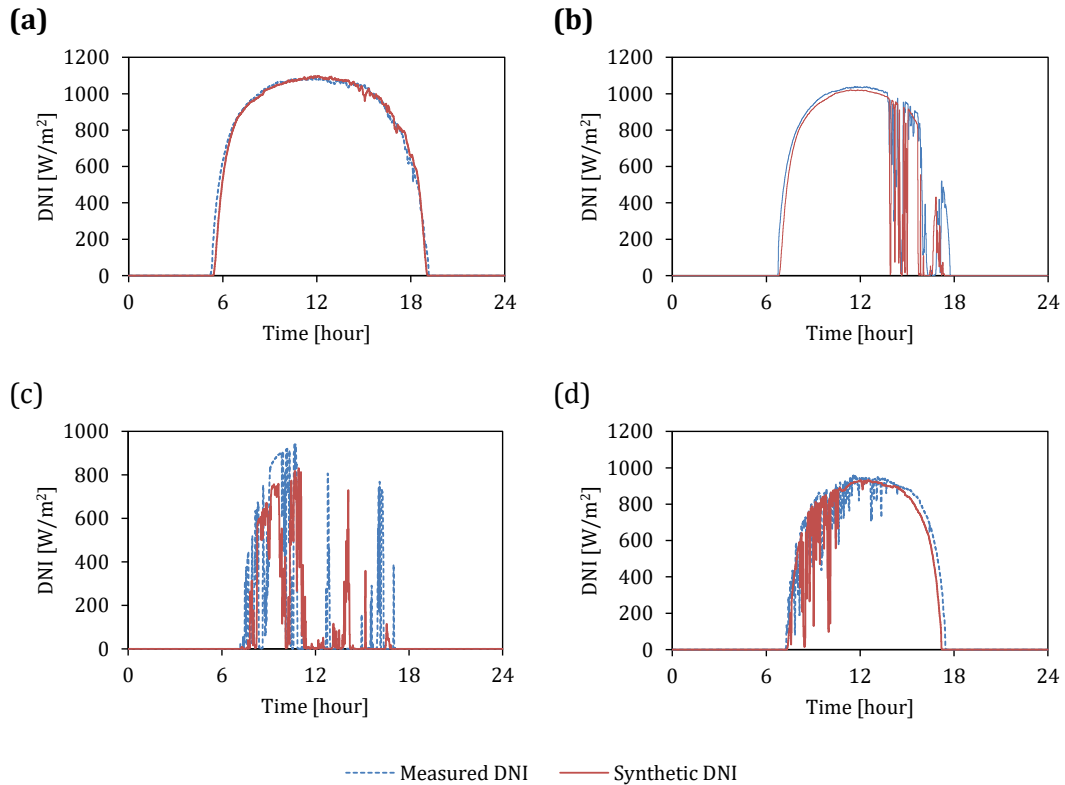


Figure 51: Comparison of measured and synthetically generated direct normal irradiance data from Bloemfontein

Figure 51(a) shows a clear day with no cloud cover. The method generates a very similar DNI curve to the measured DNI curve for when there are no cloud transients influencing the available solar resource.

Figure 51(b) shows days with scattered clouds during an extended portion of the day. The model appears to accurately generate the DNI curve of a day with clear skies in the morning and scattered clouds in the afternoon. This DNI pattern is typical in Bloemfontein.

Figure 51(c) compares the performance during days with frequent clouds and low DNI. This example shows the limitation of the method. The generated DNI curve does not match the measured curve in the morning; it then overcompensates with a peak as the time approaches noon. The accuracy could be improved using a larger high resolution data set, which would lead to improved characterization of the DNI curves and a more accurate matching of generated and measured data.

It must be noted that the method does not precisely predict individual data points. However, it successfully predicts characteristic fluctuations in DNI at the correct periods in the day while ensuring that the total available solar energy remains constant.

A.3.2. Annual statistical comparison of measured and synthetically generated data

This section evaluates the performance of the method in generating a full year (2014) of high resolution DNI data from hour averaged data for the two selected locations. The evaluation is performed by comparing the observed minute averaged data to the generated minute average data.

The measured minute averaged values for the 2014 datasets were used to evaluate the accuracy of the generated minute averaged data set. Statistical indicators were used in order to determine how accurately the generated data matches the measured data on an annual basis. A review of the statistical indicators for modeled solar radiation (Gueymard, 2014) was used as a basis for the evaluation of the generated (or predicted) and measured data.

For the purpose of statistical evaluation, the measured DNI values are referred to as the observed values and the generated DNI values are referred to as the predicted values.

Indicators of dispersion were used to compare the predicted DNI data points (p_i) to the observed data points (o_i). The two indicators of dispersion used were the normalized root mean square deviation (NRMSD) and the mean bias deviation (MBD).

$$MBD = \frac{\frac{1}{N} \sum_{i=1}^N (p_i - o_i)}{O_m} \quad (A.3)$$

$$NRMSD = \frac{\sqrt{\frac{1}{N} \sum_{i=1}^N (p_i - o_i)^2}}{o_{max} - o_{min}} \quad (A.4)$$

Where o_{max} and o_{min} represent the maximum and minimum DNI values of the observed range and O_m represents the average of the observed range. The number of data points in the set is denoted as N . Values tending towards zero for the indices of dispersion represent a significant correlation between the predicted and observed datasets.

In order to get an indication of the overall statistical performance of the method used, the Nash-Sutcliffe efficiency (NSE), the Willmott index of agreement (WIA) and the Legates coefficient of efficiency (LCE) were used.

$$NSE = 1 - \frac{\sum_{i=1}^N (p_i - o_i)^2}{\sum_{i=1}^N (o_i - O_m)^2} \quad (A.5)$$

$$WIA = 1 - \frac{\sum_{i=1}^N (p_i - o_i)^2}{\sum_{i=1}^N (|p_i - O_m| + |o_i - O_m|)^2} \quad (A.6)$$

$$LCE = 1 - \frac{\sum_{i=1}^N |p_i - o_i|^2}{\sum_{i=1}^N |o_i - O_m|^2} \quad (A.7)$$

The overall performance methods indicate 1 for perfect agreement and either $-\infty$ (NSE and WIA) or 0 (LCE) for complete disagreement.

In order to calculate the similarity between the generated and measured DNI data, the Kolmogorov-Smirnov test Integral (KSI) index was used. The KSI calculates the integrated difference between the cumulative distribution functions (CDF) of the two data sets (Espinar *et al.*, 2008).

$$KSI = \frac{100}{A_c} \int_{x_{min}}^{x_{max}} D_n dx \quad (A.8)$$

Where D_n is the absolute difference between the two normalized CDF distributions within irradiance interval of the measured and generated data sets. The critical area (A_c) is calculated as a function of the maximum (x_{max}) and minimum (x_{min}) DNI values, and the number of points used in the CDF distribution (N):

$$A_c = \frac{1.63}{\sqrt{N}} (x_{max} - x_{min}) \quad (A.9)$$

The KSI approaches zero as the two CDF distributions become identical. The two datasets can then be significantly similar in a statistical sense.

Indicators of dispersion were calculated for the GRT and UFS datasets (Table 2). The percentage values calculated for the MBD and NRMSD are low, which indicate low dispersion and a good performance of the method.

Table 41: Annual indicators of dispersion

| Parameter | GRT | UFS |
|-----------|-------|------|
| MBD [%] | 0.24 | 0.43 |
| NRMSD [%] | 10.55 | 9.74 |

Overall statistical performance indicators were calculated for the GRT and UFS datasets (Table 3). The NSE, WIA and LCE are all above 0.8, where a value of 1 indicates a perfect match between the data being compared. This is considered an acceptable indication that the method has performed well at both locations.

Table 42: Overall performance indicators

| Parameter | GRT | UFS |
|-----------|--------|--------|
| NSE | 0.8144 | 0.8478 |
| WIA | 0.8144 | 0.8481 |
| LCE | 0.8073 | 0.8432 |

The procedure for calculating the KSI for the UFS and GRT datasets is illustrated in Figure 4. The first column shows the observed and the predicted normalized frequency of the DNI datasets.

The second column shows the CDF for the observed and predicted datasets at both sites. The third column shows the absolute difference (D_n) between the predicted and the observed CDF curves.

The KSI index is calculated as 3.13 % for GRT and 2.34 % for UFS. The KSI indices suggest that the statistical distribution of the predicted and measured DNI data over the year is almost identical for both of the sites.

Considering the indicators of dispersion, the indicators of overall statistical performance and the KSI indices, the method generates DNI data for both of the sites with a significant correlation to the measured data.

A.4. Conclusion

A method developed by Fernandez-Peruchena *et al.* was implemented using DNI data acquired from the SAURAN network. Synthetic minute averaged DNI datasets were successfully generated using given hourly DNI datasets.

The statistical comparison of the generated and measured DNI datasets indicates no significant difference at either of the locations. This shows that the method for generating synthetic DNI has performed well. While the annual solar energy is correctly generated using the method, individual days of the generated DNI do not exactly match the measured DNI. This could result in minor errors while modelling the electrical yield of a CSP plant. Further investigation is required to determine the effect of these deviations on a daily basis.

Appendix B:

Plant control and operation strategy

The control system of for both plants is implemented using MATLAB® Stateflow. Stateflow is a logic tool that allows for the modelling of reactive systems. Predefined states represent real modes of operation of a CSP plant. The operating mode is changed once set-points have been reached or a certain period of time has passed. The state-based control method is described via the three logic diagrams for the main control areas: the parabolic trough solar field (Figure 52), the power tower receiver and heliostat field (Figure 53) and the power cycle (Figure 54).

B.1. Parabolic trough solar field control

The operation of the solar field is complicated by the transient nature of the HTF in the solar field. Due to the length of piping and receiver tubes in the field, there is a large volume of HTF in circulation. Furthermore, the available solar resource regularly fluctuates due to clouds passing over the solar field. The circulation of this salt must be carefully managed to ensure safe and efficient operation of the plant.

The solar field modes are determined by the time of day (*TOD*) and the return temperature of the solar field ($T_{SF,out}$). The *TOD* start and stop set points are associated with the sunrise and sunset of every day, which is determined using the zenith angle from the solar geometry model.

Design circulation → Mode (3)

During normal operation (design circulation) HTF is circulated from the cold tank, through the solar field and into the hot tank. The HTF enters each loop at the design point cold tank temperature of 290 °C. The return temperature of loop is held constant at 565 °C by changing the mass flow rate using simple proportional feedback control.

The mass flow rate is limited by the solar field HTF pump. During design circulation the pump is limited to 120 % of its design point mass flow. The lower mass flow limit is 2 kg/s per loop – this has been tested by Donnola *et al.* (2015) to ensure turbulent flow to allow for adequate heat transfer, which prevents deformation of receiver tubes.

When there is reduced solar radiation available the controller will respond by lowering the mass flow rate in response, to the limit of 2 kg/s. If this limit is met and the outlet temperature drops below the set point ($T_{hot} = 530\text{ °C}$) while the *TOD* still allows for operation, the insufficient radiation circulation mode is entered.

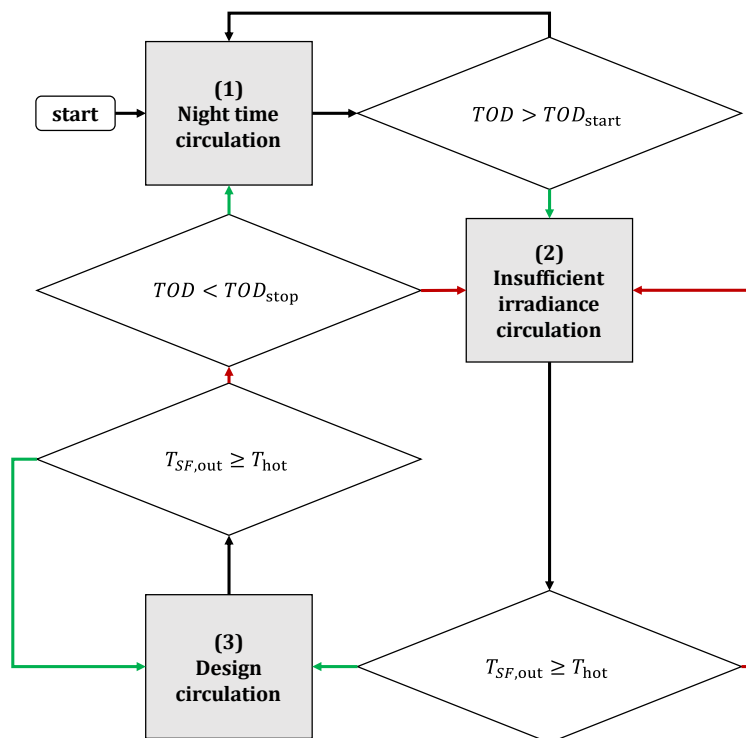


Figure 52: Control logic for parabolic trough solar field

Insufficient radiation circulation → Mode (2)

HTF is circulated from the cold tank, through the solar field and back to the cold tank in this mode of operation. The outlet temperature of the solar field is not sufficient to allow for circulation into the hot tank. The mass flow rate is set to the minimum day time set point of 2 kg/s.

If sufficient radiation allows for the set point temperature to be met again, the controller will return to design circulation mode. If the TOD reaches the point where the elevation angle is not sufficient for further solar field operation ($TOD > TOD_{stop}$) then night time circulation mode is entered.

Night time circulation → Mode (1)

For the parabolic trough HTF system the primary concern is the freezing of the molten salt in the solar field. In order to prevent this, a method proposed by Kearney *et al.* (2004) has been implemented into the operation strategy. During normal operation, the salt is circulated from the cold tank, through the solar field and into the hot tank. At the end of the day when there is no available radiation, the return temperature of the salt begins to drop. Once the return temperature is lower than a set point of 500 °C, the salt is redirected to return to the cold tank. This medium temperature salt in the solar field then increases the average temperature of the cold tank to approximately 310 – 320 °C.

Overnight the salt is circulated between the cold tank and the solar field. The mass flow rate is set to a minimum of 4 kg/s (similar to the ASE demonstration plant). This relatively high flow rate ensures that all of the HTF components are kept warm and prevents freezing in the flexible hoses and valves. The increase flow rate does,

however, result in increased heat loss overnight. The return temperature of the solar field overnight starts at approximately 300 °C and approaches a minimum of 285 °C just before sunrise. If the temperature falls below this point molten salt from the hot tank is used to maintain the field outlet temperature at 285 °C.

The TOD set point to start operation is determined by the solar zenith angle that allows for the operation of the solar collectors ($\theta_z > 5^\circ$). The controller will then enter insufficient radiation circulation mode until the set outlet temperature can be reached.

Figure 53 shows the operation of the parabolic trough solar field over two consecutive days in Springbok. The first day is heavily clouded and the second day is perfectly clear.

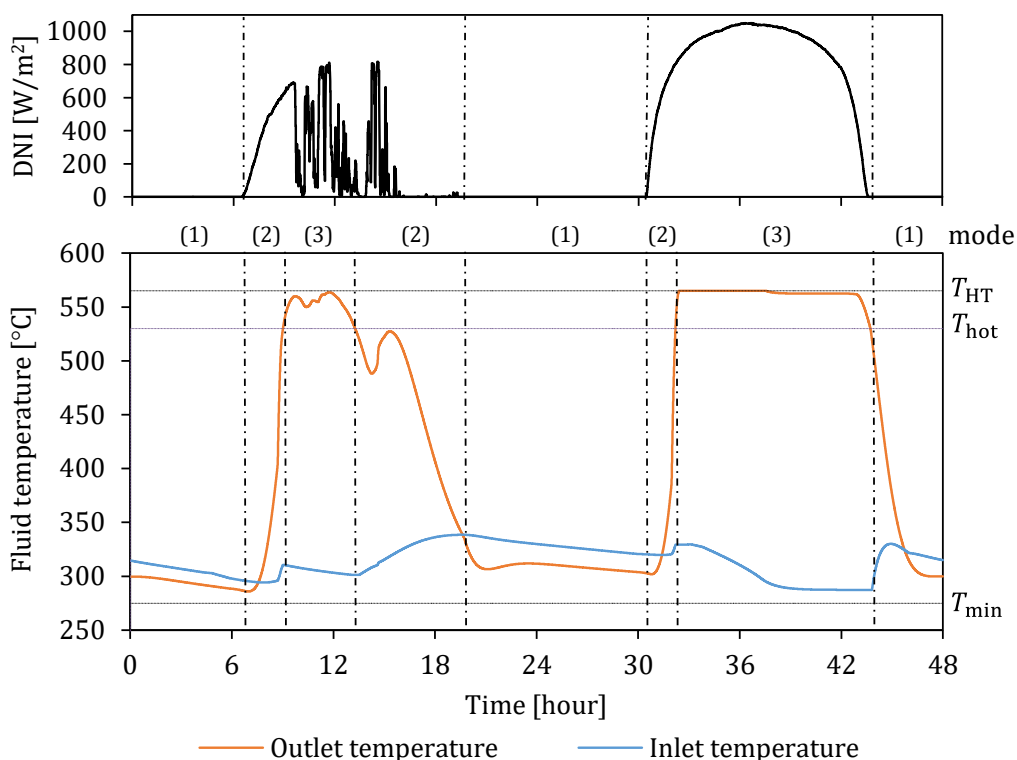


Figure 53: Temperature control of the parabolic trough solar field over two consecutive days in Springbok

The field control starts operation Mode (1) as the *TOD* is still before sunrise. The HTF is circulated at 4 kg/s from the cold tank, through the solar field and back to the cold tank. As the *TOD* reaches sunrise Mode (2) is entered and the mass flow rate reduces to 2 kg/s. When the outlet temperature of the loop reaches the required temperature (T_{hot}), Mode (3) is entered. In Mode (3) the pump control attempts to maintain the outlet temperature at 565 °C (T_{HT}), however, there is insufficient solar radiation to do so and the temperature drops below T_{hot} , reentering Mode (2).

In Mode (2) all of the medium temperature HTF in the field is recirculated to the cold tank, which causes the cold tank temperature to rise to 330 °C. The controller returns to Mode (1) at sunset to return to nighttime recirculation. Overnight the

return temperature of the loop is successfully held above the minimum (T_{\min}) without using any trace heating in the field.

The second day of operation is typical of a high DNI day. The control transitions from Mode (2) to Mode (3) at the start of operation. During design circulation the return temperature of $565\text{ }^{\circ}\text{C}$ is maintained. When the available radiation begins to reduce, the outlet temperature of the field falls below T_{hot} at the same time as sunset, therefore the control returns to Mode (1) for nighttime recirculation.

B.2. Power tower receiver and solar field control

The molten salt cycle control for a power tower plant is similar to the control of the solar field in the parabolic trough plant. The control operating modes are made somewhat more complicated due to the fact that the receiver is drained when it is not in operation. The operating modes are illustrated in Figure 54.

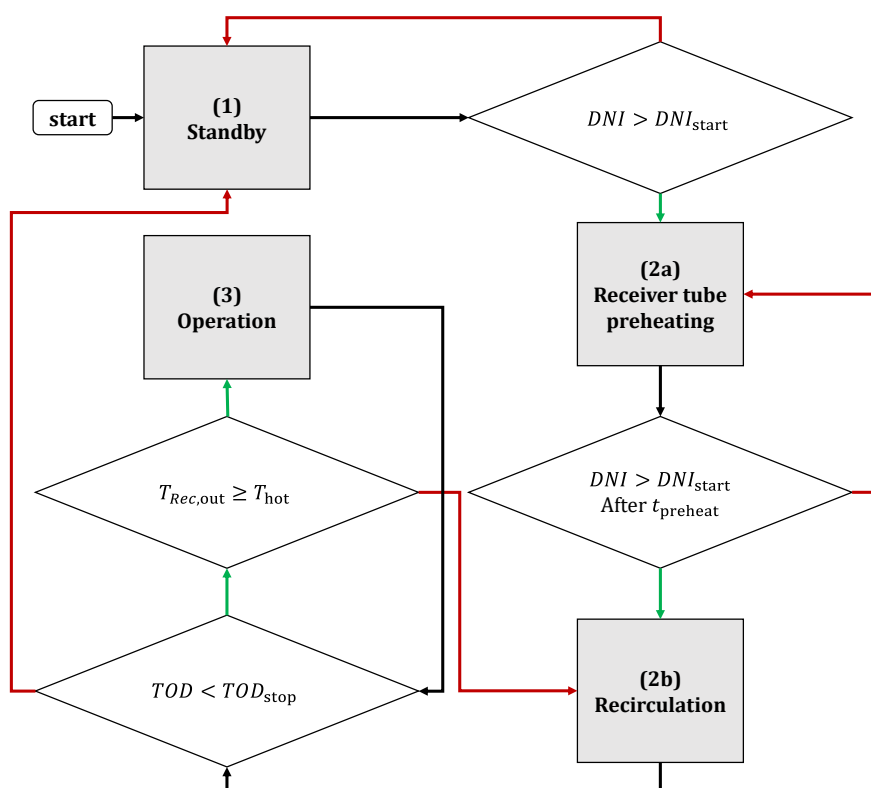


Figure 54: Power tower receiver control logic

Standby → Mode (1)

The receiver begins operation in standby (Mode 1). When there is sufficient DNI to begin operation, the control enters Mode (2a) ($DNI_{\text{start}} = 50\text{ W/m}^2$).

Receiver tube preheating → Mode (2a)

Mode (2a) allows for the preheating of the receiver tubes using solar radiation from the heliostat field. The time given for preheating (t_{preheat}) is 30 minutes, during which the receiver tubes will be heated up to $\sim 500\text{ }^{\circ}\text{C}$. The molten salt pumps are

then started up and Mode (2b) is entered. If the *TOD* falls later than sunset then the receiver returns to Mode (1) in standby.

Recirculation → Mode (2b)

Molten salt is circulated from the cold tank, up the riser, through the receiver tubes, through the downcomer and back to the cold tank. This recirculation continues at the minimum allowable flow rate of the pumps (10 % of design point flow rate). When the outlet temperature of the receiver reaches the set point (T_{hot}), Mode (3) is entered.

Receiver operation → Mode (3)

Mode (3) is the design point operation of the receiver. HTF is then diverted from the downcomer into the hot tank. The return temperature the receiver is held constant at 565 °C by changing the mass flow rate using simple proportional feedback control. The maximum mass flow rate achievable by the pump is 120 % of its design point flow rate. If the outlet temperature drops below the set point Mode (2b) is re-entered.

During Mode (3) an additional level of focus control is implemented (not shown in Figure 54). If the hot tank is completely full, the heliostat field is defocused to allow for sufficient energy to run the power cycle at full load without generating excess energy to be stored in the tank. This is implemented using simple proportional feedback control in both the parabolic trough and power tower models.

Figure 55 shows two days of operation of the power tower receiver model. Operation starts in Mode (1) and enters Mode (2a) when $DNI > DNI_{start}$. After 30 minutes, recirculation begins (Mode 2b) and the HTF temperature rises from the cold tank temperature to 565 °C. The receiver then enters Mode (3) assumes nominal operation. From hour 10 onwards, the receiver does not receive sufficient energy to maintain the outlet temperature of the receiver at 565 °C – therefore it changes between Mode (2b) and Mode (3) during the day.

The second day of operation shows a more typical day where the outlet temperature of the receiver is maintained after which it returns to standby overnight.

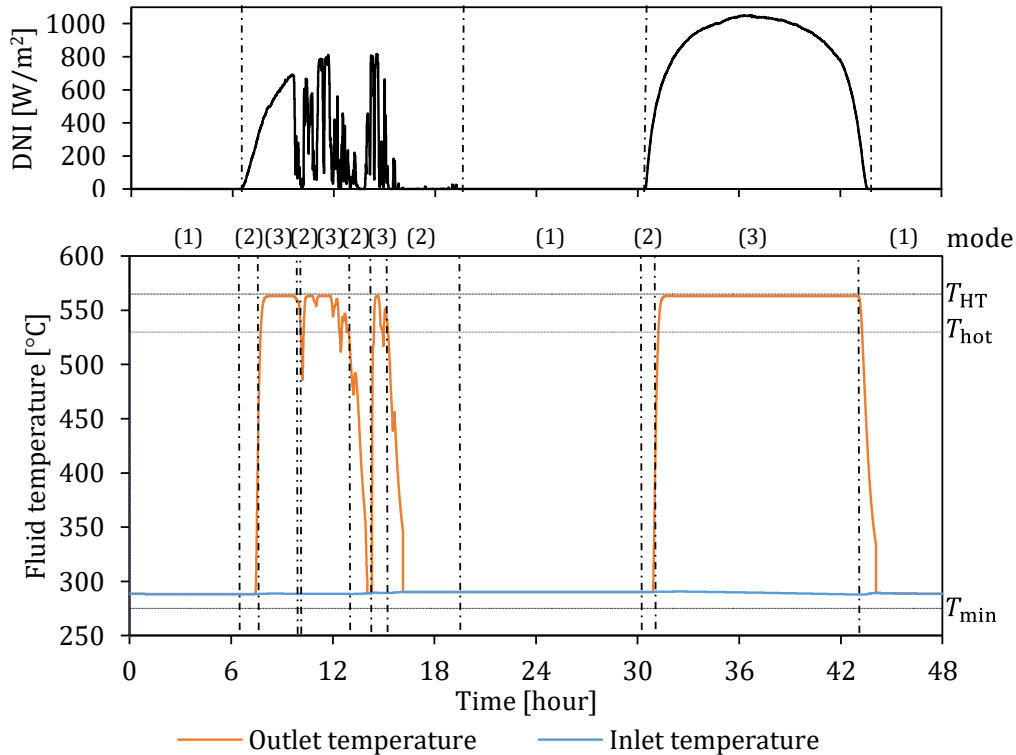


Figure 55: Temperature control of the power tower solar field over two consecutive days in Springbok

B.3. Power cycle control

Both the parabolic trough and power tower plants use the same power cycle and power cycle control. The power cycle control determines the operation of the steam cycle according to the available thermal energy in the hot tank and the tariff structure under which the plant is operating. The operation modes are as follows (Figure 56):

Power cycle stopped → *Mode (1)*: The steam cycle is shut down. The molten salt steam generator is drained and no HTF mass flow or steam cycle operation occurs. When the mass in the hot tank (m_{start}) is greater than the startup set point and the *TOD* is greater than the startup time, Mode (2a) is entered.

Turbine startup → *Mode (2)*: The turbine begins operation at 50 % of its design output in order to simulate a starting up process of the steam turbine system. The turbine operates at a lower efficiency, which results in a loss in thermal energy during the restart. HTF is pumped from the hot tank at 50 % of the design mass flow rate to the power cycle. After a 1 hour warm-up (t_{startup}), Mode (3) is entered. If the mass in the hot tank drops below the start-stop threshold ($m_{\text{stop}} = m_{\text{start}}$) during startup, the power cycle control returns to Mode (1).

Design point operation → *Mode (3)*: The power cycle operates at design point. HTF is pumped from the hot tank at the required flow rate to meet the design point thermal

demand of the power cycle. If the mass in the hot tank falls below the stopping threshold (m_{stop}) or the TOD reaches TOD_{stop} , Mode (4) is entered.

Cooldown → *Mode (4)*: During cooldown the steam generating system and turbine stop operation and begin cooling down for a set period ($t_{cooldown}$). If there is further solar radiation available and the mass in the hot tank increases again, the turbine is restarted and returns to Mode (3), alternatively the power cycle is stopped and Mode (1) is entered.

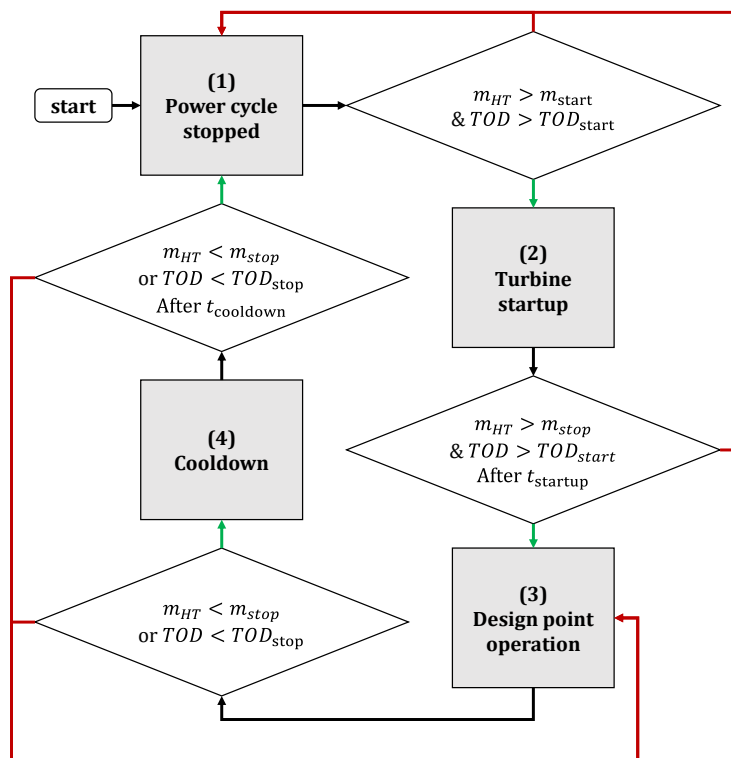


Figure 56: Power cycle control logic

When the power cycle operates under a flat tariff structure, the control system is set to generate as much electrical energy as possible. Therefore it does not consider the TOD limitations enforced in Figure 56, instead it is only dependent on the level of mass in the hot tank.

Figure 57 shows the power cycle in operation under a flat tariff in Springbok. Initially the power cycle is stopped in Mode (1). When there is sufficient DNI to allow for the hot tank to be filled above m_{start} , the turbine begins startup and Mode (2) is entered. After $t_{startup}$ the power cycle begins to produce electricity at design point and Mode (3) is entered.

During design point generation power cycle produces $\sim 100 \text{ MW}_e$ gross, however, the net output varies depending on the parasitic load on the system. Once the mass in the hot tank drops below m_{stop} Mode (4) is entered and the power cycle cools down and stops operation in Mode (1).

The same process is repeated in the second day of operation, however, there is not sufficient solar energy to allow for the period of generation demonstrated in the first day.

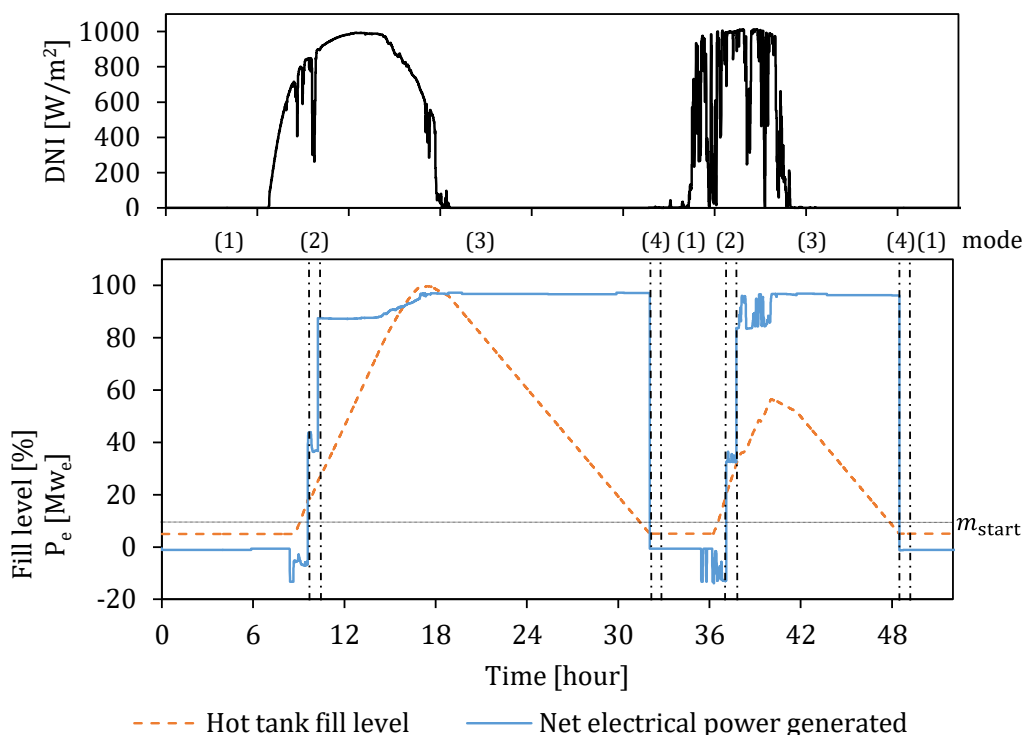


Figure 57: Power cycle operation with a flat tariff over two consecutive days in Springbok

Figure 58 shows the power cycle operating under a two-tiered tariff. Its operation is influenced by the mass in the hot tank and the TOD . The control system attempts to ensure that the power cycle generates power during times when there is payment for electricity that is generated and it shuts down operation during times of no payment

In Figure 58 the power cycle control is initially in Mode (1), however, unlike in Figure 57 the hot tank is already 60 % full. Mode (2), turbine startup, is initiated as soon as the TOD is greater than the set start time (TOD_{start}). Mode (3) is entered after $t_{startup}$ and design point generation is carried out during the normal tariff and peak tariff periods. When the zero tariff period starts, the TOD is greater than TOD_{stop} and the power cycle enters Mode (4) and then returns to Mode (1) overnight.

The fill level of the hot tank is kept at 55 % overnight, which allows for quick startup for the next day of operation. The second day of operation is similar to the first. This method of operation is simple and effective; however it does not implement intelligent operation to ensure that times of peak demand are met. Therefore over periods with multiple days of poor solar irradiation the hot tank level will remain low and the power cycle may not operate during peak tariff hours.

The implementation of a fixed start-up point can also result in multiple start-ups on days with poor radiation. Multiple start-ups results in energy being wasted, as the steam turbine and the steam cycle components warm up and begin operation in off-design conditions on more than one occasion during the day. A more intelligent operating strategy results in the plant performing as if it were operated by a well-trained operator – thereby reducing the number of start-ups and the dumping of energy. An improved operating strategy in simulation can increase the annual yield by ~2 % (Wagner & Wittmann, 2013).

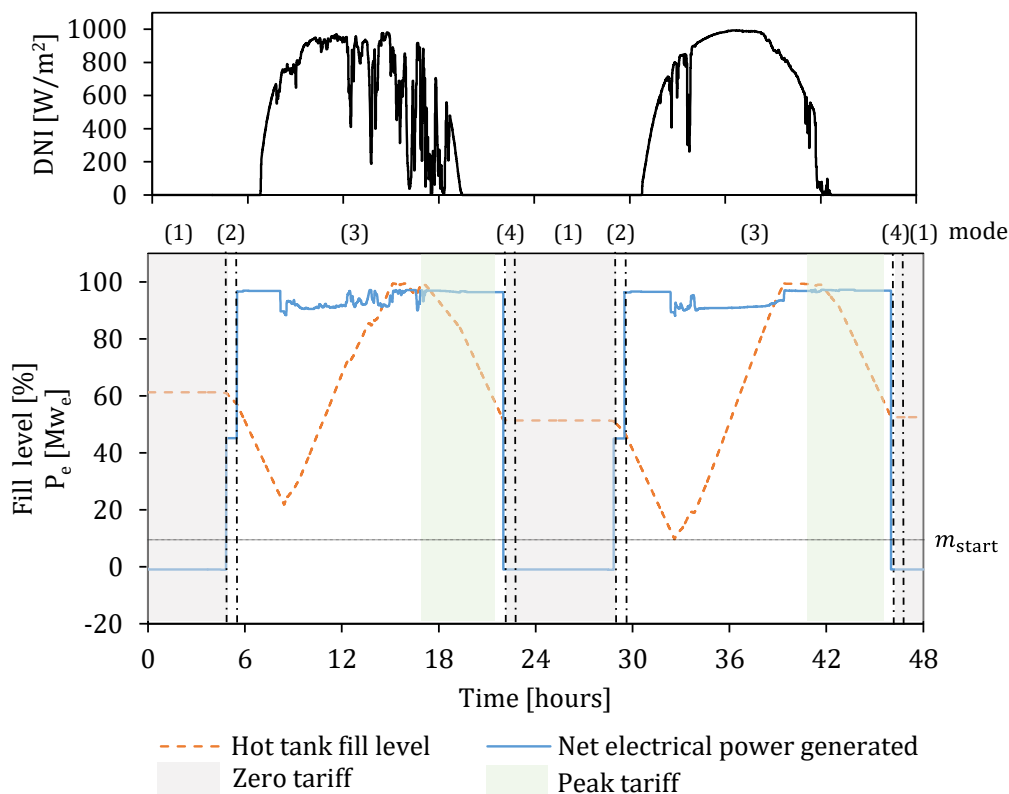


Figure 58: Power cycle control with a two-tiered tariff over two consecutive days in Upington

B.4. Conclusion

The control system and operation strategy has been described and illustrated using model operational data. The parabolic trough solar field control successfully implements freeze protection using thermal energy from the cold tank, which is a key factor to the feasibility of molten salt power tower plants.

The two operating strategies for the power cycle indicate the fundamental differences in plant operation, which are enforced by the tariff structure.

Appendix C: Pressure drop calculations

This section contains the pressure drop calculations for the parabolic trough solar field and the power tower receiver. The pumping of HTF is a substantial auxiliary consumption for both of the plants, which is proportional to the pressure that is required by the main HTF pumps.

The mass flow rate for the solar field / receiver HTF pumps is calculated using the design point thermal power required and the temperature difference expected across the solar field.

$$\dot{m}_{dp} = \frac{P_{th,SF}}{c_p(\bar{T}) (T_{CT} - T_{HT})} \quad (C.1)$$

C.1. Parabolic trough solar field

The generic solar field layout used for the molten salt parabolic trough plant model is illustrated in Figure 59. The design point flow rate through each loop ($\dot{m}_{dp,loop}$) is then calculated as the design point mass flow rate (\dot{m}_{dp}) divided by the number of loops (N_{loops}).

$$\dot{m}_{dp,loop} = \frac{\dot{m}_{dp}}{N_{loops}} \quad (C.2)$$

The procedure for calculating pressure drop in the piping is as follows:

$$Q_{pipe} = \frac{\dot{m}_{pipe}}{\rho_{HTF}} \quad (C.3)$$

$$A_{pipe} = \frac{\pi D_{pipe}^2}{4} \quad (C.4)$$

$$V_{pipe} = \frac{Q_{pipe}}{A_{pipe}} \quad (C.5)$$

$$Re_{pipe} = \frac{\rho_{HTF} V_{pipe}}{D_{pipe} \mu_{HTF}} \quad (C.6)$$

$$f_{pipe} = 0.184 Re_{pipe}^{-0.2} \quad (C.7)$$

$$\Delta P_{pipe} = \frac{f_{pipe} V_{pipe}^2 \rho_{HTF} L_{pipe}}{2 D_{pipe}} \quad (C.8)$$

The fluid properties for all pressure drop calculations are assumed to be at the average operating temperature for simplification.

A maximum flow rate of 2 m/s in the runner and header pipes is selected to reduce pressure drop in the field. This minimum flow velocity is then used to size the field piping. There are two runner pipes in the design field layout (one running North and one South). Therefore the mass flow in each runner pipe is:

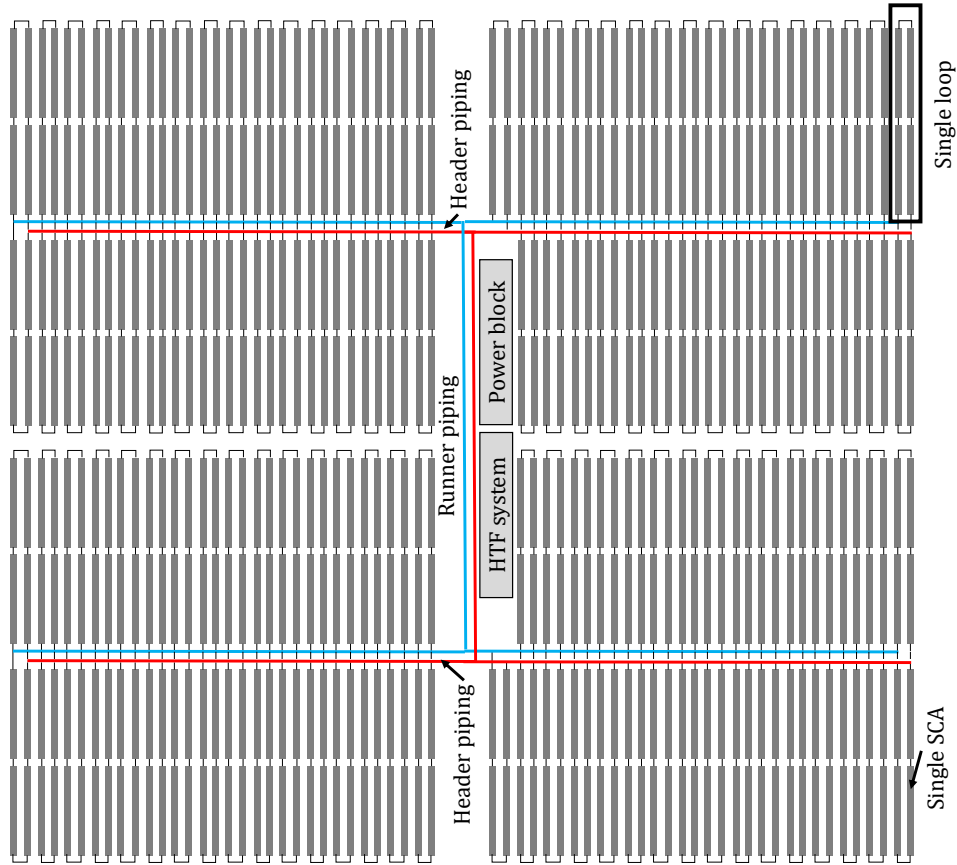


Figure 59: 'H-shaped' molten salt parabolic trough solar field layout. The solar field is made up of hot (red) and cold (blue) runner and header pipes which distribute molten salt to individual loops in the field.

$$\dot{m}_{dp,runner} = \frac{\dot{m}_{dp}}{2} \quad (C.9)$$

The required diameter of the runner piping is therefore:

$$D_{runner} = \sqrt{\frac{4 \dot{m}_{runner}}{\rho_{HTF} V_{maximum} \pi}} \quad (C.10)$$

There are four header pipes in the field layout (running East - West), each one distributing HTF to the loops in one quarter of the solar field. The header piping diameter is recalculated at each loop branch to ensure that the maximum fluid velocity condition is met.

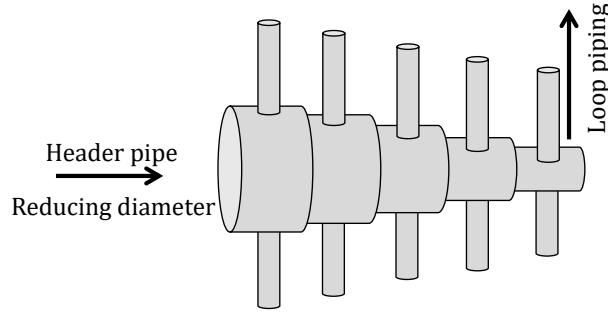


Figure 60: Illustration of header pipe in parabolic trough solar field with decreasing diameter

The mass flow in the first section of the header pipes is one fourth of the design point mass flow. The mass flow then steadily reduces at each section mass flow is diverted to individual loops. The number of reductions in each header can be the total number of loops in the field divided by 8 ($N_{\text{header,sec}} = N_{\text{loops}}/8$). The mass flow in each section ($\dot{m}_{\text{header,sec}}$) is:

$$\dot{m}_{\text{header,sec}}(i) = \frac{\dot{m}_{dp}}{4} - \left[\sum_{k=1}^{N_{\text{headersec}}} \frac{\dot{m}_{dp} k}{4 N_{\text{header,sec}}} \right] \quad (\text{C.11})$$

The diameter for each section (i) is then calculated as:

$$D_{\text{header}(i)} = \sqrt{\frac{4 \dot{m}_{\text{header,sec}}(i)}{\rho_{HTF} V_{\text{maximum}} \pi}} \quad (\text{C.12})$$

The mass flow through the receiver tubes in each loop is calculated as the total mass flow divided by the number of loops.

The pressure drop in the loop was accounted for by calculating the pressure drop in each of the four SCAs and the valves and flexible hoses associated with each loop. The pressure drop in the receiver tubes uses Equations C.2 to C.8 considering that there are four lengths of 247 m absorber tube in each loop with a diameter of 70 mm.

Each loop is assumed to contain 8 flexible hosing connections and 3 valves. The pressure drop across each of the piping components was calculated using Equation C.8 with a characteristic length of $L_{\text{valve}} = 10$ m and $L_{\text{flexible hose}} = 8.69$ m (Wagner & Gilman, 2011).

The total pressure drop across the field is calculated at each time step according to the mass flow rate into the field as follows:

$$\Delta P_{\text{field}} = \Delta P_{\text{loop}} + \Delta P_{\text{components}} + \Delta P_{\text{runner}} + \sum_{i=1}^n \Delta P_{\text{header}}(i) \quad (\text{C.13})$$

C.2. Power tower receiver

The pressure drop for the receiver has been modelled using a series of straight and bent tubes running through a single panel of the cylindrical receiver. The total pressure drop is the sum of the pressure drop in the panel and the pressure associated with pumping the fluid up to the receiver (Wagner, 2008).

The design point flow rate through each loop panel is calculated as the design point mass flow rate (\dot{m}_{dp}) divided by the number of flows (N_{flows}). The number of flows in the receiver design implemented is 2.

$$\dot{m}_{dp,panel} = \frac{\dot{m}_{dp}}{N_{flows}} \quad (C.14)$$

The procedure for calculating pressure drop in the receiver tube piping is as follows:

$$Q_{rec,tube} = \frac{\dot{m}_{rec,tube}}{\rho_{HTF}} \quad (C.15)$$

$$A_{rec,tube} = \frac{\pi D_{rec,tube}^2}{4} \quad (C.16)$$

$$V_{rec,tube} = \frac{Q_{rec,tube}}{A_{rec,tube}} \quad (C.17)$$

$$Re_{rec,tube} = \frac{\rho_{HTF} V_{rec,tube}}{D_{rec,tube} \mu_{HTF}} \quad (C.18)$$

$$f_{rec,tube} = 0.184 Re_{rec,tube}^{-0.2} \quad (C.19)$$

$$\Delta P_{rec,tube} = \frac{f_{rec,tube} V_{rec,tube}^2 \rho_{HTF} L_{rec,tube}}{2 D_{rec,tube}} \quad (C.20)$$

The fluid properties for all pressure drop calculations are assumed to be at the average operating temperature for simplification.

The two flows through the receiver each pass through 8 panels, which consist of 64 tubes in parallel. The receiver tubes have a 47 mm internal diameter and are assumed to be the length of the height of the receiver. The flow path for each panel includes pressure drops for two 45° (ΔP_{45°) and four 90° (ΔP_{90°) bends. The equivalent lengths for these bends are assumed to be 0.3 m and 2.3 m respectively. The pressure drop associated with pumping the HTF up the riser is simplified as a simple column of HTF (De Meyer *et al.*, 2015):

$$\Delta P_{tower} = H_{tower} \rho_{HTF} g \quad (C.21)$$

The total pressure drop for the receiver system is therefore:

$$\Delta P_{rec} = \Delta P_{rec,tubes} + \Delta P_{45^\circ} + \Delta P_{90^\circ} + \Delta P_{tower} \quad (C.22)$$

Appendix D: Levelized cost of electricity sensitivity

The cost of each major component of the plants was taken from literature. A sensitivity analysis has been carried out in order to investigate the sensitivity of the levelized cost of electricity to the different component cost assumptions. Both types of plants share the same thermal energy storage and power cycle components, for this reason they have not been included in the analysis.

The discount rate and EPC cost fraction for both technologies was set at 8 % and 30 % respectively. The solar field costs and receiver / HTF system costs differ between the technologies.

Table 43: Cost components used for sensitivity analysis of a power tower plant in Springbok

| Discount rate | LCOE $\left[\frac{\text{USD}}{\text{kWh}_e}\right]$ | EPC cost fraction | LCOE $\left[\frac{\text{USD}}{\text{kWh}_e}\right]$ | Solar field cost $[\text{USD}/\text{m}^2]$ | LCOE $\left[\frac{\text{USD}}{\text{kWh}_e}\right]$ | Receiver cost $[\text{USD}/\text{kW}_{\text{th}}]$ | LCOE $\left[\frac{\text{USD}}{\text{kWh}_e}\right]$ |
|---------------|---|-------------------|---|--|---|--|---|
| 5.6 % | 0.107 | 21.0 % | 0.121 | 119 | 0.115 | 119 | 0.122 |
| 6.4 % | 0.114 | 24.0 % | 0.124 | 136 | 0.120 | 136 | 0.125 |
| 7.2 % | 0.122 | 27.0 % | 0.127 | 153 | 0.125 | 153 | 0.127 |
| 8.0 % | 0.129 | 30.0 % | 0.129 | 170 | 0.129 | 170 | 0.129 |
| 8.8 % | 0.137 | 33.0 % | 0.132 | 187 | 0.134 | 187 | 0.132 |
| 9.6 % | 0.145 | 36.0 % | 0.135 | 204 | 0.139 | 204 | 0.134 |
| 10.4 % | 0.154 | 39.0 % | 0.137 | 221 | 0.143 | 221 | 0.136 |

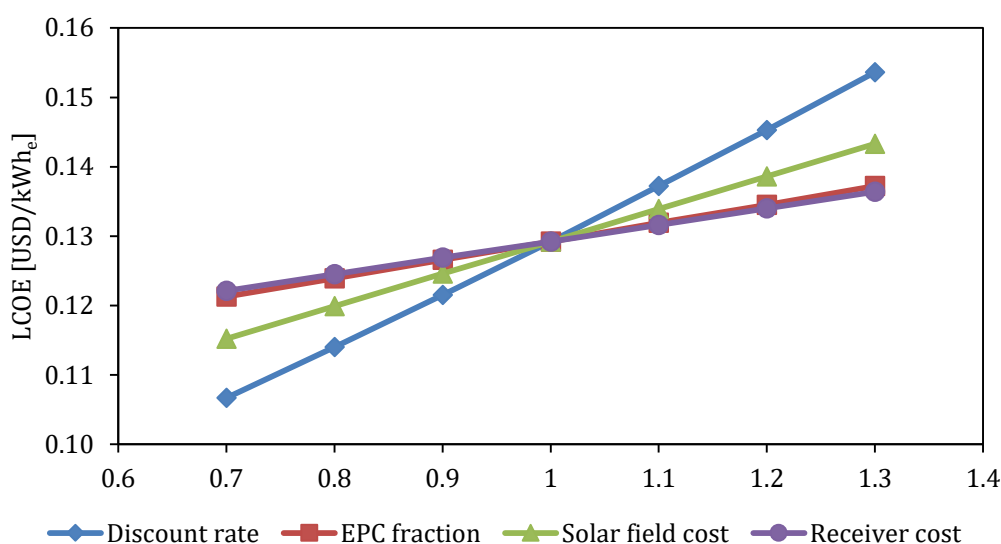


Figure 61: LCOE sensitivity analysis for a power tower plant

Table 44: Cost components used for sensitivity analysis of a parabolic trough plant in Springbok

| Discount rate | LCOE $\left[\frac{\text{USD}}{\text{kWh}_e}\right]$ | EPC cost fraction | LCOE $\left[\frac{\text{USD}}{\text{kWh}_e}\right]$ | Solar field cost $[\text{USD}/\text{m}^2]$ | LCOE $\left[\frac{\text{USD}}{\text{kWh}_e}\right]$ | HTF system cost $[\text{USD}/\text{m}^2]$ | LCOE $\left[\frac{\text{USD}}{\text{kWh}_e}\right]$ |
|---------------|---|-------------------|---|--|---|---|---|
| 5.6 % | 0.105 | 21.0 % | 0.119 | 125 | 0.114 | 49 | 0.122 |
| 6.4 % | 0.112 | 24.0 % | 0.122 | 142 | 0.118 | 56 | 0.123 |
| 7.2 % | 0.119 | 27.0 % | 0.124 | 160 | 0.122 | 63 | 0.125 |
| 8.0 % | 0.127 | 30.0 % | 0.127 | 178 | 0.127 | 70 | 0.127 |
| 8.8 % | 0.134 | 33.0 % | 0.129 | 196 | 0.131 | 77 | 0.128 |
| 9.6 % | 0.142 | 36.0 % | 0.132 | 214 | 0.135 | 84 | 0.130 |
| 10.4 % | 0.150 | 39.0 % | 0.134 | 231 | 0.140 | 91 | 0.132 |

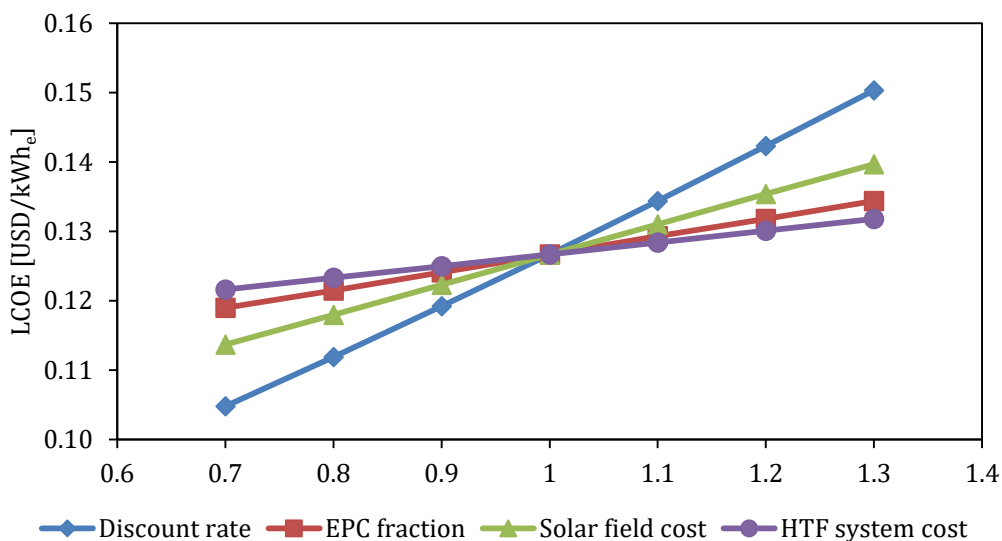


Figure 62: LCOE sensitivity analysis for a parabolic trough plant

The sensitivity analysis indicates that both the technologies are primarily sensitive to the discount rate. Both plants are sensitive to changes in solar field costs – with power towers being slightly more sensitive than parabolic troughs.

The cost of heliostat components such as the mirrors, drives and structures have a large effect on the solar field cost and therefore the LCOE of power tower plants. The cost of solar collector mirrors, structures and receiver tubes have a large effect on the parabolic trough plants.

Appendix E: Thermophysical properties of molten salt

Thermal conductivity [W/m K]:

$$\lambda = 0.443 + 0.00019 \left(\frac{T}{^{\circ}\text{C}} \right) \quad (\text{E.1})$$

Viscosity [m Pa s]:

$$\mu = 22.714 - 0.12 \left(\frac{T}{^{\circ}\text{C}} \right) + 0.0002281 \left(\frac{T}{^{\circ}\text{C}} \right)^2 - 0.0000001474 \left(\frac{T}{^{\circ}\text{C}} \right)^3 \quad (\text{E.2})$$

Heat capacity [kJ/kg K]:

$$c_p = 1.443 + 0.000172 \left(\frac{T}{^{\circ}\text{C}} \right) \quad (\text{E.3})$$

Density [kg/m³]:

$$\rho = 2090 - 0.636 \left(\frac{T}{^{\circ}\text{C}} \right) \quad (\text{E.4})$$

Enthalpy [kJ/kg]:

$$h = -15.068 + 1.15172 \left(\frac{T}{^{\circ}\text{C}} \right) \quad (\text{E.5})$$

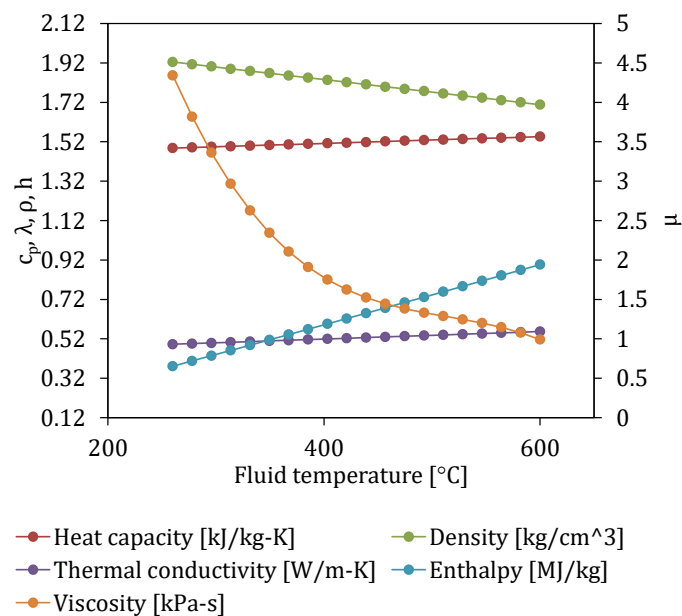


Figure 63: Properties of solar salt

Appendix F: Site monthly direct normal irradiance

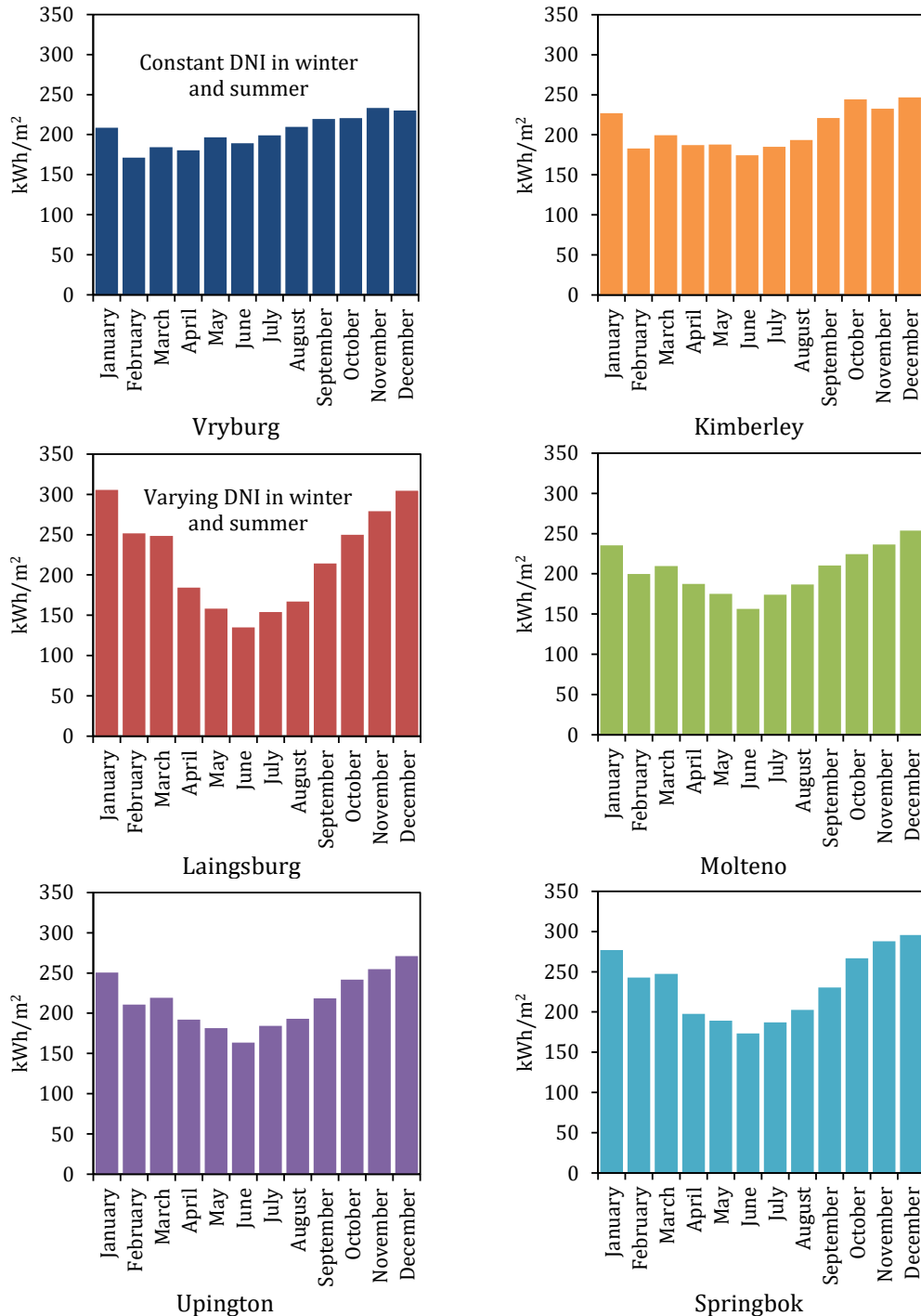


Figure 64: Monthly DNI distribution for selected sites in South Africa

References

- Abengoa Solar. 2015a. Abengoa Solar - PS10 and PS20.
http://www.abengoasolar.com/web/en/plantas_solares/plantas_para_terceros/espana/. Date accessed: 1 September 2016.
- Abengoa Solar. 2016. Abengoa Solar - Solar Plants in Chile.
http://www.abengoasolar.com/web/en/plantas_solares/plantas_propias/chile/. Date accessed: 1 September 2016.
- Abengoa Solar. 2015b. Abengoa Solar - Solar Plants in South Africa.
http://www.abengoasolar.com/web/en/plantas_solares/plantas_propias/sudafrica/. Date accessed: 1 September 2016.
- Abengoa Solar. 2013a. Development of Molten-Salt Heat Transfer Fluid Technology for Parabolic Trough Solar Power Plants. Conference paper: Sunshot Conference.
- Abengoa Solar. 2013b. Development of Molten-Salt Heat Transfer Fluid Technology for Parabolic Trough Solar Power Plants. Abengoa Solar Technical report: DE FC36 08G018038
- Abengoa Solar. 2013c. Solana - Fact Sheet.
http://www.abengoasolar.com/export/sites/abengoasolar/resources/pdf/Solana_factsheet_09092013.pdf. Date accessed: 3 September 2016.
- Archimede Solar Energy. 2016. Concentrated Solar Power (CSP) The new frontier of molten salts. Archimede Solar Energy company profile.
- Augsburger, G. 2013. Thermo-economic optimisation of large solar tower power plants. Master's thesis: École Polytechnique Federale de Lausanne.
- Bauer, T., Breidenbach, N. & Eck, M. 2013. Overview of Molten Salt Storage Systems and Material Development for Solar Thermal Power Plants. Conference Paper: SolarPACES.
- Becker, M. 1980. Comparison of heat transfer fluids for use in solar thermal power stations. *Electric Power Systems Research*, 3: 139–150.
- Beyer, H.G., Fauter, M., Schumann, K., Schenk, H. & Meyer, R. 2010. Synthesis of DNI time series with sub-hourly time resolution. Conference paper: SolarPACES.
- Brooks, M.J., du Clou, S., van Niekerk, J.L., Gauché, P., Leonard, C., Mouzouris, M.J., Meyer, A.J., van der Westhuizen, N., van Dyk, E. & Vorster, F.J. 2015. SAURAN: A new resource for solar radiometric data in Southern Africa. *Journal of Energy in Southern Africa*, 26.
- Burgaleta, J.I., Arias, S. & Ramirez, D. 2013. Gemasolar: The First Tower Thermosolar Commercial Plant with Molten Salt Storage System. Conference paper: SolarPACES.
- Burkholder, F. & Kutscher, C.F. 2009. Heat loss testing of Schott's 2008 PTR70 parabolic trough receiver. NREL Technical Report: NREL/TP-550-45633
- Cabeza, L.F., Solé, C., Castell, A., Oró, E. & Gil, A. 2012. Review of solar thermal storage

- techniques and associated heat transfer technologies. Conference paper: Proceedings of the IEEE. 525–538.
- Collado, F.J. 2008. Quick evaluation of the annual heliostat field efficiency. *Solar Energy*.
- Department of Energy. 2013. Presentation: Bid Window 3 Preferred Bidders.
- Department of Energy, Department of National Treasury & Development Bank of Southern Africa. 2015. Independent Power Producer Procurement Programme: An overview. <http://www.ipprenewables.co.za/>. Date accessed: 19 June 2016.
- Dersch, J., Schwarzbözl, P. & Richert, T. 2010. Implementation of Solar Towers in Greenius - A Tool for Fast Assessment of Technical and Economical Performance of CSP Systems. Conference paper: SolarPACES.
- Dinter, F. & Busse, K.T. 2015. Overview of predictive CSP spread scenarios and its opportunities. *Journal of Energy in Southern Africa*.
- Dinter, F. & Gonzalez, D.M. 2013. Operability, Reliability and Economic Benefits of CSP with Thermal Energy Storage : First year of Operation of ANDASOL 3. Conference paper: SolarPACES.
- Dinter, F. & Möller, L. 2015. A Review of Andasol 3 and Perspective for Parabolic Trough CSP Plants in South Africa. Conference paper: SolarPACES.
- Department of Energy. 2015. State of Renewable Energy in South Africa. ISBN: 978-1-920435-08-0
- Donnola, S., Maccari, A., Matino, F. & Tamano, S. 2015. Archimede Solar Energy Molten Salt Parabolic Trough Demo plant : improvements and second year of operation. Conference paper: SolarPACES.
- Dow Chemical Company. 2001. DOWTHERM A - Synthetic Organic Heat Transfer Fluid — Liquid and Vapor Phase Data. <http://www.dow.com/heattrans/products/synthetic/dowtherm.htm> \n <http://www.dow.com/webapps/lit/litorder.asp?filepath=heattrans/pdfs/noreg/176-01463.pdf&pdf=true>. Date accessed: 25 August 2016.
- Duffie, J. a & Beckman, W. a. 2013. *Solar engineering of thermal processes*.
- Ehrhart, B. & Gill, D. 2013. Evaluation of Annual Efficiencies of High Temperature Central Receiver Concentrated Solar Power Plants with Thermal Energy Storage. Conference paper: SolarPACES.
- Eskom. 2015. Generation Connection Capacity Assessment of the 2022 Transmission Network. Eskom report: GCCA-2022.
- Espinar, B., Ramirez, L., Drews, A., Beyer, H.G., Zarzalejo, L.F., Polo, J. & Martin, L. 2008. Analysis of different comparison parameters applied to solar radiation data from satellite and German radiometric stations. *Solar Energy*, 83: 118–125.
- Falchetta, M., Liberati, G., Consoli, D., Malloggi, S., Mazzei, D. & Crescenzi, T. 2010. Commissioning of the Archimede 5 MW Molten Salt Parabolic Trough Solar Plant. Conference paper: SolarPACES.
- Fernández-Peruchena, C.M., Blanco, M., Gastón, M. & Bernardos, A. 2015. Increasing the temporal resolution of direct normal solar irradiance series in different

- climatic zones. *Solar Energy*, 115.
- Fichtner. 2010. Assessment of Technology Options for Development of Concentrating Solar Power in South Africa. World Bank and ESMAP presentation.
- Flueckiger, S., Yang, Z. & Garimella, S. V. 2011. Thermocline Energy Storage in the Solar One Power Plant: An Experimentally Validated Thermomechanical Investigation. Conference paper: International Conference on Energy Sustainability.
- García, E. & Calvo, R. 2012. One Year Operation Experience of Gemasolar Plant. Conference paper: SolarPACES.
- Gauché, P., Pfenninger, S., Meyer, A.J., von Backström, T.W. & Brent, A.C. 2012. Modeling Dispatchability Potential of CSP in South Africa. Conference paper: Southern African Solar Energy Conference (SASEC).
- GeoModel Solar. 2014. Accuracy enhanced solar maps of South Africa with technical report prepared for the Centre of Renewable and Sustainable Energy Studies, Stellenbosch University.
- Google Inc. 2015. Software package: Google Earth v7.1.5.1557.
- Grantham, A.P., Pudney, P.J., Boland, J.W. & Belusko, M. 2013. Synthetically Interpolated Five-minute Direct Normal Irradiance. Conference paper: 20th International Congress on Modelling and Simulation.
- Gueymard, C. a. 2014. A review of validation methodologies and statistical performance indicators for modeled solar radiation data: Towards a better bankability of solar projects. *Renewable and Sustainable Energy Reviews*, 39: 1024–1034.
- Heller, L. 2013. Literature Review on Heat Transfer Fluids and Thermal Energy Storage Systems in CSP Plants. Stellenbosch University technical report.
- Hirsch, T., Bachelier, C., Eck, M., Dersch, J., Giuliano, S., Goebel, O., Haller, U., Lude, S., Rau, C., Schenk, H., Schmidt, N., Seitz, M., Westphal, B. & Yildiz, E. 2015. Steps Towards a CSP Yield Calculation Guideline : A First Draft for Discussion in the SolarPACES Working Group guiSmo. Conference paper: SolarPACES.
- Hottel, H.C. 1975. A simple model for estimating the transmittance of direct solar radiation through clear atmospheres. Conference paper: International Solar Energy Congress and Exposition.
- Janotte, N., Feckler, G., Kötter, J., Decker, S., Herrmann, U., Schmitz, M. & Lüpfer, E. 2013. Dynamic performance evaluation of the HelioTrough ® collector demonstration loop – towards a new benchmark in parabolic trough qualification. Conference paper: SolarPACES.
- Kearney, D., Herrmann, U., Nava, P., Kelly, B., Mahoney, R., Pacheco, J., Cable, R., Potrovitza, N., Blake, D. & Price, H. 2003. Assessment of a molten salt heat transfer fluid in a parabolic trough solar field. *Journal of Solar Energy Engineering*, 125.
- Kearney, D., Kelly, B., Herrmann, U., Cable, R., Pacheco, J., Mahoney, R., Price, H., Blake, D., Nava, P. & Potrovitza, N. 2004. Engineering aspects of a molten salt heat transfer fluid in a trough solar field. *Energy*, 29(5-6): 861–870.

- Kelly, B. 2010. Advanced Thermal Storage for Central Receivers with Supercritical Coolants. Abengoa Solar Report: DE FG36 9G018149.
- Kolb, G., Ho, C., Mancini, T. & Gary, J. 2011. Power tower technology roadmap and cost reduction plan. Sandia National Laboratories report: SAND2011-2419.
- Kost, C., Thomsen, J., Schlegl, T., Fluri, T., Philipps, S., Lude, S., Hädrich, I., Weber, D. & Wirth, H. 2012. Support for Moroccan Solar Plan Solar Technologies in Morocco – Industry and Value Chain Assessment. Fraunhofer ISE project: 3505.9-011.00.
- Kurup, P., Turchi, C.S., Kurup, P. & Turchi, C.S. 2015. Parabolic Trough Collector Cost Update for the System Advisor Model (SAM).
- Lippke, F. 1995. Simulation of the Part-Load Behavior of a 30 MWe SEGS Plant. Sandia National Laboratories technical report. 1995-0012.
- Litwin, R.Z. & Park, C. 2002. Receiver System : Lessons Learned from Solar Two. Sandia National Laboratories technical report: 2002-0084.
- Llorente García, I., Álvarez, J.L. & Blanco, D. 2011. Performance model for parabolic trough solar thermal power plants with thermal storage: Comparison to operating plant data. *Solar Energy*, 85: 2443–2460.
- Maccari, A., Bissi, D., Casubolo, G., Guerrini, F., Lucatello, L., Luna, G., Rivaben, A., Savoldi, E., Tamano, S. & Zuanella, M. 2015. Archimede Solar Energy Molten Salt Parabolic Trough Demo Plant: A Step Ahead towards the New Frontiers of CSP. In SolarPACES.
- Matino, F. & Maccari, A. 2015. ScienceDirect Molten Salt receivers operated on Parabolic Trough Demo Plant and in laboratory conditions. Conference paper: SolarPACES.
- De Meyer, O.A.J., Dinter, F. & Govender, S. 2015. Thermal Resistance Model For CSP Central Receivers. Conference paper: SolarPACES.
- Meyer, R., Beyer, H.G., Fanslau, J., Geuder, N., Hammer, A., Hirsch, T., Hoyer-klick, C., Schmidt, N. & Schwandt, M. 2009. Towards Standardization Of CSP Yield Assessments. Conference paper: SolarPACES.
- Moore, R., Vernon, M., Ho, C.K., Siegel, N.P., Kolb, G.J. Design considerations for concentrating solar power tower systems employing molten salt. Sandia National Laboratories report: SAND2010-6978.
- National Renewable Energy Laboratory. 2016a. Concentrating Solar Power Projects. U.S. Department of Energy database.
- National Renewable Energy Laboratory. 2016b. NREL - Concentrating Solar Power Projects - Power Tower Projects. U.S. Department of Energy database.
- Nextera Energy Resources. 2014. Genesis Solar Energy Center - Fact Sheet. Nextera brochure.
- Nouredine, Y. & Kamal, M. 2012. Study of Performance of a Solar Power Tower (15 MW) Simulation and Results. Conference paper: SolarPACES.
- NREL. 2014. Ivanpah Solar Electric Generating System. U.S. Department of Energy database.
- NREL. 2015. Software package: System Advisor Model (SAM).

- NREL. 2012a. System Advisor Model (SAM) Case Study : Andasol-1. U.S. Department of Energy database.
- NREL. 2012b. System Advisor Model (SAM) Case Study : Gemasolar. U.S. Department of Energy database.
- Osuna, R., Morillo, R., Cantero, F., Robles, P., Romero, M., Valverde, A., Monterreal, R., Pitz-paal, R., Brakmann, G., Ruiz, V., Silva, M. & Menna, P. 2006. PS10 , Construction of a 11Mw Solar Thermal Tower Plant in Seville , Spain. Conference paper: SolarPACES.
- Pavlović, T.M., Radonjić, I.S., Milosavljević, D.D. & Pantić, L.S. 2012. A review of concentrating solar power plants in the world and their potential use in Serbia. *Renewable and Sustainable Energy Reviews*, 16: 3891–3902.
- Relancio, A.J., Cuellar, A., Walker, G. & Ettmayr, C. 2015. South African CSP Projects under the REIPPPP – requirements , challenges and opportunities. Conference paper: SolarPACES.
- Richert, T. & Nava, P. 2012. Performance of the Ultimate Trough ® Collector with Molten Salts as Heat Transfer Fluid. Conference paper: SolarPACES.
- Riffelmann, K., Richert, T., Nava, P. & Schweitzer, A. 2013. Ultimate Trough - A significant step towards cost-competitive CSP. Conference paper: SolarPACES.
- Riffelmann, K.-J., Graf, D. & Nava, P. 2011. Suitable solar field layouts for the Ultimate Trough® collector. Conference paper: SolarPACES.
- Rinaldi, F., Binotti, M., Gistri, A. & Manzolini, G. 2013. Comparison of Linear and Point Focus Collectors in Solar Power Plants. Conference paper: SolarPACES.
- Rodríguez-garcía, M., Herrador-moreno, M. & Zarza, E. 2014. Lessons learnt during the design , construction and start-up phase of a molten salt testing facility. *Applied Thermal Engineering*, 62(2): 520–528.
- Ruegamer, T., Kamp, H., Kuckelkorn, T., Schiel, W., Weinrebe, G., Nava, P., Richert, T. & Riffelmann, K. 2013. Molten Salt for Parabolic Trough Applications : System Simulation and Comparison with a Power Tower. Conference paper: SolarPACES.
- Rycroft, M. 2015. Renewable energy development zones (REDZ). Department of Energy report.
- Schwarzbözl, P. & Zentrum, D. 2006. A TRNSYS Model Library for Solar Thermal Electric Components (STEC). Software package: TRNSYS, STEC.
- Schweitzer, A., Schiel, W., Abul-Ella, Z., Nava, P., Riffelmann, K., Wohlfahrt, A. & Kuhlmann, G. 2011. Ultimate Trough® – The next generation collector for Parabolic Trough power plants. Conference paper: SolarPACES.
- Schweitzer, A., Schiel, W., Birkle, M., Nava, P., Riffelmann, K. & Wohlfahrt, A. 2013. ULTIMATE TROUGH ® - Fabrication, erection and commissioning of the world ' s largest parabolic trough collector. Conference paper: SolarPACES.
- Silinga, C., Gauché, P., Rudman, J. & Cebecauer, T. 2015. The South African REIPPPP two-tier CSP tariff : Implications for a proposed hybrid CSP peaking system. Conference paper: SolarPACES.
- Solar Reserve. 2016. Crescent Dunes CSP project. Project information brochure.

- SolarReserve LLC. 2016. Redstone Fact Sheet. Project information brochure.
- Solutia Incorporated. 2013. Therminol VP-1 Vapor Phase/Liquid Phase Heat Transfer Fluid. Therminol VP-1 data sheet.
- South African Weather Service. 2015. South African Weather Service - Climate Data Requests. <http://www.weathersa.co.za/compliments-complaints/climate-data-requests>. Date accessed: 10 June 2016.
- steag. 2016. EBSILON®Professional. Software package.
- Stine, W. & Geyer, M. 2001. Power from the Sun.
- Stoffel, T., Renné, D., Myers, D. & Wilcox, S. 2010. Concentrating Solar Power: Best Practices Handbook for the Collection and Use of Solar Resource Data.
- Stuetzle, T.A. 2002. Automatic Control of the 30 MWe SEGS VI Parabolic Trough Plant. Sandia National Laboratories report: SAND2002-0102.
- The MathWorks Inc. 2015a. MATLAB R2015a. Software package.
- The MathWorks Inc. 2015b. Simulink 8.5. Software package.
- Thermoflow Inc. 2016. Thermoflow. Software package.
- Touma, J.S. 2016. Dependence of the Wind Profile Power Law on Stability for Various Locations Dependence of the Wind Profile Power Law on Stability for Various Locations.
- Turchi, C. 2010. Parabolic Trough Reference Plant for Cost Modeling with the Solar Advisor Model (SAM). NREL technical report: NREL/TP-550-47605.
- Turchi, C.S., Heath, G.A., Turchi, C.S. & Heath, G.A. 2013. Molten Salt Power Tower Cost Model for the System Advisor Model (SAM). NREL technical report: NREL/TP-5500-57625.
- Vazquez, J., Relloso, S. & Domingo, M. 2006. Sener heliostat design and testing. Conference paper: SolarPACES.
- Wagner, M.J. 2008. Simulation and Predictive Performance Modeling of Utility-Scale Central Receiver System Power Plants. Master's thesis: University of Wisconsin – Madison.
- Wagner, M.J. & Gilman, P. 2011. Technical manual for the SAM physical trough model. NREL technical report: NREL/TP-5500-51825.
- Wagner, P.H. & Wittmann, M. 2013. Influence of different operation strategies on transient solar thermal power plant simulation models with molten salt as heat transfer fluid Patrick. Conference paper: SolarPACES.
- Wu, G.C., Deshmukh, R., Ndhlukula, K., Radojicic, T. & Reilly, J. 2015a. MapRE - Multi-criteria Analysis for Planning Renewable Energy - South Africa of Southern and Eastern Africa Renewable Energy Zones. International Renewable Energy Agency and Lawrence Berkeley National Laboratory, LBNL .
- Wu, G.C., Deshmukh, R., Ndhlukula, K., Radojicic, T. & Reilly, J. 2015b. Renewable Energy Zones for the Africa Clean Energy Corridor. International Renewable Energy Agency and Lawrence Berkeley National Laboratory, LBNL.
- Zavoico, A.B. 2001. Solar Power Tower Design Basis Document. A Sandia National Laboratories Report: SAND2001-2100.